Identification and Tracking of low Energy Spectator Protons

Inaugural-Dissertation
zur
Erlangung des Doktorgrades
der Mathematisch-Naturwissenschaftlichen Fakultät
der Universität zu Köln

vorgelegt von
Andreas Mussgiller
aus München

Köln, 2007

Abstract

The present theses discusses the development, technical design and realization as well as the read-out electronics of a detection system for the identification and tracking of low energy spectator protons.

With the knowledge of the four-momentum of such spectator protons it will be possible to use deuterium as an effective neutron target. Previous measurements with an early version of the detection system have already shown that this method works quite well to investigate for instance the ω or η-meson production in proton-neutron collisions. Moreover, after the completion and installation of the polarized internal target (PIT) at ANKE, it will be even possible to engage in that field with double polarized experiments. To increase the luminosity the polarized target is equipped with an extended target cell. The described detection-system will provide the vertex reconstruction for this extended interaction region. In addition, it will act as an independent beam polarimeter at ANKE.

The detection system consists of three layers of double-sided silicon strip detectors which are arranged in a telescope structure and placed inside the accelerator vacuum as close as 2 cm to the interaction region. The modular design of the electronics and the support structures for the detectors allows one to exchange detectors and electronics in a maximum flexible way. In a minimum configuration the telescope is equipped with two detectors, a thin ($\approx 69\,\mu$m) double-sided Silicon strip detector as a first layer and a very thick (≥ 5 mm) double-sided micro-structured Lithium-drifted Silicon detector as a second layer. With this arrangement it is possible to track and identify protons in a kinetic energy range from 2.5 MeV to 25 MeV. For deuterons this range for such a telescope configuration is from 4 MeV to 34 MeV.

The performance concerning the energy determination and tracking is shown based on data taken during a beam-time in November of 2003. With the existing setup an energy resolution of 120 keV for the 69 μm thick first detection layer could be achieved. The proton-deuteron separation was in the order of 3.8 σ. First results of the measurements of the analyzing powers A_y and A_{yy} for the reaction $\vec{d}p \rightarrow dp$ as well as A_y for the reactions $\vec{d}p \rightarrow (pp)n_{Spectator}$ and $\vec{d}p \rightarrow (np)p_{Spectator}$ are presented to demonstrate the possible applications of the detection-system.

Zusammenfassung

Im Rahmen der vorliegenden Arbeit wurde ein Detektionssystem zur Identifika-
tion und Spurrekonstruktion von niederenergetischen "Spektator"-Protonen ent-
wickelt. Die technische Realisierung des Detektorsystems und der speziell dafür
entwickelten Ausleseelektronik wird im Folgenden dargestellt.

Unter Zuhilfenahme des Viererimpulses eines solchen Spektator-Protons ist
es möglich, Deuterium als effektives Neutronentarget zu nutzen. Dies konnte
bereits durch Messungen mit einer ersten Version des Detektors zur ω und η
Meson Produktion in Proton-Neutron Stößen gezeigt werden. Die Fertigstel-
lung und Installation des Polarisierten Internen Targets (PIT) an ANKE wird
es des weiteren ermöglichen, Messungen am Neutron mit polarisiertem Strahl
und Target durchzuführen. Zur Erhöhung der Luminosität ist das polarisierte
Target mit einer ausgedehnten Speicherzelle ausgestattet, was zudem bedeutet,
dass die Reaktionsvertizes entlang der Zelle verteilt sind und nur durch den hier
beschriebenen Detektor eindeutig rekonstruiert werden können. Außerdem kann
das Detektionssystem als unabhängiges Strahlpolarimeter genutzt werden.

Das Detektorsystem besteht aus drei doppelseitigen Silizium-Streifen-
Detektoren, die in einer Teleskopstruktur angeordnet sind und bis auf 2 cm Ab-
stand zur Targetregion im Beschleunigervakuum plaziert werden. Durch den
modularen Aufbau der Elektronik und des Teleskops ist es möglich, Detektoren
und Ausleseelektronik abhängig von den Anforderungen auszutauschen. In einer
minimalen Konfiguration wird das Teleskop mit zwei Silizium-Detektoren ausge-
stattet sein. Als erste Lage dient ein dünner (69 μm) doppelseitiger Silizium-
Streifen-Detektor gefolgt von einem dicken ($\geq$ 5 mm) Lithium gedrifteten
Silizium-Detektor. Diese Anordnung erlaubt die Identifikation und Spur-
rekonstruktion von Protonen in einem Energiebereich von 2.5 MeV bis 25 MeV.
Für Deuteronen wird ein Energiebereich von 4 MeV bis 34 MeV abgedeckt.

Die Leistungsfähigkeit in Bezug auf die Energiemessung und Spurrekonstruk-
tion wird anhand von Daten, die während einer Strahlzeit im November 2003
aufgezeichnet wurden, dargestellt. Für die 69 μm dünne erste Detektorlage
konnte mit dem existierenden Teleskop eine Energieauflösung von 120 keV er-
reicht werden. Die Qualität der Proton-Deuteron Trennung lag hierbei bei 3.8 σ.
Die ersten Ergebnisse für die Messung der Analysierstärken A_y und A_{yy} für
die Reaktion $\vec{d}p \to dp$ sowie A_y für die Reaktionen $\vec{d}p \to (pp)n_{Spektator}$ und
$\vec{d}p \to (np)p_{Spektator}$ werden im Folgenden präsentiert.

Contents

vi

Chapter 1

Introduction

A major part of the intended future physics program for the ANKE spectrometer [1] at the cooler synchrotron COSY [2, 3, 4] of the Research Centre Jülich will concentrate on experiments with polarized beams and targets with special interest on proton-neutron spin physics [5]. Here, the detection setup described in this work serves as a spectator detector which allows the use of polarized and unpolarized deuterons as an effective neutron target. The polarized internal target PIT [6] of ANKE with an extended storage cell in combination with the polarized COSY beam will allow one to perform single and double polarized measurements in proton and deuteron induced reactions. Exploiting such an extended cell, requires however tracking detectors placed close to the target that provide the reaction vertex on an event-by-event basis. In addition to that, the polarization of deuteron beams at COSY is currently determined by polarization export of the measurements at low beam momenta. It would be desirable to also have an independent beam polarimeter at the ANKE spectrometer and this will also be provided by the tracking device described in this work.

All activities within the proton-neutron spin physics program can also be seen as first important steps towards the Polarised Antiproton eXperiments (PAX) [7] at the future Facility for Antiproton and Ion Research FAIR [8] at GSI.

1.1 Physics Motivation

The deuteron, with a binding energy of roughly 2 MeV compared to the masses of its constituent nucleons of about 939 MeV, is a very loosely bound object. This becomes also apparent from the diameter of the deuteron of roughly 4 fm [9] while the proton and neutron have a diameter of only 1.3 fm. At typical COSY momenta of for instance 2 GeV/c, the DeBroglie wave length of a proton is

$$\lambda = \frac{h}{p} = \frac{4.136 \cdot 10^{-15}\,\text{eV} \cdot \text{s}}{2 \cdot 10^9\,\text{eV/c}} \approx 0.6\,\text{fm} \tag{1.1}$$

which is below the diameter of the deuteron. This simple estimate indicates, that at COSY energies it is possible to not only initiate the reactions on the deuteron itself,

Figure 1.1: Simple sketch of the spectator model. A beam proton impings on the the target neutron. The proton within the deuteron becomes the spectator which has the opposite momentum of the neutron.
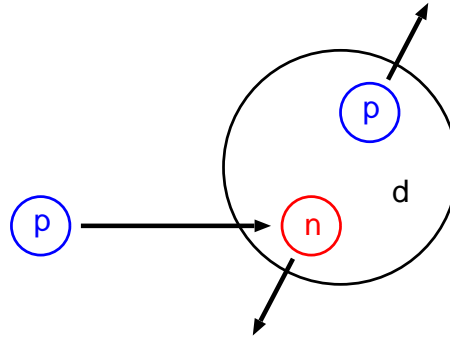
but to also probe its constituent protons and neutrons.

A very naive sketch of the spectator model [10] is shown in figure 1.1 in which a beam proton impinges on the target deuteron and reacts with the constituent neutron leaving the proton untouched. By identifying the proton, precisely measure its energy and direction, its four-momentum[1] is known. With the knowledge of the spectator four-momentum also the momentum of the neutron is known and it becomes possible to tag the reaction to the neutron and enable the use of deuterons as an effective neutron target. In a most general form such reactions can be expressed by

$$p + d \rightarrow X + p_{spectator} \tag{1.2}$$

in which X are the particles in the final state and $p_{spectator}$ is the spectator proton. In the spectator model, the neutron on which the reaction occured has the opposite momentum of the detected spectator proton, which follows the Fermi momentum distribution shown in figure 1.2(a). With this assumption equation 1.2 can be rewritten as

$$p + n \rightarrow X \tag{1.3}$$

with the four-momentum vector of the target neutron being

$$n^{\mu} = d^{\mu} - p^{\mu}_{spectator} \tag{1.4}$$

From equation 1.4 it is apparent that the mass of the target neutron strongly depends on the kinetic energy of the detected spectator proton. The effective mass of the target neutron is the given by

$$m_n = \sqrt{m_d^2 + m_p^2 - 2m_d(m_p + T_{spectator})} \tag{1.5}$$

in which $T_{spectator}$ is the kinetic energy of the spectator proton. With m_n^0 being the neutron mass for $T_{spectator} = 0$ equation 1.5 becomes

---

[1]from here on, four-momentum vectors will be denoted by a superscript μ.
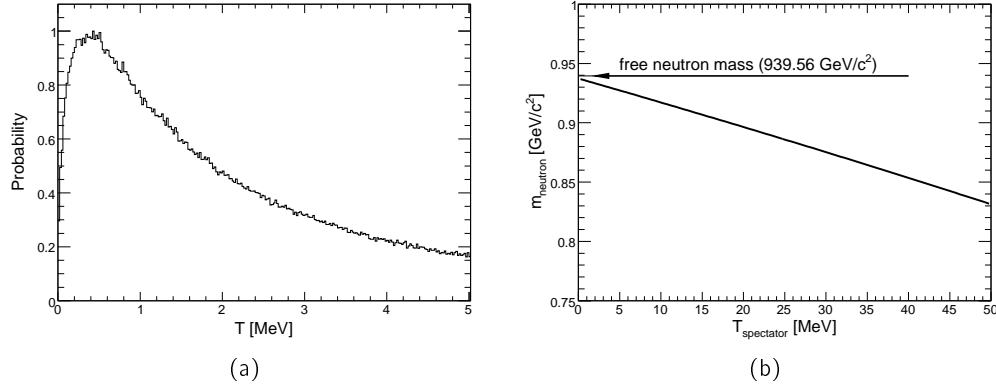
Figure 1.2: (a) Fermi distribution of kinetic energies of the nucleons within a deuteron. (b) Mass of the target neutron as a function of kinetic energy of the spectator proton. The detection threshold of the presented detection system is indicated by arrows.

$$m_n = m_n^0 \sqrt{1 - \frac{2m_d}{(m_n^0)^2} \cdot T_{spectator}} \tag{1.6}$$

with $m_n^0 \approx 937\,\mathrm{MeV}$. From equation 1.6 it is evident, that in the spectator model the neutron in the initial state never has the mass of the free neutron. The neutron mass as a function of the kinetic energy of the spectator is shown in figure 1.2(b).

With the knowledge of the four-momentum of the spectator proton one can calculate the center-of-mass energy $\sqrt{s}$ in the pn-system

$$\sqrt{s}_{pn} = \sqrt{\left(p_{beam}^\mu + d_{target}^\mu - p_{spectator}^\mu\right)^2} \tag{1.7}$$

on an event-by-event basis.

A special case of the reaction shown in equation 1.3 is the meson production on the neutron with a deuteron and one or several mesons in the final state. In this case the excess energy Q is given by

$$Q = \sqrt{s}_{pn} - \sum_k m_k \tag{1.8}$$

in which m_k are the masses of the particles in the final state. By selecting the spectator proton at certain angles it is possible to scan Q at fixed beam energies. It is therefore for instance possible to measure below and above the production threshold of a certain meson.

Previous measurements with a test version of the detection setup [11] at ANKE have shown that the described method may very well be used to investigate the meson production in proton-neutron collisions. A dedicated test of this method has been performed at a proton beam momentum of $1.2\,\mathrm{GeV/c}$ with the reaction $pn \rightarrow d\pi^0$ [11].

The total cross-section of the reaction $pn \rightarrow d\omega$ has been determined in two Q bins from $8-44$ MeV and $42-78$ MeV [12, 13], while the η production has been investigated at beam momenta of 2.055 GeV/c and 2.095 GeV/c [14].

1.2   Vertex Reconstruction

Up to now all experiments at ANKE have been conducted with either heavy strip targets or a hydrogen or deuterium cluster jet target. In both cases the center target region is well defined by the geometry of the setup and has an extension of about 10 mm. In the analysis the center of the region is used as a start point of the tracks in the ANKE detection systems and is essential to the momentum reconstruction.

With the installation of the polarized internal target at ANKE the situation has, however, become more difficult. The storage cell of the PIT is basically an about 40 cm long tube with a rectangular shape with an edge length of 20 mm, that is filled with polarized protons or deuterons by the atomic beam source ABS [15]. The ABS can produce beams with an intensity of up to $5 \cdot 10^{11}$ particles per cm^2. Compared with the cluster target that has an intensity of 10^{14} particles per cm^2, the intensity of the ABS is about 200 times smaller. Although measurements with the atomic beam are possible, it is preferable to use an extended target storage cell to increase the effective intensity and thus the luminosity by about a factor 100. This means that also the reaction vertices are distributed non-uniformly over the full length of the cell along the beam axis. Moreover with the storage cell being open on both ends, it is even possible to have reactions on the residual target gas at distances of up to several meters up and downstream from the storage cell. This has been shown from first cell tests, in which the count rate when the beam has been directed through the filled storage cell has been compared with the count rate when the beam has been directed aside the cell. The count rate on the residual gas is only four times less than the one obtained when the beam goes through the cell [16]. Moreover, measurements at the electron cooler that is located at a distance of 8 m upstream from ANKE have shown residual gas even there [17].

Under such conditions, the existing ANKE tracking detectors are not capable of reconstructing the true vertex of a reaction. Additional near target tracking detectors, which should be as close as possible to the storage cell, are required. Each track in such a vertex detector defines a line on which the vertex lies. In the energy range in which the tracking detector will be mostly used, the precision with which one is able to obtain this line is dominated by the angular straggling of the particles in the detector and in the order of 1 mm. With a second track in the same or additional detectors it should be possible to determine the vertex in all three coordinates with a resolution of 1 mm.

In section 7.4 on page 95 a first attempt to obtain a vertex in all three coordinates is presented. There, a particle track in the described tracking telescope, which is only sensitive to the y and z-coordinates of the vertex, is intersected with a track in the ANKE forward detection system (x) to obtain a vertex. It will be shown that the

position resolution in the coordinate perpendicular to the beam (x), which is determined by the ANKE forward detector, is only in the order of 9 mm for this reconstruction method. With the dimension of the used storage cell it is apparent that it is nearly impossible to distinguish between hits of the beam on the wall of the cell and hits on the actual target gas.

For maximum efficiency the tracking devices also need to provide a trigger signal which allows in coincidence with the trigger signal from the other ANKE detection systems the significant reduction of the number of background events originating from outside the target cell (up and down-stream of the beam). Moreover, depending on the investigated physics, the device must be capable of generating triggers even for minimum ionizing particles. The self-triggering option is thus indispensable for measurements that only involve these near target tracking telescopes such as the beam polarization measurements.

1.3   Polarimetry

With the start of the single and double polarized experimental program at ANKE the beam and target polarizations have to be measured. For the measurement of the target polarization a dedicated Lamb-shift polarimeter [18, 19] has been built and will be installed underneath the target storage cell. For the determination of the beam polarization the EDDA experiment [20, 21] and a dedicated Low Energy Polarimeter (LEP) [22, 23] are available. Both EDDA and the LEP however measure the beam polarization on a CH_2-foil target which essentially heats the beam and deteriorates its properties. Moreover, the EDDA polarimeter, which is also capable of determining the tensor polarization of a deuteron beam, is limited to beam intensities of $< 10^9$ particles in the ring. An independent and parasitic measurement of the beam polarization at ANKE is therefore desirable. With the use of several tracking telescopes, like the one presented in this work, dedicated coincidence triggers from these telescopes and a large coverage of the storage cell to the side and the forward direction, it will be possible to identify the polarimetry reactions and determine the beam polarization without disturbing any ongoing measurements.

With the data obtained during a beam-time in November of 2003 it was possible to use a prototype of the described setup to extract the analyzing powers for dp-elastic and quasi-free pp and np elastic scattering. The results are shown in chapter 7.

Chapter 2

Experimental Setup

The presented detection system has been developed for the ANKE magnetic spectrometer at the COoler SYnchrotron COSY of the Research Centre Jülich. As an extension of ANKE it will serve as a low energy spectator proton and vertex detector as well as an independent beam polarimeter.

In this chapter, COSY and the ANKE spectrometer are outlined. Later, an overview of how a possible extensions of ANKE by near target tracking detectors could look like.

2.1 COSY

COSY is a so called COoler SYnchrotron that provides unpolarized and transversely polarized proton and deuteron beams in a momentum range from 300 MeV/c to 3.7 GeV/c. Electron cooling is available up to a momentum of 600 MeV/c while for high momentum beams in the range from 1.5 GeV/c to 3.7 GeV/c stochastic cooling is possible. Figure 2.1 shows COSY and the injector cyclotron JULIC together with some of the internal and external experiments. The polarized or unpolarized beam particles originating from a particle source underneath the cyclotron are injected into the cyclotron where they are accelerated up to the COSY injection energy of 45 MeV. From there the particles are transported into COSY. Table 2.1 shows the maximum and typically achieved fillings of the COSY ring and where applicable the maximum and

Beam	Maximum Filling [particles]	Typical Filling [particles]	Maximum Polarization [%]	Typical Polarization [%]
p	$1.4 \cdot 10^{11}$	$1.4 \cdot 10^{11}$	—	—
$\vec{p}$	$1.0 \cdot 10^{10}$	$1.0 \cdot 10^{10}$	85	$70 - 80$
d	$1.3 \cdot 10^{11}$	$1.3 \cdot 10^{11}$	—	—
$\vec{d}$	$6.0 \cdot 10^{9}$	$6.0 \cdot 10^{9}$	75	70

Table 2.1: Maximum and typically achieved fillings (number of particles stored in the ring) and degrees of polarization of COSY for different beam types.
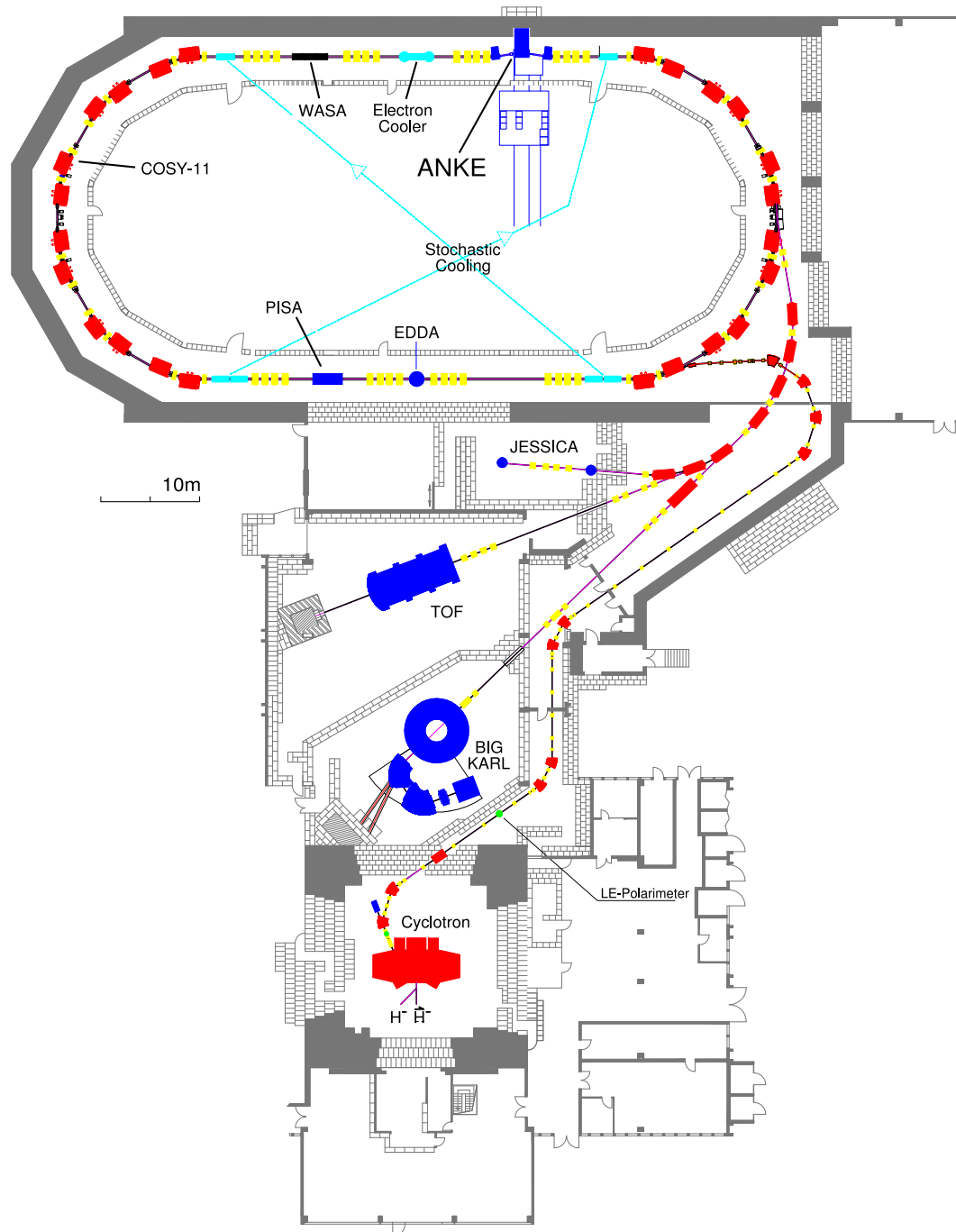
Figure 2.1: Floor plan of the COoler SYnchrotron COSY-Jülich with some of the internal and external experiments and the JULIC cyclotron.
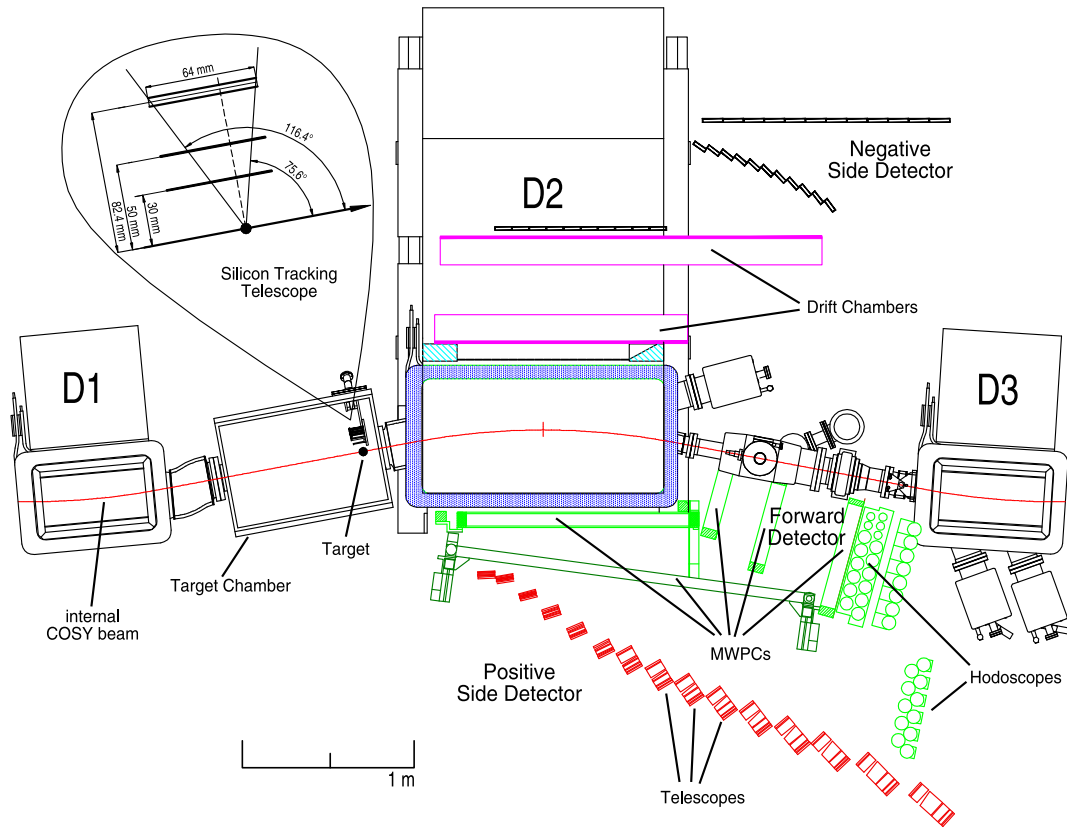
Figure 2.2: Drawing of the ANKE spectrometer with its three magnets and the side (positive and negative), forward and backward detection systems.

typical degrees of polarization for the different types of beams [24]. For unpolarized beams the maximum number of particles in the ring is in the order of $1.3 - 1.4 \cdot 10^{11}$. The polarized beams have roughly 15 times less intensity for protons, and 20 times less particles for deuterons. The circulating beam can be used in internal experiments such as ANKE, WASA, COSY-11, PISA and EDDA, or extracted and delivered to the external target locations (TOF, MOMO, GEM, NESSY and JESSICA).

2.2 ANKE Spectrometer

The ANKE spectrometer is located at one of the internal target positions of COSY. It consists mainly of three dipole magnets (D1 - D3) that introduce a closed orbit bump of the circulating beam. The use of three magnets and the fact that the main spectrometer magnet D2 is movable perpendicular to the beam axis allows one to vary the momentum range covered by the ANKE detection systems independent on
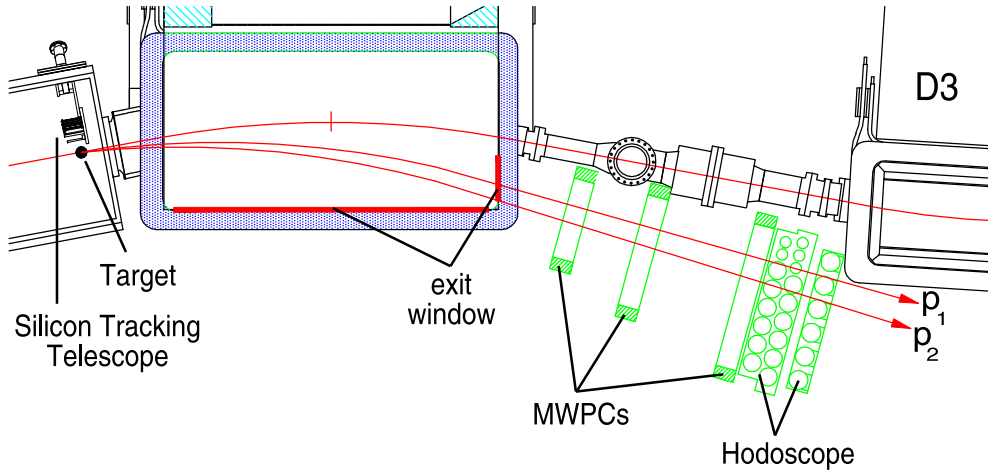
Figure 2.3: Expanded view of the target region and the forward detection system.

the beam energy. Figure 2.2 shows ANKE with its magnets D1, D2 and D3. The detection systems of ANKE comprise tracking detectors and scintillator hodoscopes in forward direction and both to the left (negatively charged reaction products) and to the right (positive particles) of the beam. In addition dedicated range telescopes and Cerenkov counters are installed in order to identify rare events involving particles such as the K^+.

With the data obtained by the multi-wire proportional chambers and the scintillation counters a track can be reconstructed back to the vertex, which in case of a strip or cluster jet target is a fixed point and well known. For an extended target such as the PIT the vertex has to be determined with the help of near-target tracking detectors. The track information and the knowledge of the magnetic field in D2 can be used to reconstruct the momentum of the particle. For the positive and negative side detectors additional time of flight information is available that allows the distinction between different types of particles. An expanded view of the target and forward region of ANKE is shown in figure 2.3. The tracking telescope presented in this work is shown at its mounting position in the target chamber.

2.3   Tracking Detectors for ANKE

Figure 2.4 shows the artist view of a possible extension of the ANKE spectrometer by near target tracking detectors. Three layers of double-sided silicon strip detectors, arranged in a telescope structure, are placed around the storage cell. In the figure, four of those telescopes, two to each side of the cell, are shown. The modular design allows one to change the placement of these telescopes depending on the requirements without having to redesign the whole detection system. Moreover, the modular design of the telescopes itself gives also the possibility to change the detector configuration
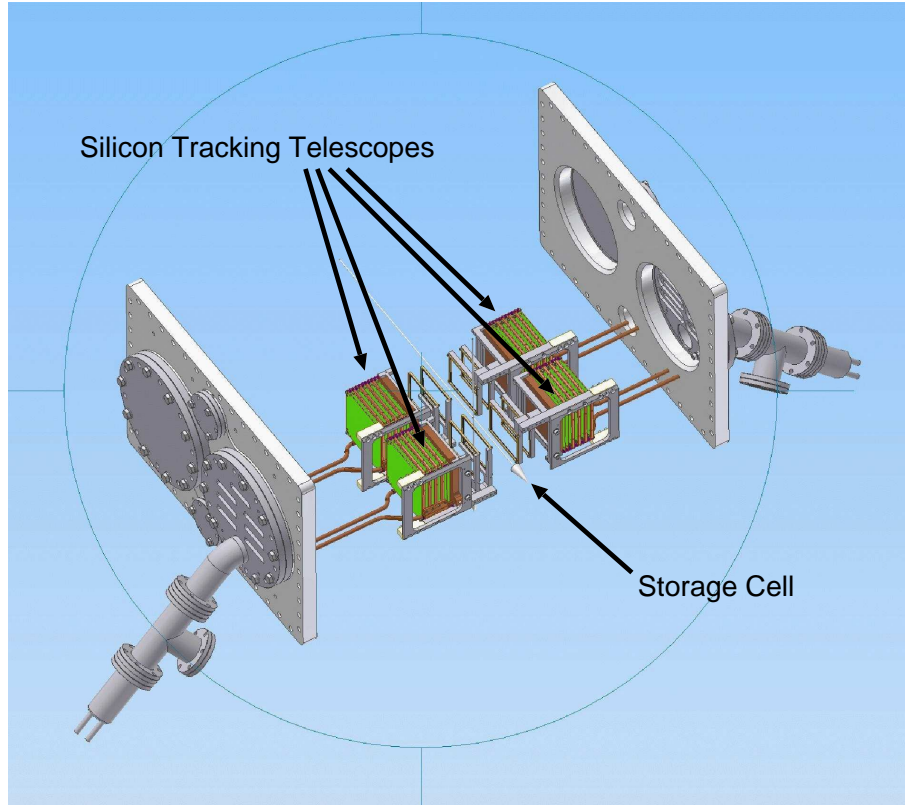
Figure 2.4: Artist view of a possible arrangement of four silicon tracking telescopes around the ANKE storage cell.

within a telescope. For the beam polarimetry for instance, one would place additional telescopes in the forward direction of the storage cell in order to identify the ejectiles of the chosen polarimetry reaction solely in the telescopes.

In the following chapters, the design of one telescope, its dedicated read-out electronics and the energy measurement and tracking are described. The work concludes with the first results obtained from data taken with one telescope, and an outlook on the possible improvements of the detection system.

Chapter 3

Silicon Tracking Telescope

The requirements of having particle identification together with a precise energy determination and tracking with a vertex resolution of 1 mm suggests the use of several layers of double-sided silicon detectors installed inside the accelerator vacuum and arranged in a telescope structure. In general, the Silicon Tracking Telescope has to provide

- **particle identification for protons and deuterons**
  Protons and deuterons have to be identified via the $\Delta E/E$-method over an energy range from 2.5 MeV to ≥ 40 MeV with a resolution of $150 - 250$ keV.

- **tracking of particles**
  Tracking of particles must be provided with an angular resolution in the range from $1°$ to $6°$ (FWHM). For stopped protons and deuterons the resolution depends on the angular straggling and therefore the particle energy while for minimum ionizing particles the resolution is determined by the strip pitch of the used detectors and the distance between them.

- **a trigger signal within 100 ns of the particle passage**
  This allows one to use the detection system stand-alone and to set timing coincidences with other ANKE detector components. The self-triggering capabilities of the telescope are essential for the polarimetry studies, where two or more telescopes will be placed close to the side and the forward direction of the target and used to identify the polarimetry reaction. Moreover, the trigger signal in coincidence with the triggers from other ANKE detection system will significantly reduce the amount of background events.

- **maximum possible modularity**
  Depending on the field of operation and the range of kinetic energy the telescope has to cover, it is desirable to have a modular system that allows an easy exchange of detectors and electronics. In addition this will make the maintenance of the telescope less difficult.

To fulfil these requirements, the telescope will be equipped with three layers of double-sided silicon detectors, a thin 69 μm first layer, a 300 μm or 500 μm intermediate layer and a thick ($\geq$ 5 mm) last layer. The detection threshold is set by the thickness of the first layer. For a 69 μm detector it is in the order of 2.5 MeV for protons and 4 MeV for deuterons. Since the particle has to be stopped in one of the rear detection layers to enable the $\Delta E/E$-method, the maximum energy for protons that can be identified is then in the order of $\geq$ 32 MeV. For deuterons it is $\geq$ 43 MeV.

For the inner detectors of the telescope an effective strip pitch of $\approx$ 400 μm has been chosen for optimized tracking resolution while for the last layer the pitch is 666 μm. For two low energy protons detected in the same or different telescopes, the vertex resolution is then about 1 mm.

Due to a vacuum break at the beginning of the data taking period the bonds connecting the strips of the available 300 μm detectors to the read-out electronics were damaged. The data presented in this work have therefore been taken with just a 69 μm silicon detector and a 5.1 mm Si(Li) detector.

3.1   Silicon Detectors

The silicon detectors that are used in the tracking telescope can be logically split into two groups. For the inner two layers (69 μm to 500 μm) the pitch of the detectors has been chosen to be in the order of 400 μm in order to fulfill the tracking requirements. In standard configuration, the outermost detector ($\geq$ 5 mm) is used to stop particles, precisely measure their energy loss and validate the tracks determined for the position information from the two inner layers.

3.1.1   The BaBar IV Detectors

The BaBar IV detector, which will be used for the first two layers of the tracking telescope, has been originally designed for the BaBar experiment [25, 26, 27] at the SLAC PEP-II B factory [28] by the British company Micron Ltd. [29]. The size of the active area of this so called BaBar IV detector makes it however also suitable for the telescope. In addition the reuse of already existing masks and production facilities makes the choice of the BaBar IV detector cost efficient. To provide AC-coupling for each strip already on the detector, an additional mask is vacuum metallized onto both sides. The detector can be produced in thicknesses from 69 μm to 500 μm. On the p-doped side the detector has 1023 strips and on the N side it has 631 strips[1], all of which are capacitively coupled to the bond pads that are used to connect the strips to the electronics.

To increase the effective strip pitch to about 400 μm a rather complicated connection scheme is required. Figure 3.1(a) shows this scheme for the P side of the BaBar

---

[1]Positive charge signals are obtained from the p-doped side of a silicon detector, whereas negative charge signals are obtained from the n-doped side [30]. From here on, when referring to polarities, always the signal polarity is meant and not the doping of the detector.

Figure 3.1: Geometry and connection scheme of the P (a) and N (b) sides of the BaBar IV detector.
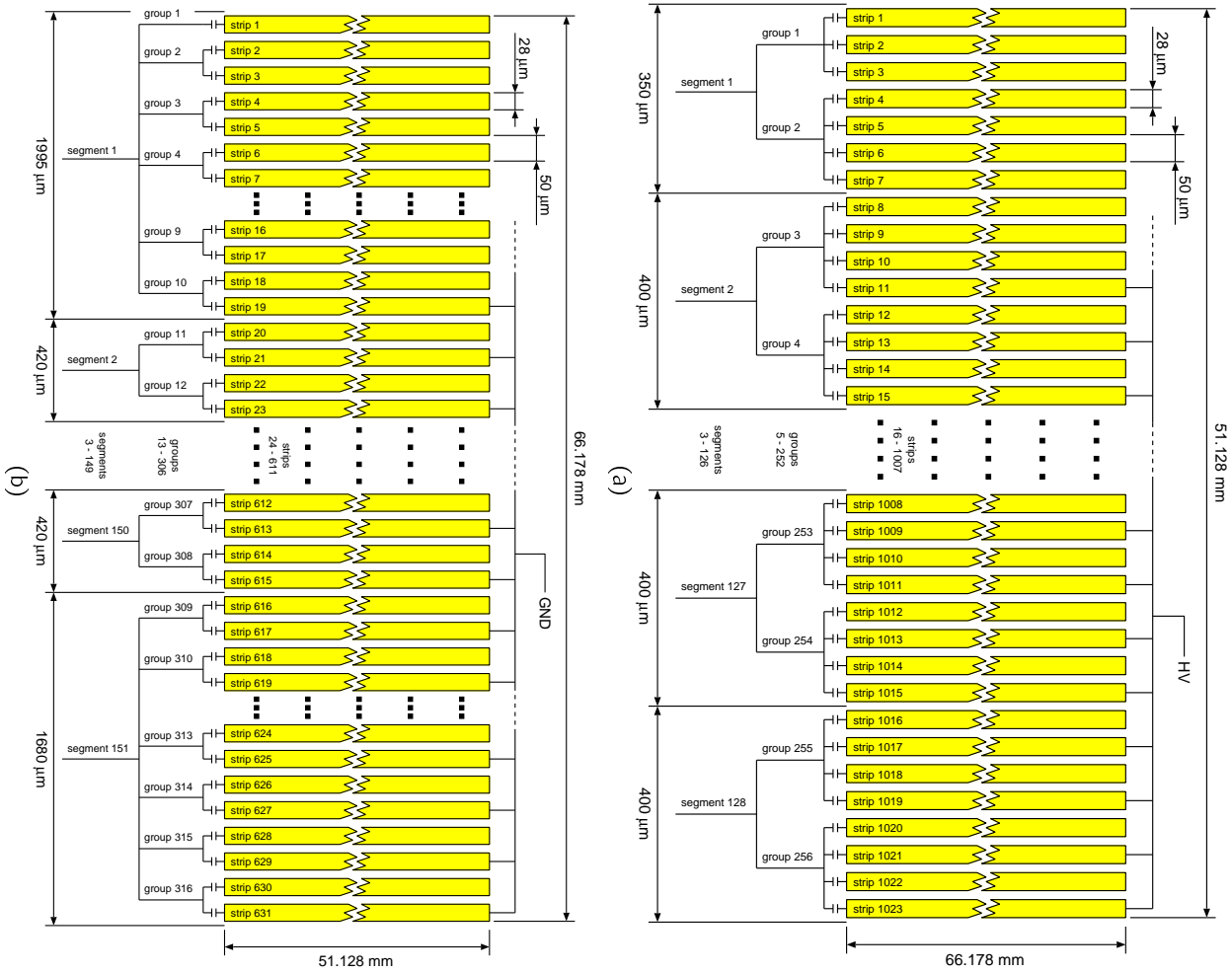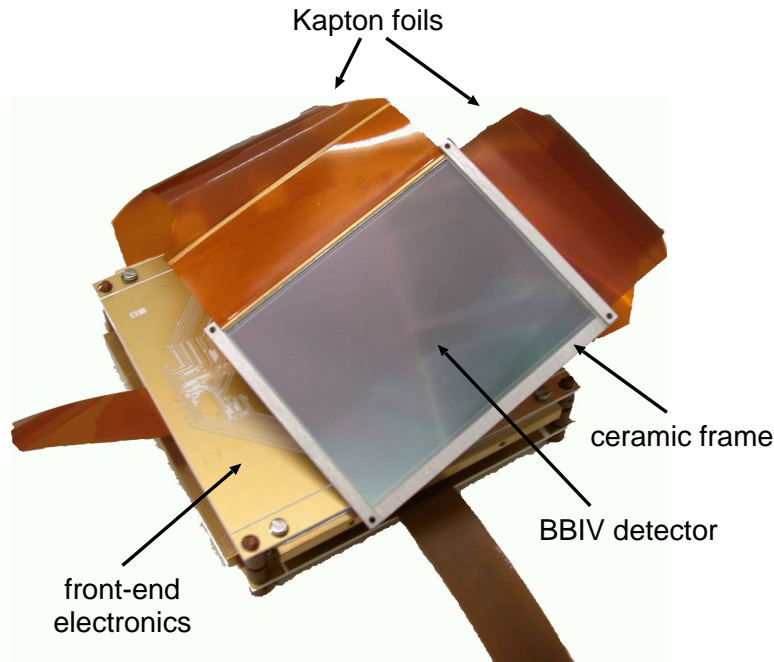
Figure 3.2: Photograph of the BaBar IV detector in its ceramic frame on top of stack of two front-end electronics boards. The detector is connected to the electronics via the Kapton foils.

IV detector. On the detector the strips are combined to groups of four strips with the first group consisting of three strips. On the Kapton [31] foil that is used to connect the detector to the front-end electronics these 256 groups are again combined to 128 segments by bonding two groups to one segment on the Kapton foil. On the N side of the detector the strips are combined in groups of two strips with the first strip being a single group resulting in 316 groups of strips. On the Kapton foil the first 10 groups are combined to the first segment, followed by 149 segments made up of two groups. The last segment (151) is a combination of the last 8 groups (309 through 316). The detailed scheme is shown in figure 3.1(b). A picture of the BaBar IV detector in its ceramic frame is shown in figure 3.2.

3.1.2 The thick Lithium drifted Detector

The thick Lithium drifted Silicon detector $(Si(Li))^2$ is a development of the detector laboratory of the Nuclear Physics Institute (IKP) of the Research Centre Jülich (FZJ). The available detector has a thickness of approximately 5.1 mm, 64 by 64 mm active area and 96 strips on both detector sides with a pitch of 666 μm [32]. Figure 3.3 shows

---

[2]On the Lithium side of a Si(Li) detector negative charge signals are obtained, while the positive charge is collected on the Boron implanted side.
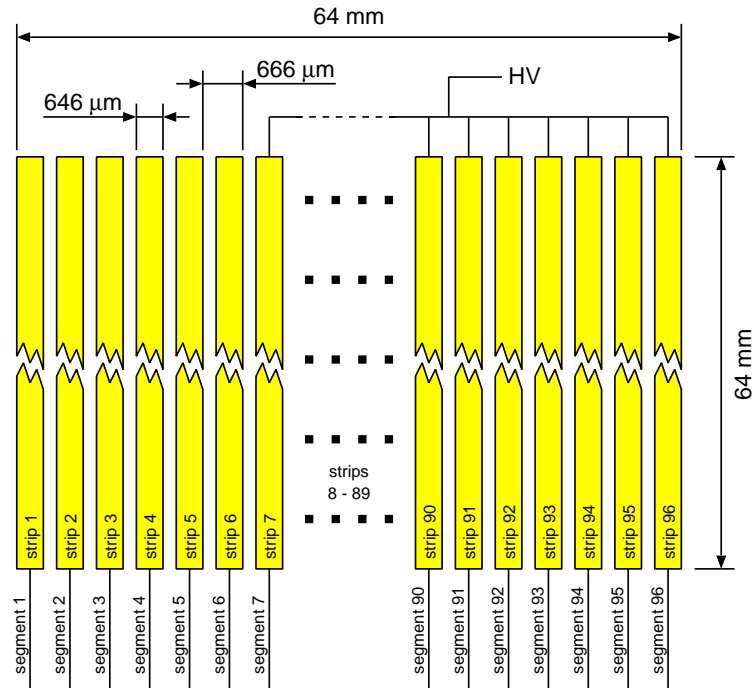
Figure 3.3: Geometry and connection scheme for both sides of the Lithium drifted Silicon Si(Li) detector.

the layout of one side of the detector. Compared to the thin BaBar IV detector the connection of the 96 strips to the inputs of the front-end board is straight forward and also shown in the figure. Although the voltage to achieve full depletion of the detector is in the order of 300 V, bias voltages of up to 1 kV are preferable to minimize the charge collection time. Even with the large input range of the front-end amplifier chips an in-vacuum capacitive divider board is necessary to match the detector signal to the input range of the electronics. In addition the board decouples the signals from the high voltage side of the detector. Figure 3.4 displays a picture of the Aluminum frame holding the thick detector. The detector is fixed to the frame by holding brackets made of Vespel.

Recent investigations at the detector laboratory have shown that the Si(Li) detectors can be produced with thicknesses of 10 mm and more [33]. The use of these detectors as a last detection layer in the tracking telescope extends the range of operation to 46 MeV for protons and 62 MeV for deuterons.

3.2 Front-end Electronics

With the maximum number of channels for a single detector side of 151 and a total number of 471 channels for a telescope equipped with one BaBar IV and one Si(Li)
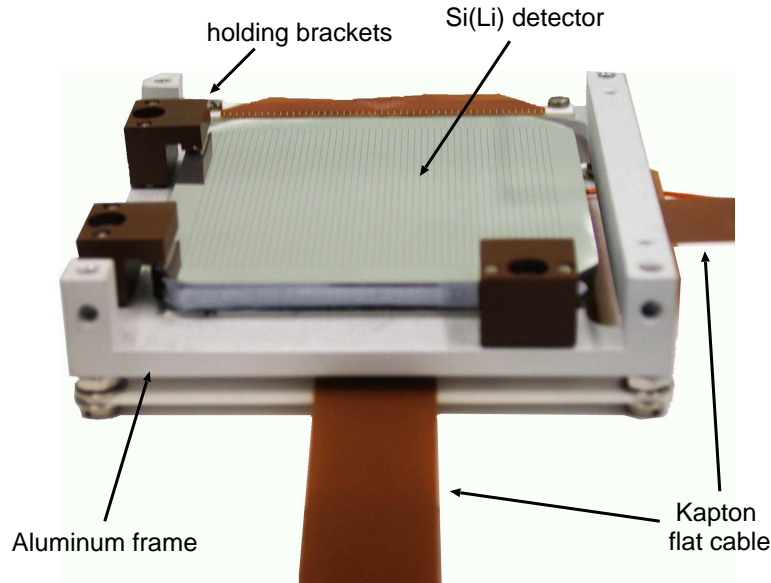
Figure 3.4: Picture of the Si(Li) detector mounted in an aluminum frame.

detector it becomes apparent, that an integrated read-out system is required to minimize the number of vacuum feed-throughs and the number of amplifiers. For this purpose a vacuum compatible front-end board has been developed. On the input side it is equipped with three 51 pin Hirose connectors [34]. Two of the 153 possible inputs are used for the bias and ground connection leaving 151 inputs that may be connected to the strips or segments of a detector.

To meet the requirement of having a single type of electronics board handle the signals from a variety of detectors ranging from 4 MeV for protons in a 69 μm Silicon detector to about 40 MeV for deuterons in a 5 mm thick Si(Li) detector together with a low trigger threshold of 100 keV, the VA32TA2 [35] front-end chip has been developed together with the Norwegian company IDE AS. The chip is an enhancement of the VA32HDR [36, 30, 37] preamplifier chip and the TA32cg [38, 30, 37] trigger chip combined on a single die which eliminates the bond connections between the two chips. A block scheme of the VA32TA2 is shown in figure 3.5. A photograph of the front-end board equipped with five chips is shown in figure 3.6.

The VA32TA2 has 32 identical channels which can be logically split into an amplitude and a trigger part. A charge signal provided on the input pad of a channel is amplified in the preamplifier stage. After the preamplifier the signal is split into two branches, an amplitude part and a trigger part.

In the slow branch, the amplitude part of the chip, the signal is fed to the slow shaper. Once a readout cycle is started by applying the "hold" signal (time line D in figure 3.7), the output of each of the 32 slow shapers is stored in the sample and hold facility. With both the "shift_in" (time line E) and the "clk" (time line F) signal active
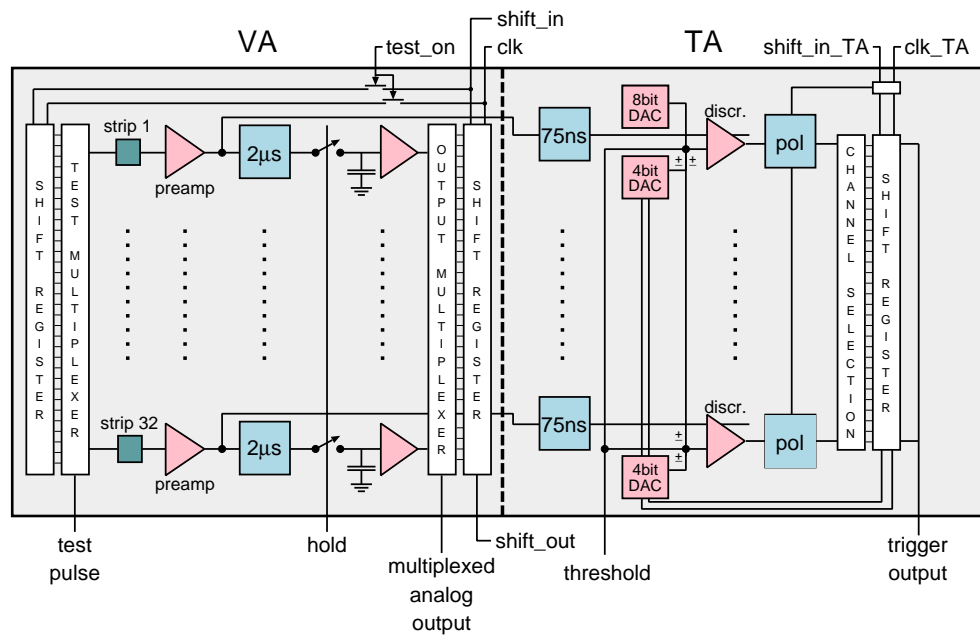
Figure 3.5: Block scheme of the VA32TA2 front-end amplifier chip.
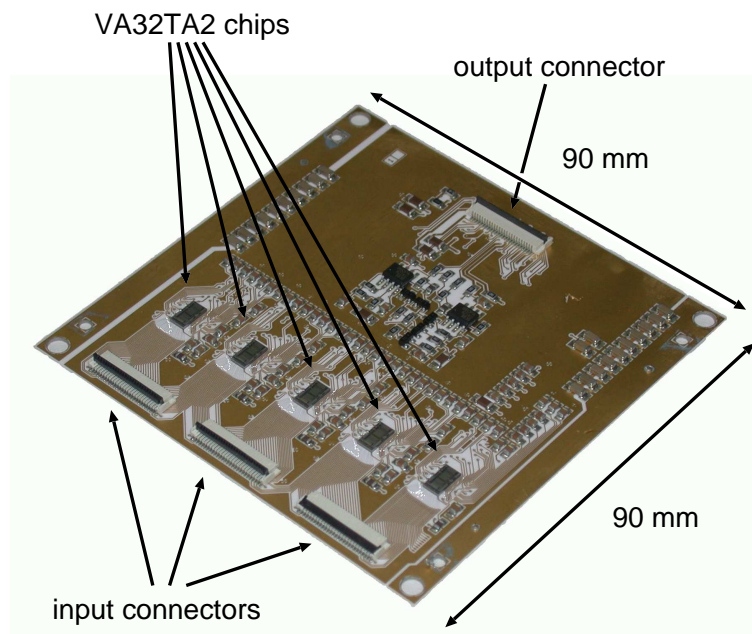
Figure 3.6: Picture of the in-vacuum front-end electronics board showing the three input connectors, the five VA32TA2 front-end chips as well as the output connector.
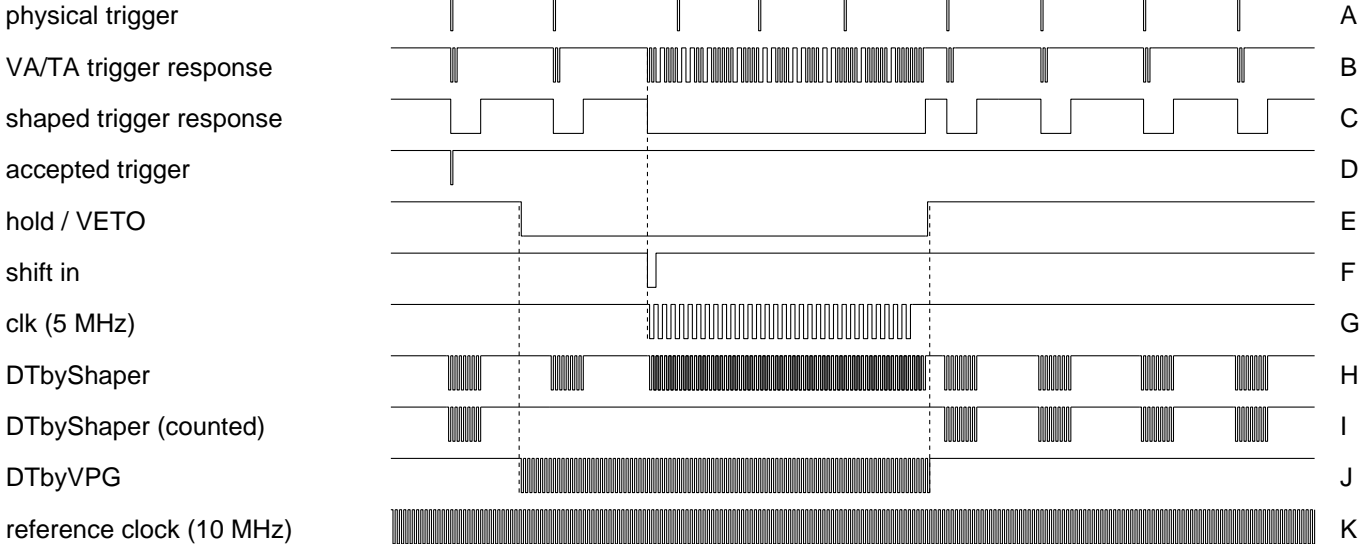
Figure 3.7: Timing diagram of the digital signals of the front-end electronics and the data acquisition system.

physical trigger	A
VA/TA trigger response	B
shaped trigger response	C
accepted trigger	D
hold / VETO	E
shift in	F
clk (5 MHz)	G
DTbyShaper	H
DTbyShaper (counted)	I
DTbyVPG	J
reference clock (10 MHz)	K

Die size	6300 μm x 3310 μm	
Channels	32	
Power Supply Power Dissipation	2 V 96 mW (3 mW/channel) (quiescent)	
Linear Range	139 MIPs (1 MIP = 3.6 fC)	
Peaking Time	VA	2 μs
	TA	75 ns
Gain Noise	$\approx$ 0.8 mV/fC 710 + 3 electrons/pF	

Table 3.1: Summary of the features and specifications of the VA32TA2 front-end amplifier chip.

one bit is inserted into the read-out register which switches the first channel of the output multiplexer to the output bond pads. By clocking the "clk" control signal the bit is moved through the register switching the channels step by step to the output. According to the specifications, the maximum clock frequency is 10 MHz, although only 5 MHz have been confirmed by the measurements. Each channel is therefore for a minimum time of 100 ns[3] applied to the output of the chip. The output of the shift register is in addition provided on a "shift_out" bond pad allowing to build a daisy-chain of chips. Up to ten chips can be connected to a daisy chain allowing a maximum number of 320 inputs to be read out. To build a chain of chips, the control signals have to be provided to all chips simultaneously and the output of the shift register of a chip has to be connected to the "shift_in" input of the next chip in the chain.

In the trigger part of the chip, the fast branch, the signal from the preamplifier stage is shaped with a peaking time of 75 ns. The output of this fast shaper is compared with a threshold giving the opportunity to obtain a trigger signal from the chip. The individual threshold for each channel is made up of an external voltage, a per chip offset voltage and a per channel offset. Both the per chip and per channel offset voltages can be controlled by an additional slow control shift register. It is also possible to mask out certain channels from the trigger pattern. The shift register is controlled by two signals similar to the control lines of the read-out shift registers inside the amplitude part of the chip. These signals are the "clk_TA" and "shift_in_TA".

When used in a daisy chain it is likely that the average output level of the chips varies over a wide range. In order to minimize that range each chip has an additional 7 bit DAC that allows the shift of the average output level of each chip individually. The DAC is an extension of the slow control shift register and is also controlled by the "clk_TA" and "shift_in_TA" signals. Table 3.1 summarizes the main features and specifications of the VA32TA2 and figure 3.7 shows the timing diagram of a read-out sequence.

Each of the front-end boards is equipped with 5 VA32TA2 chips in a daisy chain. Since

---

[3]Throughout all the measurements a frequency of 5 MHz (200 ns active phase) has been used.

the board only allows the connection of 151 detector segments, 9 of the 160 available chip inputs are not used and left floating.

3.3   Interface

A second front-end board serves as an interface between the in-vacuum electronics and the data acquisition system. Its main purpose is to optically decouple the in-vacuum electronics, which might be on high voltage[4], from the read-out electronics. The board receives the digital slow control and read-out signals via a common bus from the DAQ and provides them to the VA32TA2 chips on the front-end boards. It is also equipped with an eight channel 12 bit DAC which is used to generate the bias voltages for the chips as well as the common threshold for one detector side. In order to allow individual trigger mask and voltage settings each interface board is addressable via the control bus. A second stage adjustable amplifier provides the amplitude signals as a differential signal on two LEMO connectors. The trigger output of the chips can be taken from a LEMO connector as well. In order to allow one to set an individual delay between the trigger and the generation of the "hold" signal a voltage input is provided on each interface board. It permits to add a precisely adjustable delay between the incoming "hold" from the DAQ and the outgoing "hold" signal to the VA32TA2 chips. A simplified connection scheme of the front-end electronics is shown in figure 3.8.

3.4   Assembly

On the front-end side the whole detection system is designed in such a way that all components of the telescope are mounted on a single CF160 flange. Inside the vacuum a stainless steel pole is used as support for both the detectors and the read-out boards. At the end of the pole, where the detector frames are mounted, special positioning holes have been drilled. The holes have a distance of 20 mm to each other and allow the placement of the detectors at different, but precisely reproducible positions. The in-vacuum electronics boards are mounted behind the detectors. Each board is shielded by a copper plate to minimize distortions and is thermally connected to a cooling head via copper foils. The cooling is required since the total power consumption of the electronics for the telescope equipped with two detectors is about 1800 mW and a constant temperature of the equipment is desirable for stable operation. In addition cooling is required for the thick detector because the leakage current of the detector and thus its power consumption increases exponentially with temperature. This positive feedback would lead to severe damage of the detector if used without cooling. For this purpose copper foils have also been used to thermally connect the frame of the thick detector to the cooling head. For temperature monitoring a Pt100 sensor has been mounted on the mounting pole close to the electronics.

---

[4]The front-end electronics lies on the same potential as the connected detector side which means that for each detector one board is on high voltage.

HV
10 - 150 V

65/300/500 µm
Si detector

GND

HV
0.5 - 1.5 kV

5 - 10 mm
Si(Li) detector

GND

capacitive
divider and
decoupling

capacitive
divider and
decoupling

front-end
board

front-end
board

front-end
board

front-end
board

CF 160 Flange

Interface

Interface

Interface

Interface

signal decoupling

+ −

+ −

+ −

+ −

digital control

analog detector signals

Trigger

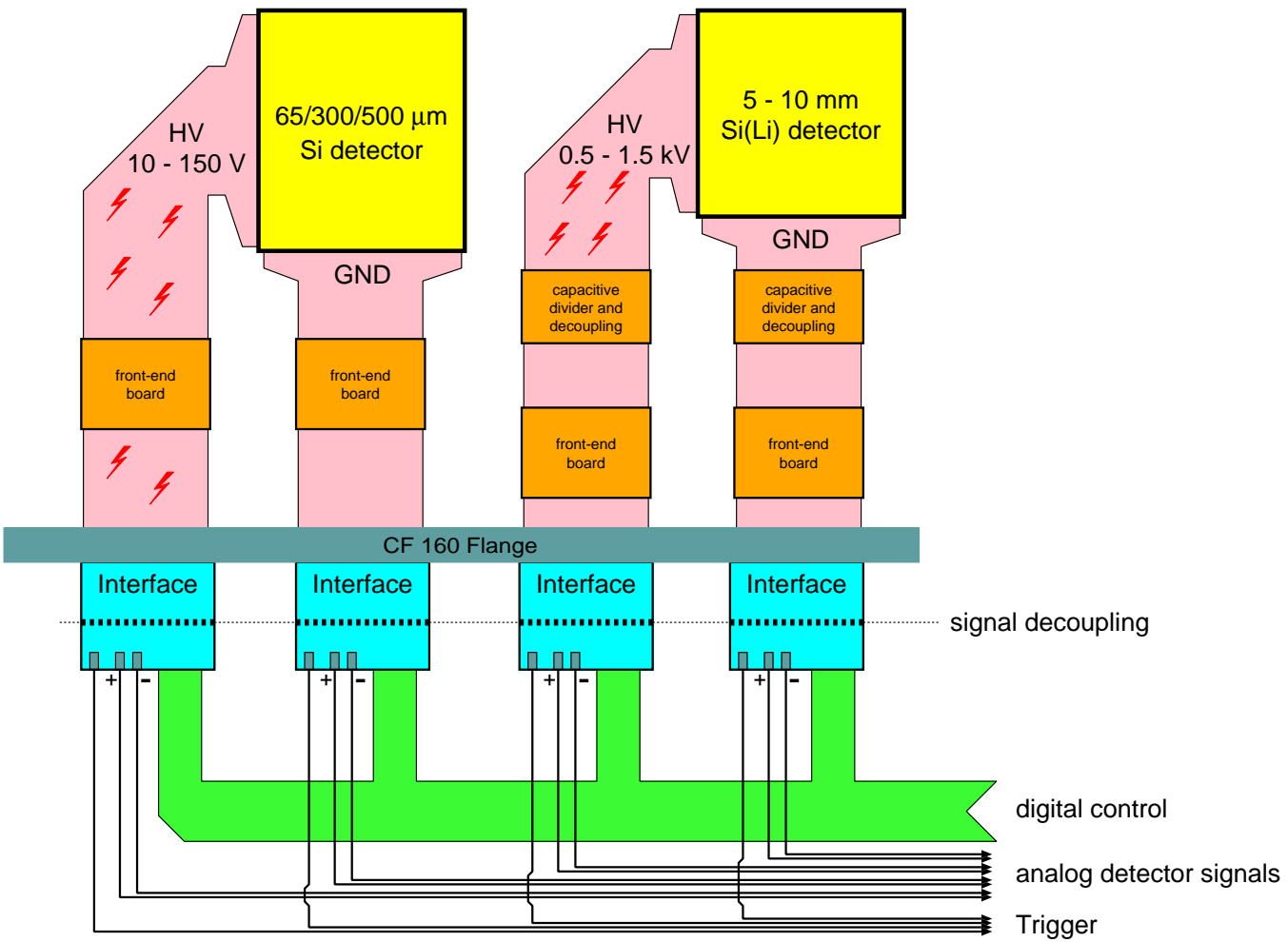Figure 3.8: A simplified connection scheme of the tracking telescope equipped with two double-sided detectors. On the interface boards the digital control signals are optically decoupled from the high voltage level inside the vacuum. Due to lack of adequate analog opto-couplers, the analog detector signals are AC coupled from the vacuum side to the outside with an additional base line restorer.
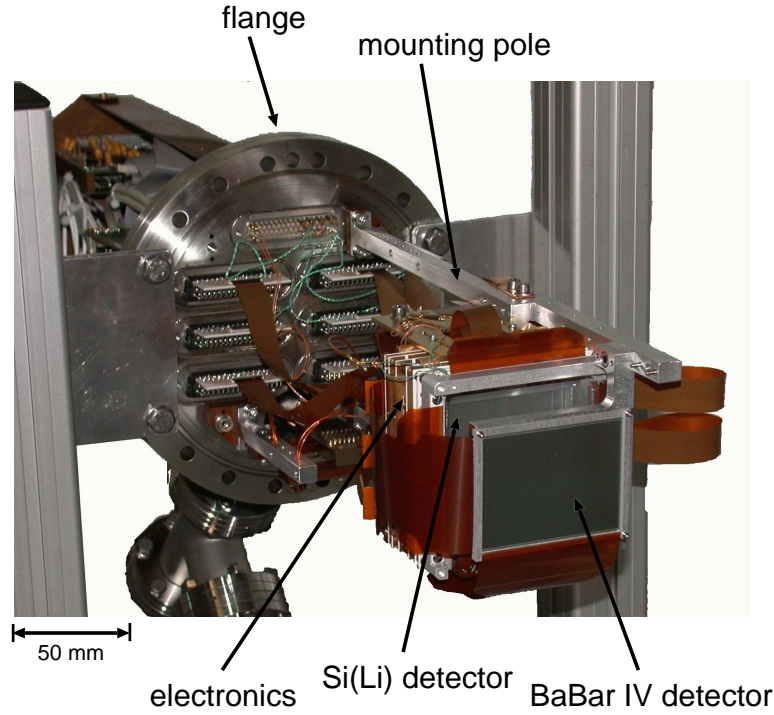
Figure 3.9: Photograph of the telescope equipped with a 69 μm BaBar IV detector and a thick Si(Li) detector. The electronics is mounted behind the last detection layer.

The electronics feed-through have been realized by seven 50 pin Sub-D vacuum connectors [39] which are integrated into the flange. They allow the connection of one front-end board to one Sub-D connector via a Kapton foil and a special designed vacuum compatible Kapton to Sub-D adapter. A picture of the flange mounted on a holding device is shown in figure 3.9. The seven connectors allow an extension of the telescope by an additional double-sided detector leaving one connector in spare for additional temperature monitoring of the electronics and detectors.

Outside the vacuum the interface boards which are also equipped with Sub-D connectors are simply plugged to the flange. A box made of copper sheet metal is placed around the interface boards to shield them.

Figure 3.10 shows a sketch of the detector positions for a telescope equipped with three detectors in side and top-view. In the axis along the beam (z) the telescope is shifted by 12.5 mm with respect to the nominal target point which is indicated by a filled circle. The configuration shown in the drawing has been optimized for the measurement of the reaction $pd \rightarrow d\omega p_{sp}$ [40]. Here the forward hemisphere of the acceptance is used to detect pd-elastic events for luminosity determination and the backward hemisphere for the detection of the slow spectator proton. By shifting the whole setup backwards, the acceptance for the spectator protons is increased leaving still some coverage of the forward hemisphere. The overall coverage in the horizontal
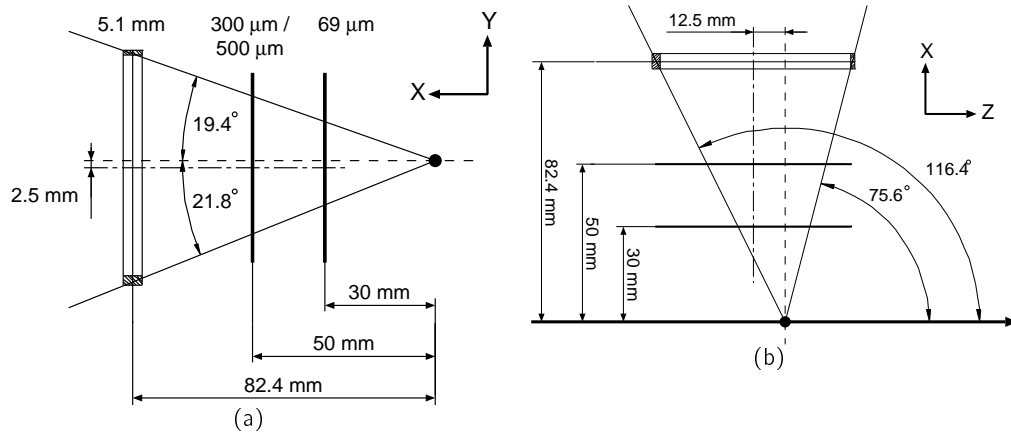
Figure 3.10: Sketch of the detector positions for a telescope equipped with three detectors in side (a) and top (b) view.

angle is thus in a range from 75.6° to 116.4°. Although in the design of the telescope it has been foreseen to position the detectors symmetric around the middle plane, a shift of 2.5 mm to negative *y* values has been measured and is visible in the side view of the drawing. The reason for this is a bending of the mounting pole due to the weight of the detectors, frames and the electronics. The range in vertical angles covered by the telescope is then between −21.8° and 19.4°.

As already mentioned before, all data presented in this work have been taken with a telescope with just two detectors. In the used configuration, the thick detector has been installed at its nominal distance of 82.4 mm to the beam, while the first layer (69 μm) has been moved to the position of the second layer at 50 mm.

With a telescope in full configuration with three detectors, the first two thin layers are mainly used for the tracking of particles, while the last layer with its large strip pitch is used to validate the track and measure the energy of the particle. When only using one thin and the thick Si(Li) detector, the position information from the thick detector is directly used in the track determination. Even though the segments of the thick detector are 666 μm wide, the number of segments that collect charge increases with the total energy deposit and is in the order of 5 segments for the highest energy deposits. As it will be shown in chapter 6, the position of the particle passage is then calculated as the energy weighted center of gravity over the segments collecting the charge. It is however possible that particles exit the detector to the side of the thick detector which essentially cuts off parts of the distribution of collected charge over the segments leading to a shift in the calculated position. To overcome this problem, the segments located at the edge of the detector have not been considered in the analysis. The regions which have been neglected in the analysis are indicated by the shaded areas in figure 3.10.

3.5   Telescope Trigger

In standard configuration with three detectors, the trigger signal from the telescope is the coincidence of the individual signals from the two sides of the intermediate $300\,\mu$m or $500\,\mu$m detector. The detection threshold is thus the energy loss in the first layer plus the trigger threshold of the second layer, since the particle has to pass the first layer before it can even generate a trigger signal. For protons the detection threshold is then about $2.5\,\text{MeV} + 0.15\,\text{MeV} = 2.65\,\text{MeV}$, for deuterons it is in the order of $4\,\text{MeV} + 0.15\,\text{MeV} = 4.15\,\text{MeV}$.

Without the intermediate layer, the telescope trigger is the coincidence of the trigger signals from both sides of the $69\,\mu$m detector. With a trigger threshold of about $150\,\text{keV}$ and the fact that only particles which pass the first detector and deposit enough energy in the second layer can be considered in the track determination, it is apparent that the used trigger is not very efficient. The reason for this is the fact that particles that are stopped in the first detector generate a trigger signal even though those events can not be used in the analysis. However, the used trigger scheme is the only possible scheme in this configuration since the timing of the trigger signals from the thick detector strongly depends on the deposited energy, which essentially disables the use of these signals in a telescope coincidence and especially in a coincidence with other ANKE detection systems. A detailed discussion of the used trigger scheme follows in chapter 4.

Chapter 4

Data Acquisition

For one fully equipped telescope the number of read-out channels is already 750. A dedicated read-out system based on commercially available VME modules that also fits into the ANKE DAQ [41, 42, 43] had to be developed. In order to meet the requirement of an energy determination with a precision of better than 1 %, special modes of operation have also been implemented. They allow the monitoring of the pedestal as well as an individual calibration of each channel. Moreover, the used front-end electronics made it necessary to develop a special trigger and dead-time logic.

In addition a client side software framework has been developed for the DAQ system that provides an easy to use interface to all the configuration parameters of the front-end boards and the VA32TA2 chips. It also allows one to switch the DAQ into different operation modes and run automatic diagnostics routines, which is essential when operating a detection system with that amount of channels.

4.1 Readout Electronics

The read-out system is basically made up of a VME crate holding the digitalization units and a PC running netBSD. The used interface between the VME bus and the PC is a SIS3100 VME to PCI interface [44, 45] with a one unit wide VME controller and a single PCI card. The connection between the controller and the PCI card is accomplished via an optical link. The key feature of the VME controller is an on-board digital signal processor (DSP) which allows the read-out of the VME units into an internal buffer without any traffic over the optical link. The advantage of this controller based read-out is that the modules can be read out with their maximum speed without the necessity of VME calls from the PC. Once each module has been read out and the buffer is filled a fast DMA transfer is initialized to copy the data in the buffer of the controller to the PC memory. When the buffer in the netBSD PC [46] is full, the buffered events are transfered via fast Ethernet to a so called Event-builder that manages the incoming event packages from all the ANKE read-out systems and distributes the data to the permanent data storage and online analysis workstations.

A read-out cycle is initiated by a trigger signal on one of the four inputs of a PCI
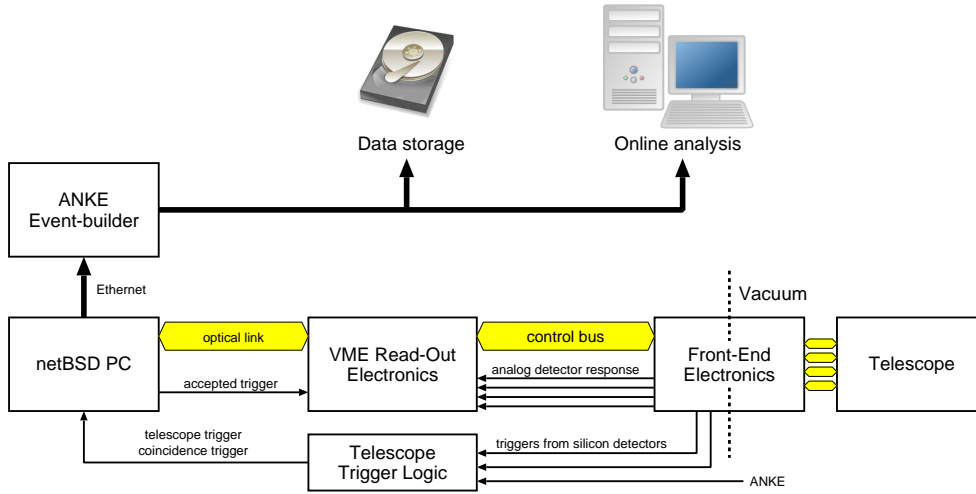
Figure 4.1: Simplified scheme of the telescope data acquisition system. The front-end elec-
tronics is connected to a VME control unit via a flat cable bus. The analog signals
are digitized by VME ADCs. A detailed connection scheme of the VME part of
the DAQ system is given in figure 4.2. The telescope trigger logic is described in
section 4.5.

synchronization unit [47] which is also placed inside the PC. Once an incoming trigger
is accepted by the synchronization unit it switches into a busy state and generates a
signal on an output connector which is used to start the read-out sequence. When
the read-out is completed, the synchronization unit leaves the busy state and accepts
further incoming triggers. A scheme of the tracking telescope read-out system is shown
in 4.1. The block-scheme of the VME part of the DAQ system is displayed in figure 4.2
with a detailed description following in the next sections.

4.1.1 Control

The key component of the read-out system for the tracking telescope is a 16 channel
programmable clock pattern generator. This VME sequencer, a VPG517 [48] produced
by Kramert GmbH, is used to generate all digital control signals for the read-out
sequence as well as the slow control setup of the chips and the interface boards. The
maximum clock frequency is 25 MHz and can be programmed to be either from an
external source or from the VME bus clock with the option of a dividing factor. Its 16
outputs are available on a flat cable connector on the front panel with the first four
channels being also available on LEMO connectors. Besides allowing a read-out with
the maximum possible frequency of 5 MHz[1], the high maximum clock frequency of the
sequencer gives the opportunity to shift control signals relative to each other in steps

---

[1]Although the chips allow 10 MHz as the maximum read-out frequency, the ADC with 5 MHz
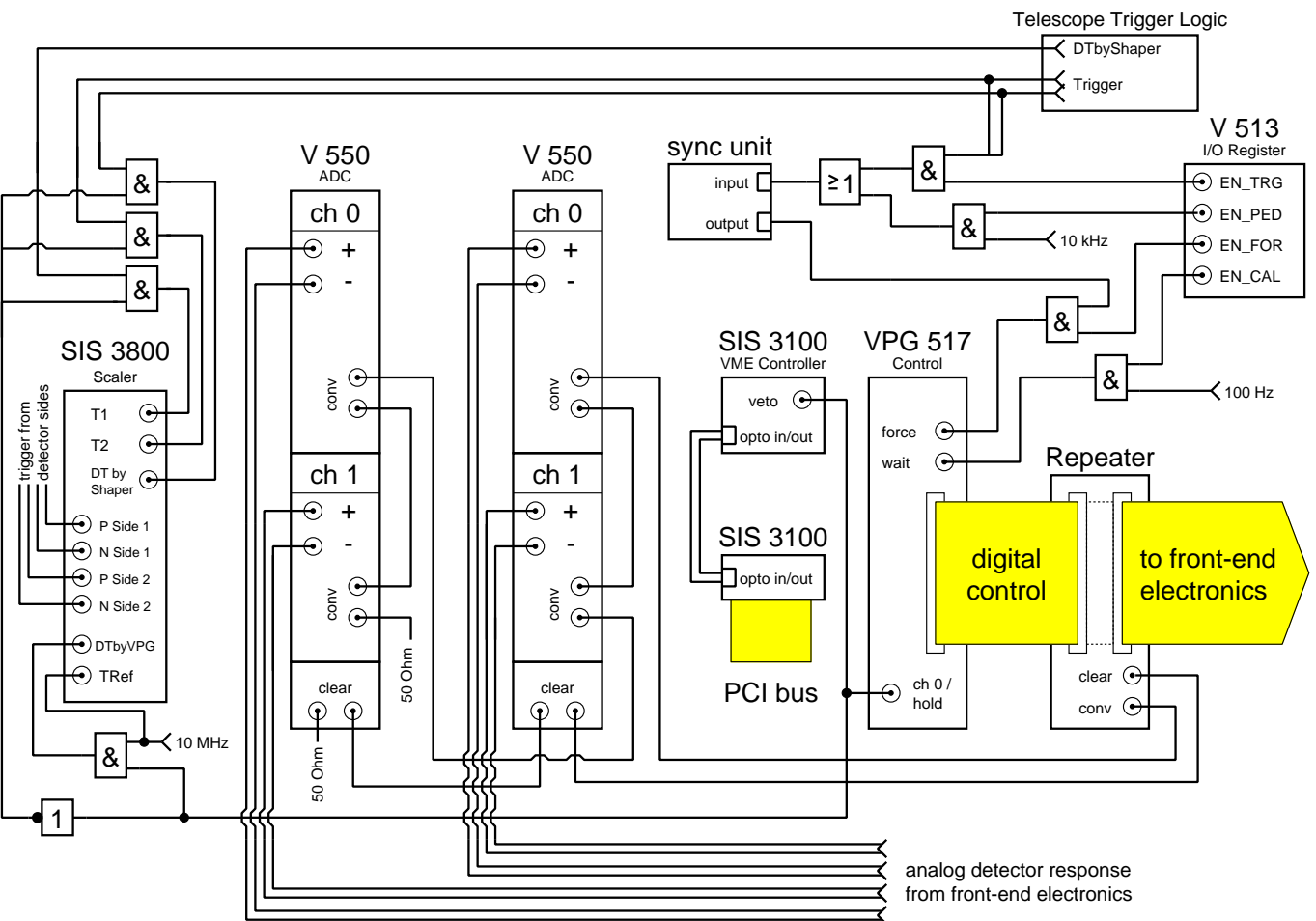maximum conversion frequency is the limiting factor.

Figure 4.2: Connection scheme of the VME part of the Read-Out system. A description of the telescope trigger logic follows in section 4.5 with a connection scheme shown in figure 4.4.

#	Name	Description	Time line
0	VETO	a copy of the "HOLD" signal (taken from front panel LEMO connector)	D
1	A3	address lines for slow control setup	
2	A2	of the chips and the bias voltage DACs	
3	A1		
4	A0		
5	SHIFT_IN_TA	shift in signal for the slow control shift register	
6	CLK_TA	clock signal for the slow control shift register	
7	TEST_ON	switches the front-end chips into test mode and selects the DACs on the interface board for slow control set up.	
8	CLEAR	clears the ADCs	
9	TEST_PULSE	sends a test charge to the front-end chips	
10	SHIFT_IN	shift in signal for the read-out shift register	E
11	CLK	clock signal for the read-out shift register	F
12	DRESET	reset signal for the front-end chips	
13	CONV	conversion signal for the ADC	
14	HOLD	signal to freeze the current VA amplitudes	D

Table 4.1: Summary of digital control signal provided by the VME control unit.

of 40 ns. Smaller steps have to be accomplished by additional cable delays. Table 4.1 describes the digital control signals.

4.1.2 ADC

The differential analog signals from the chips are digitized by CAEN V550 [49] C-RAMS modules. The V550 is a single slot wide VME ADC module that has been specially designed for the read-out of multiplexed analog signals. Each module houses two separate 10 bit ADC channels which are multiplexed to allow the digitalization of up to 2016 segments per input. A pedestal and threshold memory is provided for every channel, which gives the possibility to have a zero suppression done by the module. Both the pedestal and threshold values can be set with an accuracy of 12 bit[2]. The maximum conversion rate is 5 MHz which corresponds to a conversion time of 200 ns. The digitized analog value, if above threshold, is together with the strip number and status information stored in a 32 bit wide and 2047 word deep FIFO that can be accessed via the VME-Bus. Although only two ADC units are displayed in the connection scheme in

---

[2]The reason for the 12 bit pedestal and threshold memory is the fact that the 10 bit V550 ADC is upgradeable to a 12 bit version.

figure 4.2 the DAQ system is designed to be easily extendible by a user-defined number of ADC units.

4.1.3   Scaler

For count rate monitoring and an off-line dead-time correction a 32 channel SIS3800 VME scaler unit [50] has also been integrated into the read-out system. Table 4.2 gives an overview of the counted signals. Due to the fact that the trigger part of the VA32TA2 front-end chips generated random triggers during the period of clocking (time lines F, H and I in figure 3.7) the scaling for the "DTbyShaper" and telescope trigger signals needs to be blocked during that time by the "VETO" signal. The active time of the "VETO" signal is however measured (DTbyVPG) and allows together with the reference clock (TRef) an extrapolation of the measured "DTbyShaper" and trigger counts to the real numbers. The actual counts for the trigger and "DTbyShaper" are essential for a dead-time correction which is described in detail in section 4.6.

Name	Description	Time line
DTbyShaper	10 MHz reference clock representing the dead time introduced by trigger signal shaping (counting blocked by VETO signal)	C
T1 ...	trigger signals from telescope trigger logic (counting blocked by VETO signal)	
DTbyVPG	10 MHz reference clock (counting enabled by VETO signal)	L
TRef	10 MHz reference clock	K

Table 4.2: Overview of the signals counted by the dedicated VME scaler unit.

4.1.4   I/O Register

One drawback of the used sequencer is the fact, that only one programmed sequence can run at a time. This means that the DAQ has to be stopped in a defined state in order to perform the slow control setup and vice versa. To ensure stable operation a CAEN V513 VME digital I/O unit [51] has been introduce to the DAQ system. The unit allows to block certain signals and therefore to switch the read-out system into different modes of operation. Table 4.3 describes how the output channels are used.

4.2   DAQ modes

To ensure the performance of the silicon tracking telescope and for commissioning and maintenance purposes the developed DAQ system may be switched into different

Bit	Name	Description
0	EN_TRG	enables the trigger signal to reach the synchronization unit
1	EN_FOR	enables the accepted trigger signal to reach the "FORCE" input of the control unit
2	EN_PED	switches a 10 kHz signal to the input of the synchronization unit
3	EN_CAL	switches a 100 Hz signal to the "WAIT" input of the control unit

Table 4.3: Description of the I/O register bits used to control the DAQ operation mode.

Operation Mode	EN_TRG	EN_FOR	EN_PED	EN_CAL
Data taking	1	1	0	0
Pedestal	0	1	1	0
Calibration	1	1	0	1
Slow control	0	0	0	0

Table 4.4: Summary of the I/O register bit pattern setting for the different DAQ operation modes.

modes of operation. This is achieved via the VME I/O register described in the previous section. Table 4.4 summarizes the implemented modes. It is obvious that the "data taking" mode is the most important one. However in chapter 5, that is concerned with energy measurement, it will be shown how important the calibration and the monitoring of the pedestals is for a precise energy determination and thus the performance of the detection system.

4.2.1 Data taking mode

A physical trigger is either accepted or rejected by the synchronization unit (time line A in figure 3.7). The accepted trigger (B) is available on the output of the synchronization unit and connected to the "FORCE" input of the VPG517. It is used to start the programmed read-out sequence in the VPG517 control module. The running sequence generates all the necessary control signals for the read-out of the front-end chips (D, E and F) as well as the conversion signal for the ADC ("CONV"). It is available on a LEMO connector on the front panel of the repeater board. A copy of the hold signal is taken from the front panel of the VPG517 and is used to delay the read-out of the VME digitalization modules by the DSP in the VME controller. At the end of the read-out cycle, when the hold signal and its copy become inactive and all modules have been filled, the VME controller triggers the DSP read-out of the modules. On acceptance of the trigger the synchronization unit has already triggered a software routine via an interrupt. Once the data is processed by the software the synchronization unit leaves its busy state and accepts new incoming trigger signals.

4.2.2   Pedestal mode

Especially when running with zero suppression in the ADCs it is essential to monitor the behavior of the pedestals. For this purpose the "pedestal" mode has been implemented into the DAQ system. In pedestal mode a 10 kHz generator signal is fed to the input of the synchronization unit. The incoming physical triggers are blocked from the trigger input in order not to distort the pedestal measurement. Besides the rare case, when the constant frequency trigger occurs in coincidence with a physical trigger, the measured data for a strip corresponds to the pedestal of this channel since no energy has been deposited in that strip by a particle passing through the detector.

4.2.3   Calibration mode

A correct energy calibration of the setup requires that the calibration has been performed under the same experimental conditions as the data taking with the telescope. In "calibration" mode a second sequence is stored in the VPG517 in parallel to the regular read-out sequence. A 100 Hz generator signal is fed to the "WAIT" input of the VPG517. When the signal arrives, the second sequence is triggered which generates a test pulse. At the end of the sequence the control unit sleeps in an endless loop and waits for a trigger from the front-end chips. The signal path for the trigger is the same as for regular data taking which ensures similar experimental conditions when running in calibration mode. Typical calibration spectra are shown in chapter 5.

4.3   Integration into the ANKE DAQ

Each of the ANKE detection systems is equipped with a synchronization unit that is interconnected via a ring bus. One of the synchronization units on the bus is the master which receives the triggers, all other units are configured as slaves. A trigger, accepted by the master, is passed to the slaves on over the ring bus and starts the read-out sequence in each slave. When all slave systems have finished the read-out cycle and processed the data, the master synchronization unit is ready to accept new incoming triggers. The read-out system of the tracking telescope is equipped with a master synchronization unit which also allows the use of the setup either in stand alone mode at ANKE or in the lab. In this configuration the synchronization ring bus is basically a closed loop with only one unit. For the integration into ANKE the existing synchronization ring is opened and the tracking telescope synchronization unit, configured as a slave, is connected to the ANKE synchronization ring. In addition the trigger signals connected to the inputs of the tracking telescope synchronization unit in stand alone operation have to be connected to the inputs of the ANKE master synchronization module.
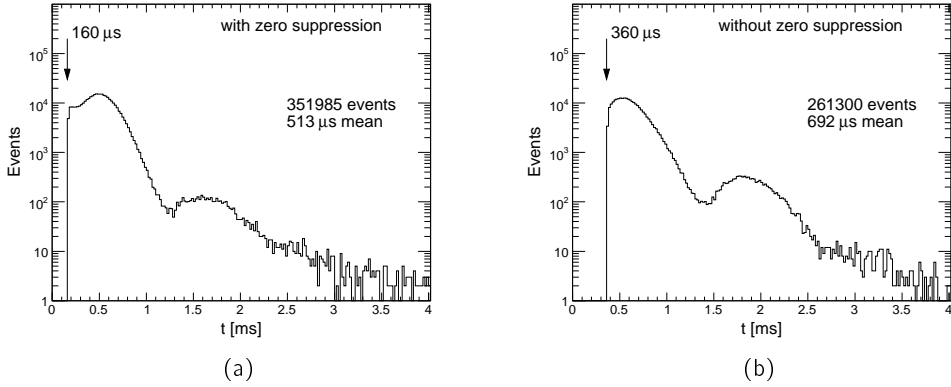
Figure 4.3: Distribution of times between two consecutive events for data taken with (a) and without (b) zero suppression. Both plots represent an equal measurement time of 180 s.

4.4 Readout Performance

With an accepted trigger the read-out procedure for all configured ANKE detection systems is started. For the tracking telescope read-out electronics the time of a full read-out sequence strongly depends on the mode of operation. Figure 4.3 shows the distribution of times between two consecutive events for data taken with (a) and without (b) zero suppression. In both cases the displayed statistics represents a single accelerator spill of 180 s duration. The edges on the left of each plot correspond to the minimum time that is required to process one event. For the data taken with zero suppression the minimum time is 160 μs while it is 360 μs for the none zero suppressed data and fixed. This minimum time can be expressed by

$$t_{\text{readout}} = t_{\text{front-end}} + N_{\text{data}} \cdot t_{\text{transfer}} \tag{4.1}$$

in which $t_{\text{front-end}}$ is the time from the acceptance of the trigger to the start of the data transfer from the VME digitalization modules to the DSP buffer. It includes the delay between the trigger and the hold signal as well as the actual clocking of the front-end chips and was in the order of 140 μs. N_{data} represents the number of data words that have been digitized, without zero suppression it is 471 while with zero suppression it is between 30 and 55. t_{transfer} is the average time for a single data word transfer. Since the DSP issues a block transfer to copy the data from the VME modules to its buffer, t_{transfer} also contains the time to set up such a block transfer. With t_{transfer} being in the order of 450 ns the difference in the minimum time required for the read-out of a single event becomes obvious. Both histograms also show a bump at approximately 550 μs which correspond to the average input trigger rate of roughly 1800 triggers per second. The second bump at 1.8 ms without zero suppression and at 1.6 ms with zero suppression originates from the increased time it takes to process
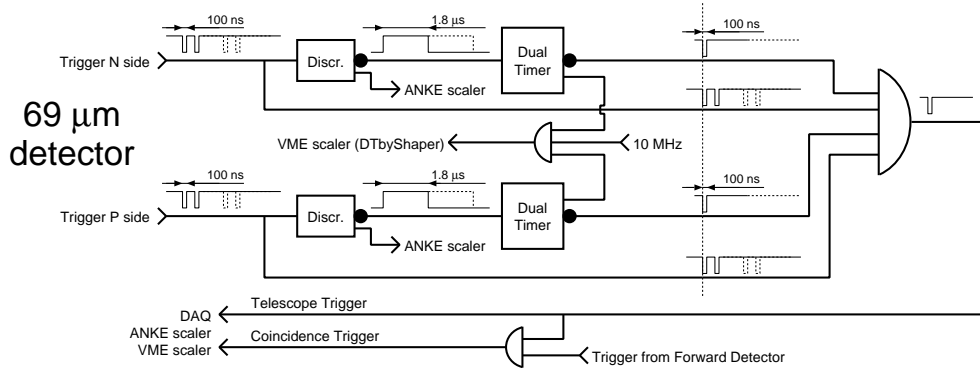
Figure 4.4: Connection scheme of the telescope trigger logic.

the event when the data buffered in the netBSD PC is transfered from the read-out system to the Event-builder via Ethernet.

4.5   Trigger Scheme

The VA32TA2 front-end chips allow the tracking telescope to generate a trigger for the data acquisition. Due to the fact, that the front-end electronics, with the chip settings used during the data taking, produced after pulses for each true trigger (time line B in figure 3.7 on page 20) a dedicated trigger and coincidence scheme had to be set up. Figure 4.4 shows the trigger scheme for the tracking telescope using the individual triggers from both sides of the first (69 μm) detector. In order to remove the secondary pulses the trigger signal is fed to a discriminator which produces a single pulse with a fixed width of 1.8 μs. In case of an after-pulse within this 1.8 μs window the output pulse of the discriminator is prolongated by another 1.8 μs with respect to the second incoming double pulse. The secondary triggers and the prolongation of the pulse are indicated by dotted lines in the figure. In a second stage the leading edge of the inverted signal from the discriminator is used by a dual timer unit to generate a single pulse. The falling edge of the discriminator signal clears the dual timer and enables it to generate new pulses. This means that new output pulses are only generated after at least 1.8 μs. The shaped and original trigger signals from both sides of the detector are used by a four-fold coincidence unit to generate the final telescope trigger. It may be used directly or in coincidence with the trigger from another ANKE detection system (i.e. the ANKE forward detector [52, 53]) to start the data acquisition. For monitoring purposes the signals generated by the discriminators as well as the final triggers are counted by the ANKE system scalers. To measure the trigger dead-time introduced by the discriminators a dedicated scaler unit has been implemented in the telescope read-out system. The so called "DTbyShaper" (dead-time by shaper) signal is the coincidence of both discriminator outputs and a 10 MHz reference clock which allows the determination of the introduced dead-time with a resolution of 100 ns (time line C).

4.6   Dead-Time correction

As shown in the previous sections the data acquisition takes between $160\,\mu s$ and $360\,\mu s$ to digitize and process a single event. Any trigger arriving during that time is lost but counted in the ANKE system scalers. For any physics analysis it is essential to correct the observed counts and rates for this dead-time via the following equation

$$N_{\mathrm{real}} = N_{\mathrm{measured}} \cdot \frac{t_{\mathrm{m}}}{t_{\mathrm{m}} - N_{\mathrm{measured}} \cdot \tau} \qquad (4.2)$$

in which N_{measured} is the measured trigger rate or counts for a certain reaction channel, N_{real} is the real rate or real number of counts, τ is the dead-time and t_{m} is the measurement time. In a simple dead-time correction one would use the number of accepted triggers and the total number of incoming trigger for a certain trigger type and calculate the dead-time as

$$\tau = t_{\mathrm{m}} \cdot \frac{N_{\mathrm{real}} - N_{\mathrm{acc}}}{N_{\mathrm{real}} \cdot N_{\mathrm{acc}}} \qquad (4.3)$$

where N_{acc} is the number of accepted triggers and N_{real} is the number of triggers counted by the ANKE system scalers. Due to the random triggers generated by the telescope front-end chips during the read-out sequence the number of incoming triggers for a trigger involving the tracking telescope trigger is contaminated and essentially higher than the real number. With the information counted by the dedicated VME scaler it is possible to extrapolate to the real number of incoming triggers via the following equation

$$N_{\mathrm{real}} = N_{\mathrm{VME}} \cdot \frac{t_{\mathrm{m}}}{t_{\mathrm{m}} - (t_{\mathrm{DTbyVPG}} + t_{\mathrm{DTbyShaper}})} \qquad (4.4)$$

In equation 4.4 N_{VME} is the number of triggers counted by the VME scaler, t_{m} is the time of the measurement and t_{DTbyVPG} is the time during which the counting by the VME scaler is blocked whereas $t_{\mathrm{DTbyShaper}}$ is the time the telescope trigger scheme is blocked and trigger generation is disabled. Figure 4.5 shows the typical distribution of $t_{\mathrm{DTbyShaper}}$. Each trigger arriving at the discriminator opens a $1.8\,\mu s$ long time window during which the $10\,\mathrm{MHz}$ reference clock is scaled. In addition, the counting is also blocked during the read-out sequence while t_{DTbyVPG} is only measured during the read-out sequence. Hence $t_{\mathrm{DTbyShaper}}$ and t_{DTbyVPG} do not overlap and may be simply added to form the full dead-time introduced by the trigger logic. The peaks in the histogram at multiples of $1.8\,\mu s$ correspond to the number of windows between two consecutive events. The tails to larger values are due to the possible prolongation of the window by a second incoming trigger. With each accepted trigger also a $1.8\,\mu s$ window is opened. The peak on the far left of the histogram represents the delay between the accepted trigger and the actual start of the read-out sequence when no additional windows have been opened since the previous accepted event. By analyzing the $t_{\mathrm{DTbyShaper}}$ distribution it is possible to extract the number of windows between two events. This is especially important for the dead-time correction of a trigger that is the coincidence
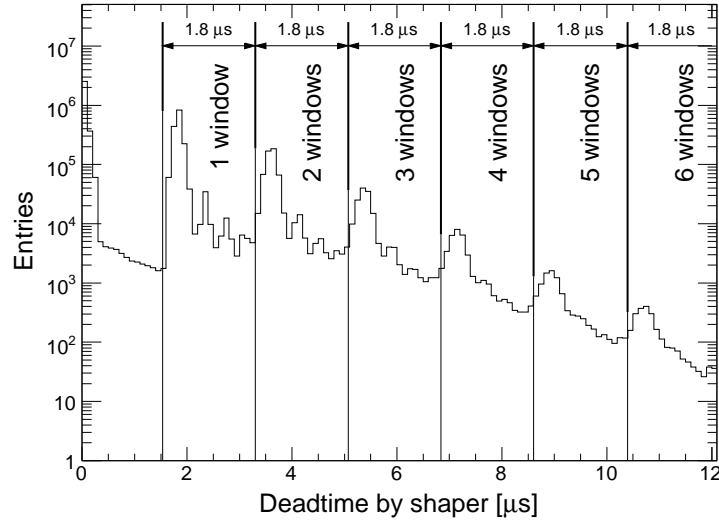
Figure 4.5: Distribution of the dead time introduced to the telescope trigger by the shaping of the trigger signals from the individual detector sides ("DTbyShaper"). Each peak corresponds to a $1.8\,\mu s$ wide time window that is started by the incoming trigger from the VATA chips. The tails to higher times originate from the possible prolongation of the window. Analyzing the value for "DTbyShaper" on an event by event basis allows to extract the number of windows and hence the number of coincidence opportunities between two events.

of the telescope trigger and the trigger of another ANKE detection system. In case of the forward-telescope coincidence trigger, a $400\,ns$ wide coincidence window is opened with each start of a "DTbyShaper" window. This means that the trigger scheme is not blocked for the full $1.8\,\mu s$ plus prolongation for each "DTbyShaper" window but only for $1.4\,\mu s$ plus prolongation. Applying this modification to equation 4.4 results in an equation for the real number of incoming coincidence triggers (equation 4.5).

$$N_{\text{real}} = N_{\text{VME}} \cdot \frac{t_{\text{m}}}{t_{\text{m}} - (t_{\text{DTbyVPG}} + t_{\text{DTbyShaper}} - N_{\text{w}} \cdot 400\,\text{ns})} \qquad (4.5)$$

$$\tau = \frac{N_{\text{VME}} \cdot t_{\text{m}} - N_{\text{acc}} \cdot \{t_{\text{m}} - (t_{\text{DTbyVPG}} + t_{\text{DTbyShaper}}[-N_w \cdot 400\,\text{ns}])\}}{N_{\text{VME}} \cdot N_{\text{acc}}} \qquad (4.6)$$

Combining equations 4.3 and 4.5 yields an equation (4.6) for the dead-time of the read-out system for a trigger that involves the telescope trigger. In equations 4.5 and 4.6 N_w represents the number of "DTbyShaper" windows. The modification for the coincidence trigger is indicated in squared brackets in equation 4.6.

Unfortunately only after the period of data taking a discrepancy between the number of incoming triggers counted by the ANKE system scalers and the VME scaler had been discovered. In the data the number measured by the ANKE scalers is about
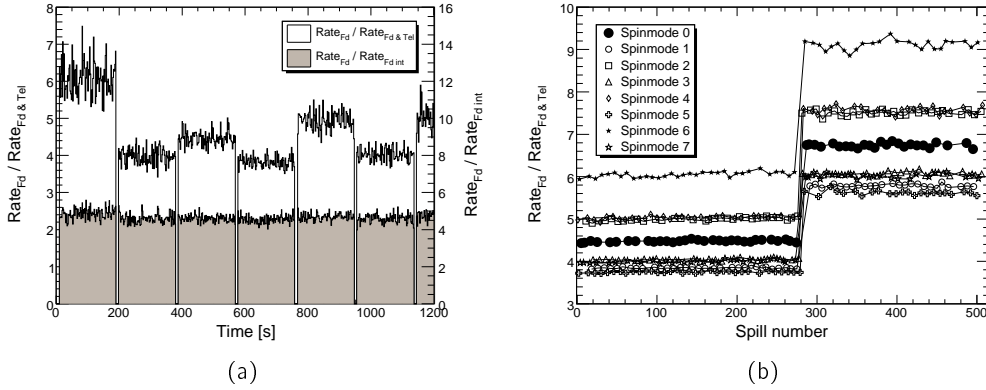
Figure 4.6: (a) ratios of the prescaled trigger rate of the forward detection system (Rate_{Fd}) to the forward - telescope coincidence trigger rate ($\text{Rate}_{Fd\,\&\,Tel}$) as a function of time for six consecutive accelerator spills. As a reference the shaded histogram shows the ratio of the prescaled forward trigger to the forward trigger with an additional cut on the energy loss in the forward hodoscope ($\text{Rate}_{Fd\,int}$). (b) development of the average ratio of the prescaled forward trigger to the coincidence trigger for each beam spin-mode.

5 % less than the number given by the VME scaler. However, due to the fact that the ANKE scaler counts the contaminated trigger signal, the number obtained by the ANKE scaler must be larger than the number measured by the VME scaler. From the available data it was not possible to specify the reason for this discrepancy which might have been double pulses in the VME scaler channel or missed pulses in the ANKE scaler channel.

Although the available data did not allow the determination of absolute values for the dead-time, it was possible to perform a relative dead-time from accelerator spill to accelerator spill. Figure 4.6(a) shows the time flow of the ratio of the prescaled trigger rate of the forward detection system (rate_{Fd}) to the rate of the forward - telescope coincidence trigger ($\text{rate}_{Fd\,\&\,Tel}$) for six consecutive complete accelerator spills. The shaded histogram shows the ratio of rates for the prescaled forward trigger to the forward trigger with an additional cut on the energy loss in the forward scintillation hodoscope ($\text{rate}_{Fd\,int}$) as a reference. The average fluctuation within one spill is in the order of 14 % for the ratio involving the telescope trigger and 11 % for the reference plot which does not include the telescope trigger. The rather larger jumps in the ratio rate_{Fd} to $\text{rate}_{Fd\,\&\,Tel}$ from spill to spill are caused by the different beam polarization modes for two consecutive spills. Figure 4.6(b) displays the average ratio of the prescaled forward trigger rate to the coincidence rate for each of the available beam spin modes for the complete data set. For each of the spin-modes the ratio is constant over the time of data taking. The jump at approximately spill 280 is caused by a change in the prescaling factor for the forward trigger from 10 to 15. The jump in the graphs reflect this change in the prescaling factor. Both the fact that the ratio of rate_{Fd} to

rate$_{\text{Fd \& Tel}}$ is constant over the duration of a spill and that the average of this ratio over one spill is constant over the full data set allows to perform a relative dead-time correction from spill to spill even if N_{VME} and the extrapolated number of incoming triggers are not absolutely correct numbers. This is of special importance for the polarimetry investigations in which one is only interested in relative counts for the different beam polarization states. Details on the polarization measurements are given in chapter 7.

Chapter 5

Energy Measurement

The main field of application of the Silicon Tracking Telescope is to identify and measure the energy of low energy spectator protons with a precision better than 1 %. Knowing the four-momentum of this spectator proton it is possible to identify a proton-neutron reaction and to also determine the four-momentum of the neutron in the initial state on an event by event basis.

Special attention has to be drawn to the configuration parameters of the front-end electronics and the read-out system in order to achieve the desired precision. In addition, the calibration coefficients that map the ADC value to an energy loss information have to be determined for each individual read-out channel.

Moreover, changes in the working environment, such as the temperature and the low voltage power supply of the chips, result in an effect called common-mode, which is a common shift of the base-line of the front-end electronics that can be corrected in an off-line analysis. Without correction the shift would essentially lead to a false measurement of the energy loss.

5.1   Tuning

The tuning of the read-out system for best performance can be logically split into two independent parts. First the correct chip bias voltage and control register settings have to be found for the different front-end - detector combinations. In a later stage, the DAQ has to be tuned which basically means optimizing the timings of the digital control signals.

5.1.1   Chip tuning

In section 3.2 it was demonstrated that the used front-end chip with its eight bias voltages and the different possible control register settings is on one side very flexible but also rather complicated to setup for best performance. By switching the front-end chips into test mode and shifting one bit in both the test and read-out shift registers to one of the channels, this channel becomes transparent. This means that
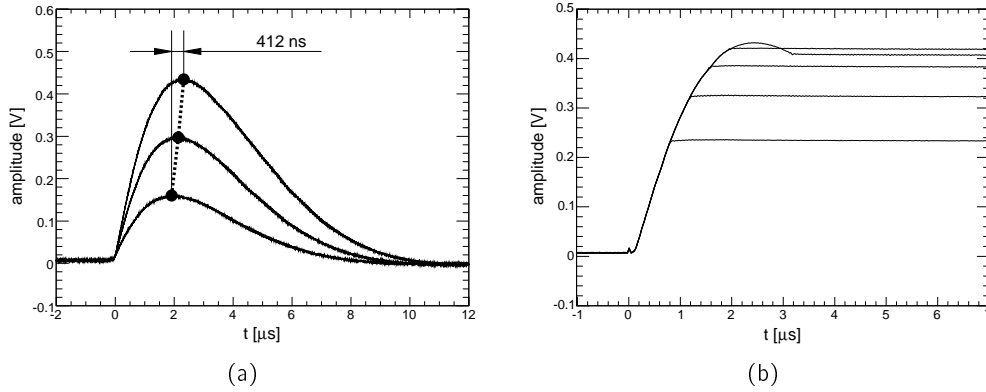
Figure 5.1: (a) Pulse shape for test pulse amplitudes of 500 fC, 1000 fC and 1500 fC. (b) Pulse shape for a test charge of 1500 fC with the "hold" signal applied at 0.8 μs, 1.2 μs, 1.6 μs, 2.0 μs and 3.2 μs after injecting the test charge.

a charge applied to the input of the selected channel is amplified by the slow shaper of that channel and directly available on the output of the chip. After sending a test pulse to this selected channel the pulse shape can be observed with an oscilloscope or sampled by an ADC. Figure 5.1(a) shows the pulse shape for several different test pulse amplitudes. The variation in peaking times (the time until the pulse has reached its peak amplitude) is of the order of 400 ns.

In an ideal case the peaking time should not depend on the amplitude of the test pulse. By setting the bias voltage of the front-end chips appropriately it is possible to minimize this dependence. However, connecting a different detector to the front-end board or connecting the other side of a detector may change the optimum bias voltage settings. Therefore the tuning of the chip parameters has to be repeated after such changes.

5.1.2   Read-Out tuning

The tuning of the read-out system is mainly finding the correct timing for all the digital control signals. The timing of the hold signal is one of the most important ones, since it determines how well the peak amplitude of a signal is sampled by the ADC. Figure 5.1(b) shows the pulse shape for a fixed test pulse amplitude and a variety of different hold delays. Goal of the tuning is to find the hold delay in such a way that the hold signal is applied to the sample and hold facility of the chip when the analog signal in the slow shaper has reached its maximum. Since the hold delay is fixed by the sequence running in the control unit it becomes obvious, how important a minimum peaking time variation and therefore the chip tuning is for a good performance of the energy measurement. In practice, the hold delay is adjusted by triggering the DAQ with test-pulses of the most probable expected amplitude and varying the hold delay with
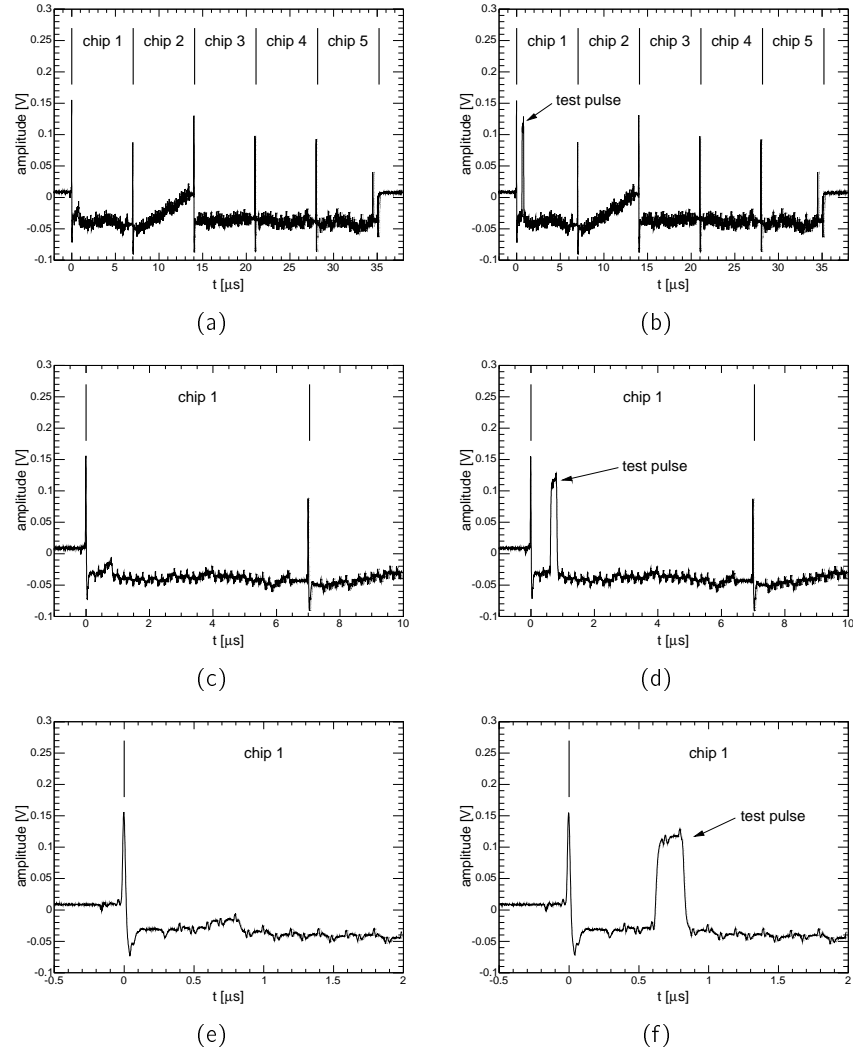
Figure 5.2: Output amplitude distribution of a front-end board with 5 chips. The plots in the right column (b, d and f) show a sequence with a test pulse injected into the third channel of the first chip in the chain. Sub-figures c and d show a zoom onto the first chip and e and f display a zoom onto the region in which the test pulse was been applied.

respect to the incoming trigger until a maximum chip response is reached. Since the determined hold delay depends on the trigger delay, the time between the generation of trigger in the front-end and the actual start of the DAQ, it is obvious that special care has to be taken in order to have equal trigger delays during tuning and data taking.

The second delay that has to be tuned in the read-out system is the delay between the clock and the conversion signal. Consecutive pulses to the "clk" input of the front-end chips switch the output of the slow shaper to the output multiplexer. There has to be a corresponding conversion signal to each "clk" pulse in order to sample the multiplexed data synchronously. A rough estimate for the delay between both signals is the time the "clk" travels from the read-out control unit generating the signals to the front-end chips plus the time the analog signal travels back to the ADC. Figure 5.2 shows the distribution of the output signals of a front-end board with five chips. In Figures 5.2(a) and (b) all five chips are visible, (c) and (d) show a zoom onto the first chip and (e) and (f) display the first 8 channels of the first chip. In the plots on the right side (a,c and e) also a test pulse has been introduced to the third channel of the first chip. With a clock frequency of 5 MHz each channel is only for 200 ns available at the input of the ADC. In addition to that, the settling time of the analog signal has to be taken into account. From 5.2(f) it is obvious that the full amplitude of the analog signal is only available at the very end of the 200 ns active time of each channel. For best performance the conversion pulse has to be shifted to the end of this active cycle. A trivial check, whether the delay of the "conv" to the "clk" signal is set correctly, is to look at the channel adjacent to a channel with a high amplitude test pulse because the settling time does not only apply to a rising signal but also to a falling one. If the timing is set correctly the amplitude in the adjacent channel must correspond to the pedestal of that channel. In case the "conv" signal is applied too early, a channel adjacent to a channel with a test pulse will show some remaining amplitude of the test pulse.

5.2   Calibration

Once the front-end electronics and the read-out system are tuned for a certain experimental setup, a calibration that maps the chip response in ADC channels to an energy loss of a particle passing through the detector needs to be obtained. In practice, the calibration procedure is split into three stages. In the first stage, the test-pulse capabilities of the VA32TA2 chips is exploited to determine the response function of the chips. In later steps real data is used to obtain an absolute energy calibration.

5.2.1   Test Pulse measurements

The VA chips test pulse capabilities allow one to calibrate each VA channel individually. The test charge is generated by a voltage step over a test capacitance of 1 pF on the front-end electronics board which is generated by one of the digital control signals. The amplitude of the voltage step is determined by one channel of the DAC integrated on

(a)   (b)
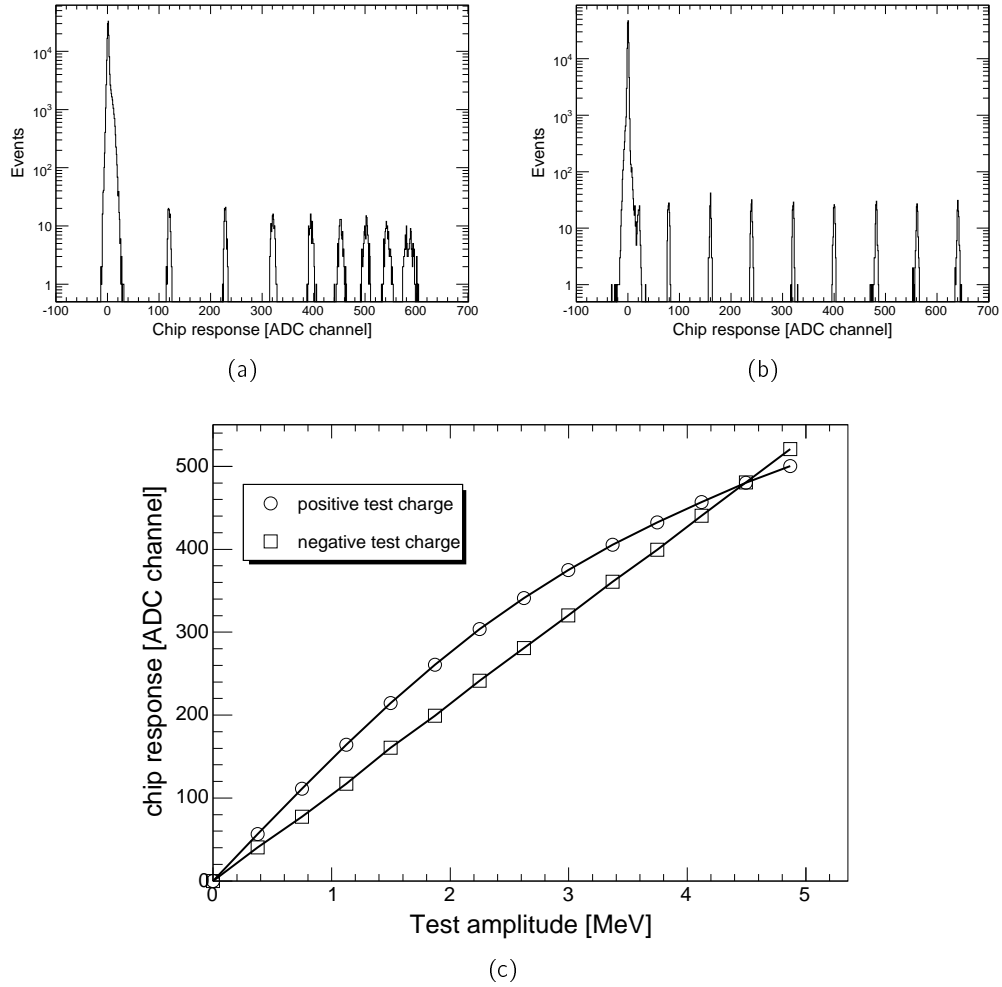

(c)

Figure 5.3: Typical test pulse histograms for positive (a) and negative (b) test charges. Sub-figure c shows the chip response as a function of the applied test charge for both positive and negative test charges.
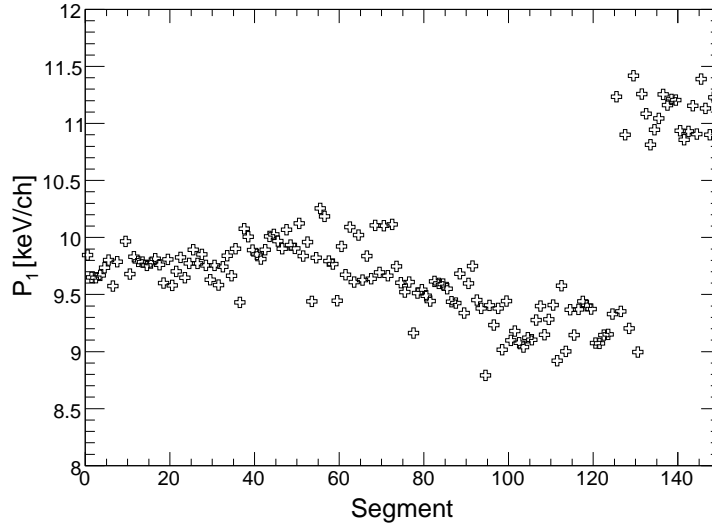
Figure 5.4: Distribution of the calibration coefficient P_1 over one side.

the interface board with an addition dividing factor of three. The applied test charge is then given by

$$Q_{\text{test}} = \frac{1}{3} 1 \, \text{pF} \cdot U_{\text{test}} \tag{5.1}$$

With the knowledge, that an energy deposit of 3.6 eV creates one electron-hole pair [54], the energy equivalent E_{test} to the applied test charge can be expressed by

$$E_{\text{test}} = 1 \cdot 10^{-15} \cdot \frac{3.6 \, \text{eV}}{1.602 \cdot 10^{-19} \, \text{fC}} \cdot Q_{\text{test}} = 22.472 \, \frac{\text{keV}}{\text{fC}} \cdot Q_{\text{test}} \tag{5.2}$$

Typical test pulse histograms are shown in figure 5.3. In the histograms the test pulse peaks are 50 fC apart from each other with 100 entries in each peak. The peaks on the far left of the histograms are the pedestals.

By measuring the chip response for several different test charges a preliminary calibration is obtained. Figure 5.3(c) shows the test amplitudes in MeV as a function of the chip response in ADC channels for positive and negative amplitudes. A fit by a 4th degree polynomial to the test pulse plots results in a calibration function for each channel. On the front-end board each of the five chips has its own test capacitance which means that the effective test pulse amplitude may vary from chip to chip due to production tolerance of the capacitance and the placement of the capacity on the printed circuit board. With the existing front-end board chip number 5 always shows lower test pulse amplitudes. The reason for this behavior is a change in the effective capacitance due to the placement of the components on the board. Figure 5.4 shows the distribution of the calibration coefficient P_1 over all strips of
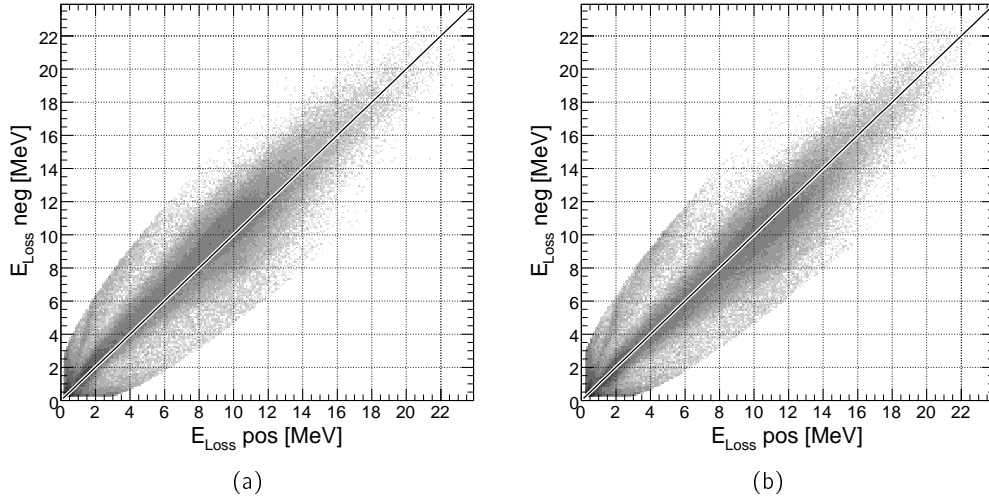
Figure 5.5: Energy loss of the negative side versus the energy loss of the positive side before (a) and after adjusting the calibration (b). Before the adjustment the band is slightly rotated to the axis of the negative side.

the negative side of the first detector. The strips connected to chip 5 (starting from strip 125) show a significant difference to the rest of the strips. To overcome this behavior an additional calibration factor has been introduced which lets one equalize the effective test capacitance. The energy loss information for a segment can thus be calculated with

$$E_{\text{loss}} = Cap \cdot (P_0 + P_1 \cdot ch + P_2 \cdot ch^2 + P_3 \cdot ch^3 + P_4 \cdot ch^4) \qquad (5.3)$$

in which ch is the chip response in ADC channels, P_0 through P_4 are the calibration coefficients and Cap is the capacitance coefficient. By definition P_0 is forced to zero since a chip response of zero must give a energy loss of zero.

5.2.2 Equalizing the Calibration for both sides of a detector

The charge collected from both sides of a detector must be the same. The energy deposit for a hit is given by

$$E_{\text{sum}} = \sum_{\text{segments}} E_{\text{segment}} \qquad (5.4)$$

and

$$E_{\text{hit}} = S_1 \cdot E_{\text{sum}} + S_2 \cdot E_{\text{sum}}^2 + S_3 \cdot E_{\text{sum}}^3 + S_4 \cdot E_{\text{sum}}^4 \qquad (5.5)$$

in which E_{segment} is the energy deposit for a segment which is given by equation 5.3 and E_{sum} is the sum of energy losses over all segments that comprise the hit. S_1
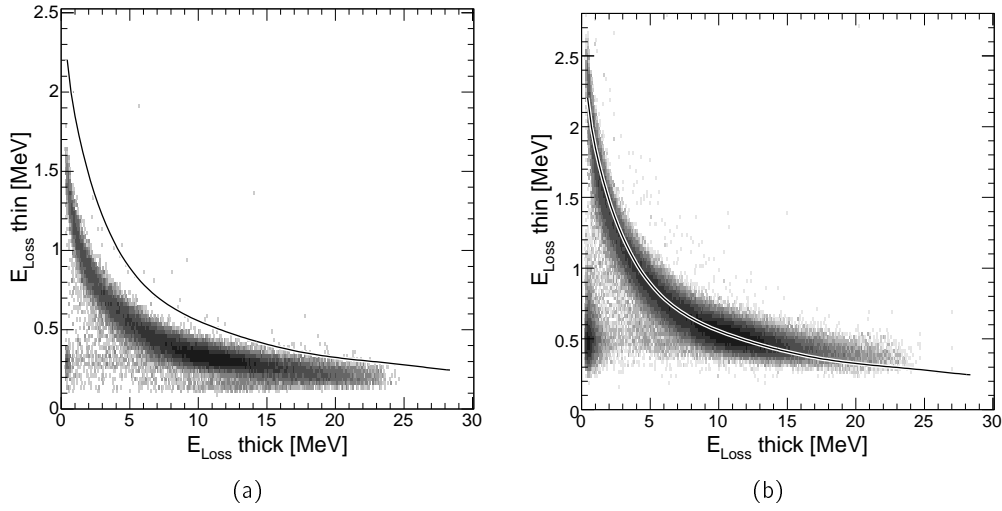
Figure 5.6: Energy loss of a hit in the thin detector versus the energy loss of a hit in the thick detector for the same track for the preliminary (a) and the final energy calibration (b). The black curves indicate the SRIM calculation. Both plots show the integral data for the whole telescope with 128 segments by 151 segments in the first detection layer and 96 segments by 96 segments in the second detector.

through S_4 are additional per side calibration coefficients. The left plot in figure 5.5 shows the energy loss of the negative side versus the energy loss of the positive side of the thick detector. The black line indicates equal energy losses from both sides. In the figure the band is rotated to the y-axis which means that either the negative side gives too high energy losses or the positive side gives too low energy losses. Adjusting S_1 through S_4 for both sides leads to equal energy losses over the full range. The energy loss from the negative side versus the energy loss from the positive side after the adjustment of the coefficients is displayed in the right plot of figure 5.5.

5.2.3   Finalizing the Calibration

With the energy calibration obtained up to this point it is already possible to identify particles by exploiting the ΔE vs. E method. The plot in figure 5.6(a) shows the energy loss of a hit in the thin detector versus the energy loss of a hit in the thick detector for the same track. A band of protons is clearly visible but does not coincide with the expected curve indicated by a solid line. To finalize the calibration it is possible to adjust the coefficients S_1 through S_4 for all four sides by fitting a sample of selected protons to the calculated curve. The result of the fit is shown in figure 5.6(b). With the final calibration the band coincides very well with the calculation.

5.3   Common Mode and its Correction

In an ideal situation a segment that has not collected any charge gives an ADC value that is equal to the channels pedestal value. Depending on the read-out frequency and various other reasons it is possible that the baseline of the read-out electronics shifts from event to event. This results in a common shift of the pedestals for all channels which essentially leads to an offset in the calculation of the energy loss for one segment. The behavior is known as common mode and can be corrected in the off-line analysis.

Figure 5.7(a) shows the event by event jump of the pedestal of one channel of the negative side of the thin detector for 25 consecutive events. Without common mode the data points would be located at zero. The plot shows that the pedestal oscillates in the range of -6 to $+6$ ADC channels around zero. The energy equivalent of this range is approximately $\pm 50\,\mathrm{keV}$. A similar picture for the negative side of the thick detector is displayed in figure 5.7(b). In case of the thick detector the range in which the average pedestal oscillates around zero is from -3 to $+3$ ADC channels or -120 to $+120\,\mathrm{keV}$ in energy equivalent. Taking into account that the charge generated by a particle in the thick detector is in average collected by about five segments the maximum error in energy loss determination introduced by the common mode is $\approx 5 \cdot 120\,\mathrm{keV} = 600\,\mathrm{keV}$.

The following is a description of the two in the analysis software available correction methods as well as a comparison in correction quality and performance of the two methods.

5.3.1   Mean value correction

The "Mean value" correction algorithm calculates the common mode for each event as the mean value of each segments ADC value minus the channels nominal pedestal. In particular, a segment is only used in the calculation of the common mode when its ADC value is below a certain threshold. For the N-side of the thin detector for instance, where the maximum positive swing of the common mode is 6 ADC channels, a value of 7 or 8 ADC channels as a threshold is a good choice. The threshold for the common mode correction must in any case be higher than the maximum positive swing of the common mode. If it is set below the maximum positive swing it is possible that for certain events the common mode is so high that no segment is used to calculate the common mode. As a mathematical formula the "Mean value" algorithm can be expressed by

$$\mathcal{CM} = \sum_{0 \leq i < n} \left(raw[i] - pedestal[i] \right) / n \quad \text{with} \quad raw[i] < thr[i] \qquad (5.6)$$

in which $\mathcal{CM}$ is the common mode for the event, n is the number of segments with an ADC value below threshold, $raw[i]$ is the actual ADC value for segment i and $pedestal[i]$ and $thr[i]$ are the nominal pedestal and threshold of channel i respectively. Figure 5.8 shows the uncorrected and corrected pedestal of an arbitrarily se-
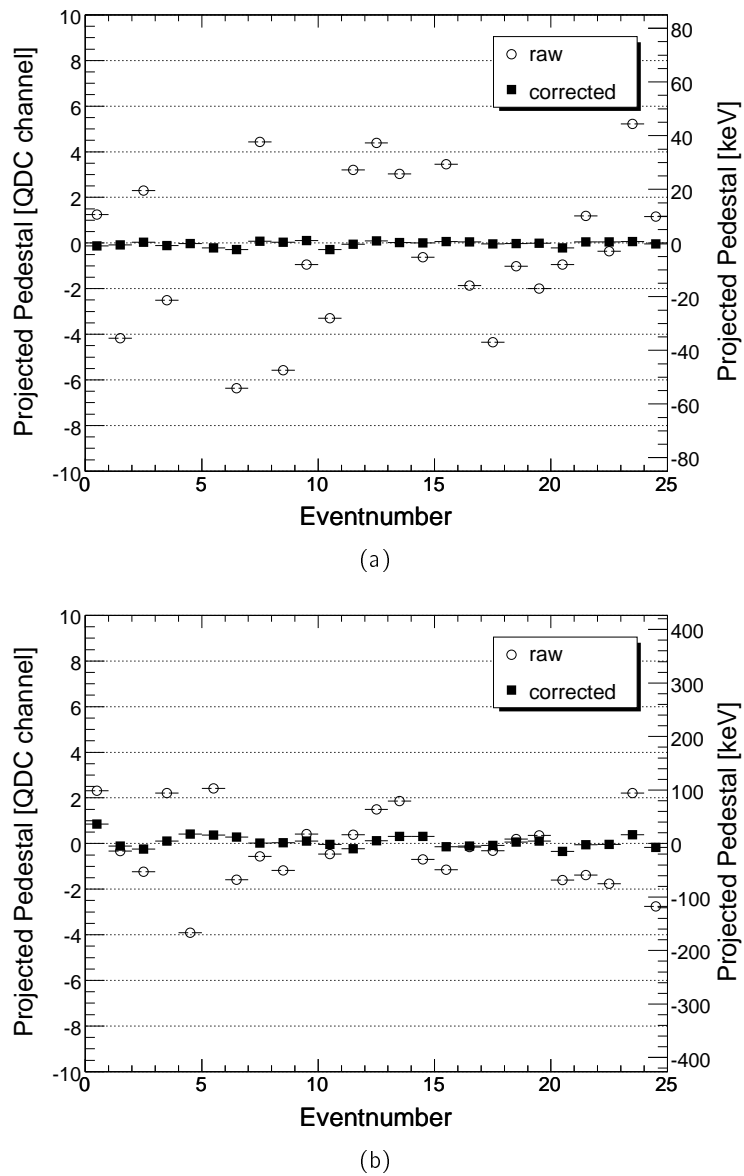
(a)

(b)

Figure 5.7: Event by event jump of the pedestal of one channel of the negative side of the thin detector (a) and the negative side of the thick detector (b) for 25 consecutive events. The circles represent the raw data, the squares the data after the common mode correction.

lected segment of the N-Side of the thin detector for data taken with and without zero suppression. Without correction the pedestal peak has a width of 69 keV or 8.1 ADC channels (FWHM) for the full data and a width of 71 keV or 8.4 ADC channels (FWHM) for the zero suppressed data. After the "mean value" common mode correction the peak width is significantly reduced. For the unsuppressed data the width is 24 keV or 2.8 ADC channels (FWHM) and for the data taken with zero suppression it is 22 keV or 2.6 ADC channels (FWHM).
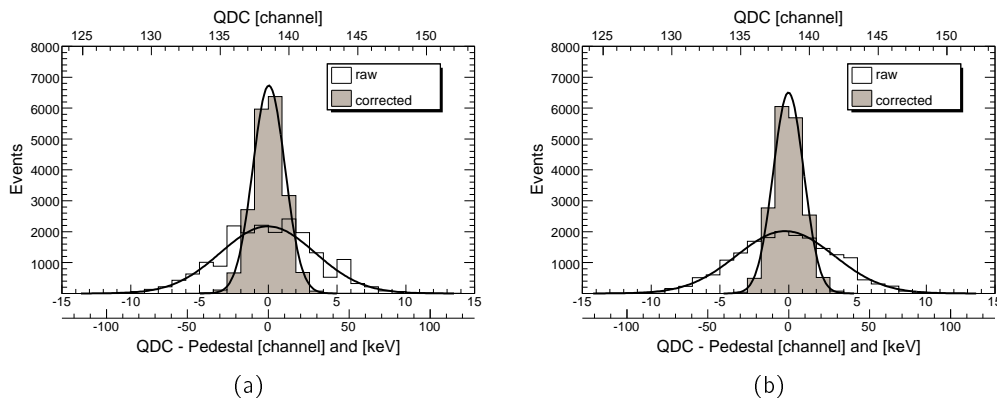

(a)   (b)

Figure 5.8: Raw (uncorrected) and common mode corrected pedestal of an arbitrarily selected segment of the negative side of the thin detector for data taken without zero suppression (a) and with zero suppression (b). The common mode correction was performed using the "mean value" method in both cases. Without correction (transparent histogram) the pedestals are 69 keV (a) and 71 keV (b) wide. After the correction the pedestals (filled histogram) have a width of 24 keV (a) and 22 keV (b).

5.3.2 Qsort correction

The second algorithm available for the off-line common mode correction is the "Qsort" method. The ADC value minus the nominal pedestal for each segment is added to a list and sorted. If the list has n elements then the common mode for the current event is the value at index $n/2$ of the list. Figure 5.9 shows the uncorrected and corrected pedestal of an arbitrarily selected segment of the N-Side of the thin detector for data taken with and without zero suppression. Before the correction the pedestal has a width of 69 keV or 8.1 ADC channels for the unsuppressed data and a width of 71 keV or 8.3 ADC channels (FWHM) for the reduced data. After applying the "Qsort" correction algorithm the width of the peak for both cases is 23 keV or 2.7 ADC channels (FWHM).

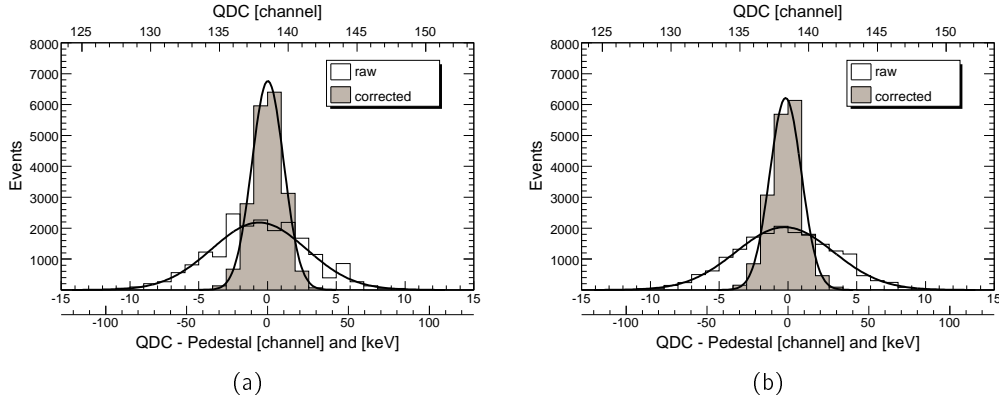(a)   (b)

Figure 5.9: Raw (uncorrected) and common mode corrected pedestal ("Qsort" method) of
an arbitrarily selected segment of the negative side of the thin detector for data
taken without zero suppression (a) and with zero suppression (b). Before applying
common mode correction (transparent histogram) the pedestals are 69 keV (a)
and 71 keV (b) wide. After the correction the pedestals (filled histogram) have a
width of 23 keV.
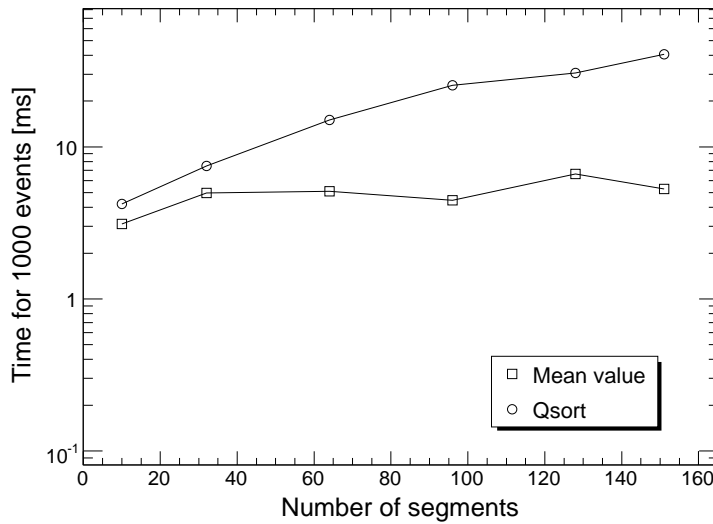

Figure 5.10: Time to perform the common mode correction as a function of segment number
for both introduced correction methods. The data points at 10 segments repre-
sent the processing of data taken with zero suppression. The data points at 96
segments represent both sides of the thick detector and the points at 128 and
151 the positive and negative sides of the thin detector respectively.

5.3.3   Comparison

Both methods show an equal correction quality independent on the type of data (with or without zero suppression). However, when comparing the performance of both methods then the "mean value" correction method has a clear advantage over the "Qsort" algorithm. Figure 5.10 shows the time needed to correct the common mode of 1000 events as a function of the number of segments. The data points at 10 segments represent data taken with zero suppression, the points at 96 segments both sides of the thick detector without zero suppression and the data points at 128 and 151 segments the P and N side of the thin detector respectively. For all chosen segment numbers the "mean value" algorithm is significantly faster which is a clear advantage. Even for data taken with zero suppression, which is the preferred mode, the "mean value" method is roughly two times faster than the "Qsort" method. However, the "mean value" algorithm requires a per segment threshold which has to be set in a correct way. In case the threshold is set too high, also segments with a real signal are considered in the calculation of the common mode which results in false values. On the other hand, a too low threshold may cause the algorithm to fail because for large values of the common-mode all segments might have ADC values that are above the threshold.

The calculations have been conducted on a PC with a 1.3 GHz Intel Celeron M Processor running Ubuntu-Linux [55] with version 3.3.5 of the GNU C/C++ compiler family [56].

5.4   Detection Resolution

By exploiting the $\Delta E/E$ method it is possible to identify and distinguish between stopped protons and deuterons. To give an estimate on how well the separation of both particle works, it is reasonable to give the detection resolution as a number for the combination of two detectors. Figure 5.11(b) shows a projection of the ΔE vs. E plot along the solid line in figure 5.11(a). In figure 5.11(a) the calculated bands for protons and deuterons are indicated by dashed lines. The line marking the projection axis is perpendicular to the proton band at 5 MeV energy loss in the thick detector. However, due to the different axis scales for the energy losses in the thick and thin detectors the projection axis does not seem to be perpendicular to the proton curve. A fit by a combination of two gaussians to the resolution plot yields the band separation which is roughly $3.8\,\sigma$.

Due to the absence of an absolute energy reference[1] the quality of the obtained energy calibration can only be given by the distance between the proton and deuteron bands in figure 5.11(b). In the figure the distance is 499 keV while a value of 527 keV is expected from the calculations. The reason for the deviation of $\approx 6\,\%$ to the expected

---

[1]Irradiating each detector with an α source would provide an absolute energy reference, to which the calibration can be adjusted.
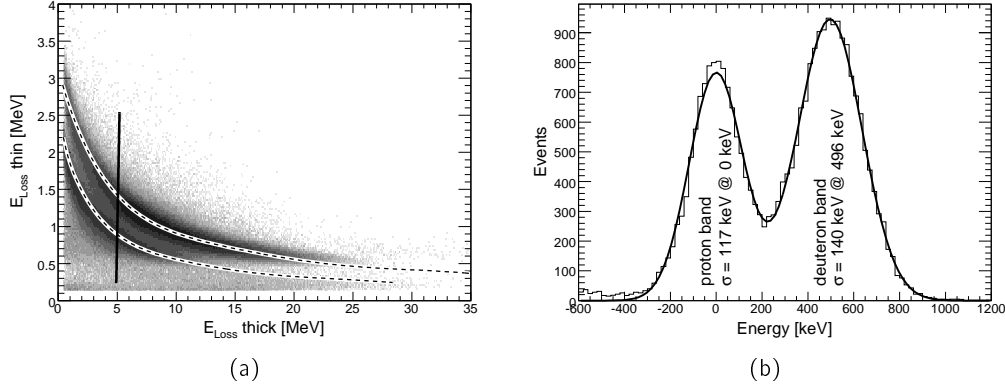
(a)   (b)

Figure 5.11: (a) Energy loss of a hit in the thin detector versus the energy loss of a hit in the thick detector. The calculated proton and deuteron curves are indicated as dashed lines. The projection axis for the resolution plot is shown as a solid line. The axis is perpendicular to the proton band at 5 MeV energy loss in the thick detector. (b) Projection along the solid line shown in the ΔE vs. E plot.

(a)   (b)
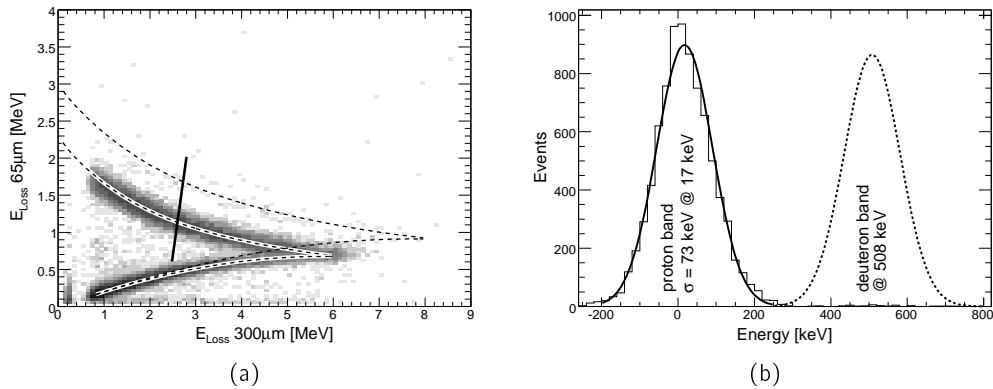
Figure 5.12: (a) Energy loss of a hit in a 65 μm thick detector versus the energy loss of a hit in 300 μm detector. The data has been taken with a first version of the tracking telescope. As in figure 5.11(a) the calculated proton and deuteron curves are indicated as dashed lines and the projection axis for the resolution plot is shown as a solid line. (b) Projection along the axis indicated in the ΔE vs. E plot. The expected projection of the deuteron band is indicated by a dashed line assuming that the resolutions for protons and deuterons are equal.

value is a remaining non-linearity from the test-pulse measurements, that can not be corrected for by the two subsequent fits to real data.

For comparison, figure 5.12 shows the same two plots for data taken with a first version of the tracking telescope [37]. It was equipped with a 69 μm thick double-sided Silicon detector as a first layer and a 300 μm detector as a second layer. The front-end electronics utilized the VA32HDR [36] amplifier and TA32cg [38] trigger chips. The projection axis for the resolution plot has been chosen to be perpendicular to the proton band at 2.5 MeV energy loss in the 300 μm detector. Due to the absence of deuterons in the data, the expected deuteron peak in the resolution plot is indicated by a dashed gaussian assuming equal resolutions for both protons and deuterons. The separation of the two bands is approximately 7 σ.

Chapter 6

Track reconstruction with the Telescope

In order to fix the momentum of the initial neutron in a proton-neutron reaction within the spectator model, the precise knowledge of the four-momentum of the detected spectator proton is required. In case one investigates inelastic proton-neutron interactions with additional particles in the final state this gives also the opportunity the measure at different excitation energies by selecting certain ranges of the polar angle θ of the detected spectator proton.

Moreover, the knowledge of the track of a particle will allow to reconstruct the vertex of the reaction in two dimensions on an event by event basis. For an identified reaction with known kinematics it is also possible to precisely align the silicon tracking telescope and with respect to D2 and other ANKE detection systems.

In a first approximation the reconstructed tracks are assumed to be straight lines between the hits in the detectors. Later, corrections due to the magnetic field of the D2 spectrometer magnet are applied to the track parameterization.

6.1 Detector Hits

A track is defined as a straight line between two correlated hits, in the thin and in the thick detector. Each hit contains the information about the energy loss of the particle and its position in the detector. In a first stage each side is analyzed separately resulting in hits that carry the position information only in dimension, in the analysis these hits are called "one-dimensional" hits. Later the 1D hits are combined to form "two-dimensional" hits with the full position information. Besides the position in the detector frame itself, the hit carries its position in the telescope and the ANKE reference frames. The detector reference frame is defined as x and y being the coordinates in the detector plain and z being the coordinate along the thickness of the detector with the origin being in the center of the detector. In particular, x is measured by the positive pulsing side and y is measured by the negative pulsing side. The telescope coordinate system

is a copy of the ANKE system rotated by the D1 deflection angle around the y axis and shifted to the nominal target position.

6.1.1 One-dimensional Hits

In a first stage of the hit generation each detector side is analyzed separately in order to get a list of one dimensional hits. The hit finding algorithm is best explained by figures 6.1(b) and (c) in which the energy loss distribution of a single event is shown. The algorithm loops over the list of segments of a side and checks if the energy loss of a segment is above the primary threshold of that segment. For the event displayed in the figure this condition is met by segment 74. Once a segment is found to be above its primary threshold the algorithm goes back and forward in the list and adds the energy losses of all segments that have an energy loss above the secondary threshold. In the example segment 73 meets the condition when the algorithm is going backwards and segments 75, 76, 77 and 78 have the required energy loss when going forward in the list. The secondary threshold is chosen in such a way that the size of the hit (the number of segments comprising the hit) is reasonable (depending on the type of the detector) and to reduce the errors introduced by the energy loss summation. A low secondary threshold increases the size of the hit, which in an extreme case might lead to a combination of two physical hits to one hit. A high secondary threshold decreases the size but increases the error in the energy loss determination because not all segments are taken into account. The position of the hit in the detector reference frame is defined by the weighted energy loss center of all segments in the hit. Figure 6.1(a) shows a typical energy loss histogram for the negative pulsing side of the thick detector.

6.1.2 Two-dimensional Hits

In the second stage of the hit determination the one dimensional hits from both sides are combined. The criteria to decide whether two 1D hits belong to the same 2D hit is that both energy losses may only differ by a certain percentage, that depends on the detector type. Figure 6.2 shows the energy loss for a hit on the negative pulsing side versus the energy loss for a hit on the positive pulsing side. When the two dimensional hits are generated, the third coordinate (z) of the hit is set to zero. For the first detector this approach is reasonable because the thin detector works as a transmission detector, which means that the energy is deposited homogeneously along the path of the particle. Figure 6.3 shows a sketch of a hit in the thin detector. For particles that are stopped in the thick detector the situation becomes more complicated because the z coordinate of the hit can no longer be assumed to be in the middle of the detector.

6.1.3 Particle identification

With the energy loss information for the hits in both detectors it is possible to identify the particle by the $\Delta E/E$ and PID [57, 58] methods. On the left side of figure 6.4 the $\Delta E/E$ plot is shown. On the right side the PID versus the total energy loss is plotted.
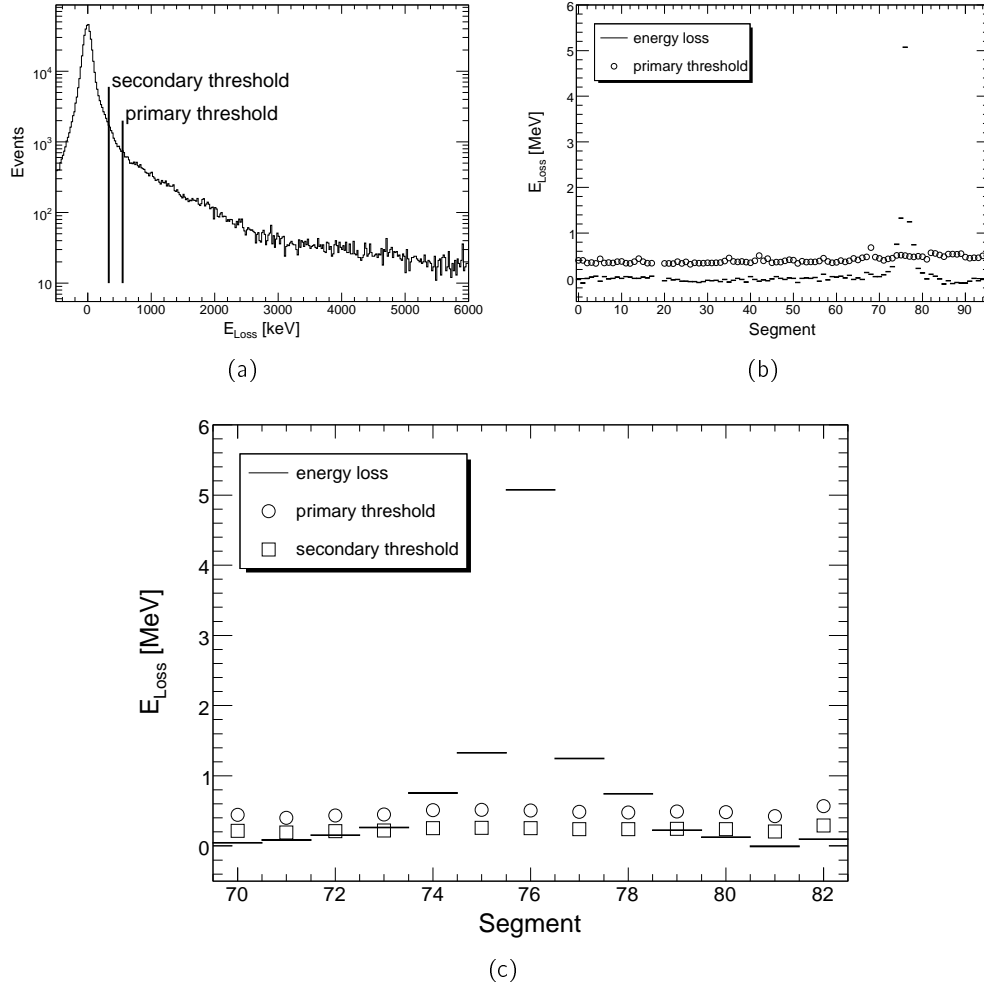
(a)

(b)

(c)

Figure 6.1: Typical energy loss histogram for a segment of the negative pulsing side of the thick detector (a). The primary threshold is located at 5σ of the pedestal width which corresponds to ≈ 550 keV. The secondary threshold is set to 3σ of the pedestal width or ≈ 330 keV. In (b) the distribution of energy losses for a single event over all segments of the negative pulsing side of the thick detector is shown. The individual primary thresholds are indicated by circles. (c) displays a zoom on the region of the detector which was struck by a particle. The secondary thresholds are indicated by boxes.

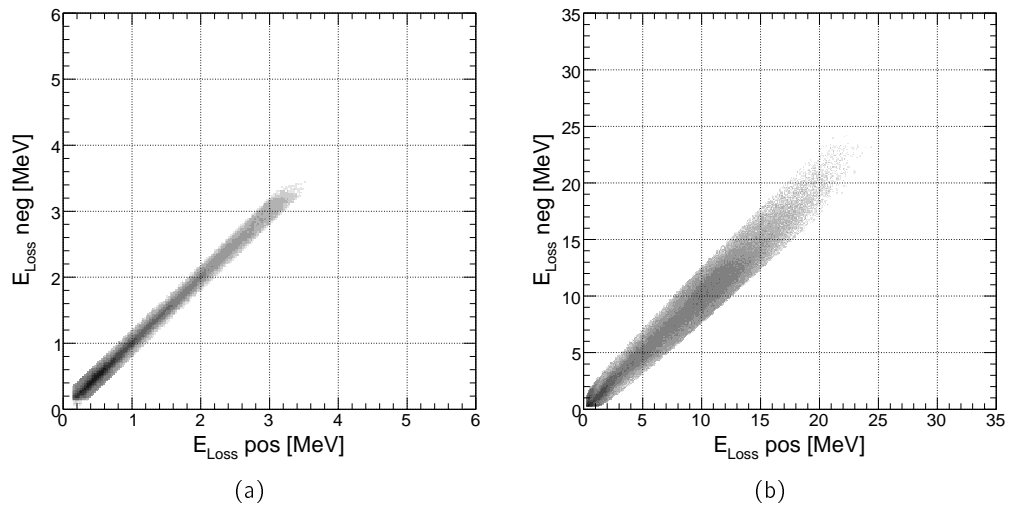(a)   (b)

Figure 6.2: Energy loss of a hit in the negative pulsing side vs. the energy loss of a hit in the positive pulsing side for the thin (a) and the thick (b) detector.
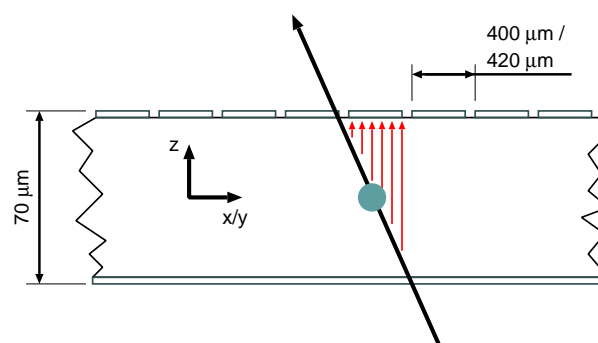

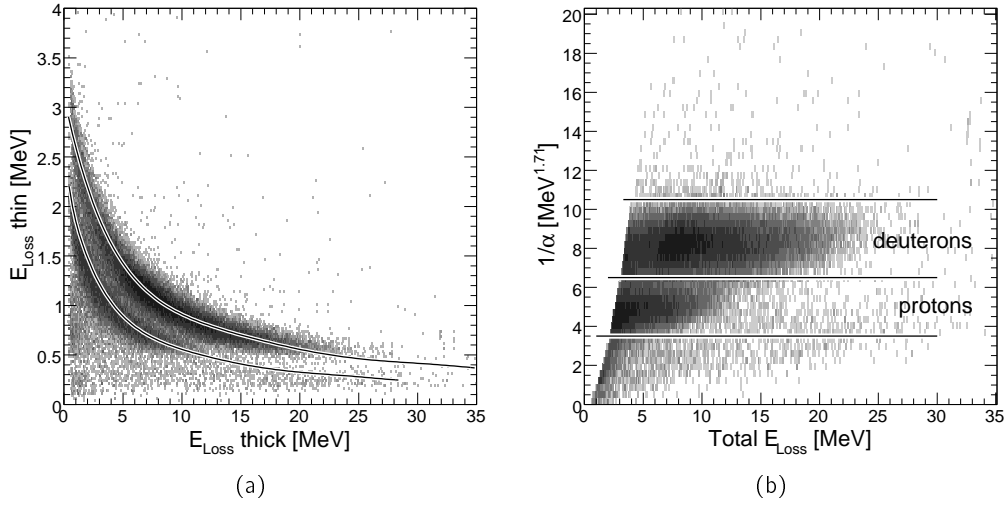Figure 6.3: Sketch of a track in the thin detector.

Figure 6.4: (a) ΔE-E and (b) PID plots for data from the beam-time in November 2003.

The PID is defined by equation 6.1 in which ΔE is the energy loss of the particle in the thin detector and E is the energy loss in the thick detector. In the PID vs. total energy loss plot each particle type contributes to a horizontal band.

$$\frac{1}{\alpha} = (\Delta E + E)^{1.71} - E^{1.71} \qquad (6.1)$$

A cut around the bands in both plots allows the selection of certain particles for further analysis.

6.1.4 3D position information from the thick detector

Figure 6.5 shows the track of a stopped particle in the thick detector. Most of the energy is deposited at the end of the track. With the measured energy in the thick detector and the knowledge of the particle type it is possible to calculate the penetration length in the silicon detector. Figure 6.6 shows the range of protons and deuterons as a function of the initial kinetic energy.

By this method the z position of a hit in the coordinate system of the thick detector can only be extracted for identified and stopped particles (in our case protons and deuterons). Figure 6.7 shows a sketch of the principle of the reconstruction method. t is the thickness of the detector, d is the calculated penetration length and a and b are the coordinates of a hit in the thin detector in the reference frame of the thick detector.

$$x = \frac{a \cdot z}{b + z} \qquad (6.2)$$
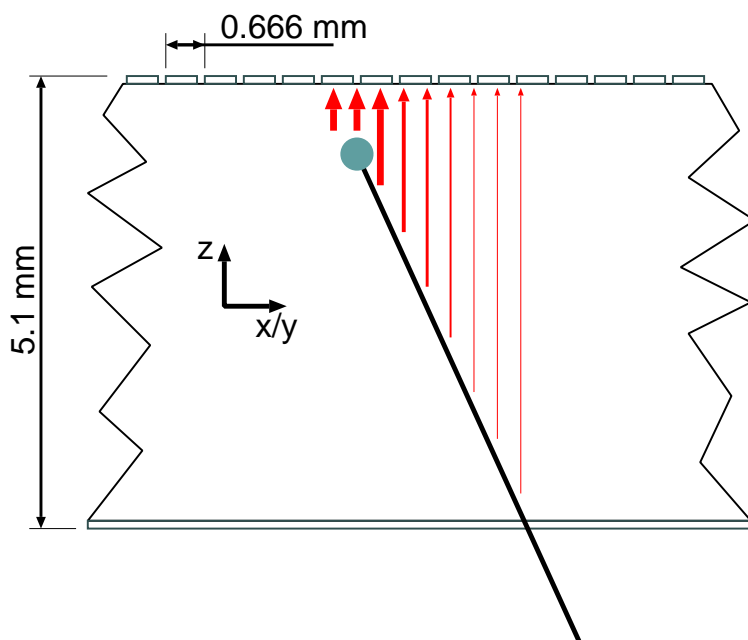
$$d^2 = x^2 + z^2 \qquad (6.3)$$

Figure 6.5: Sketch of the track of a stopped particle in the thick detector. The amount of deposited energy along the path is illustrated by the thickness of the arrows.
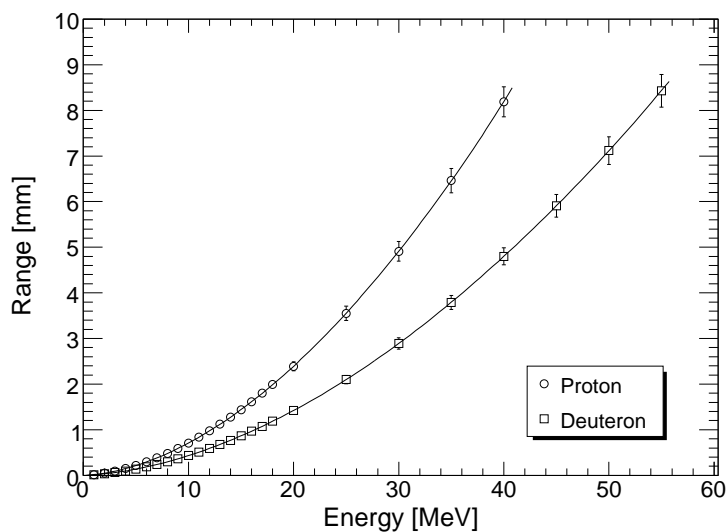

Figure 6.6: Range of protons and deuterons in silicon as a function of the initial kinetic energy. The error bars show the longitudinal straggling.
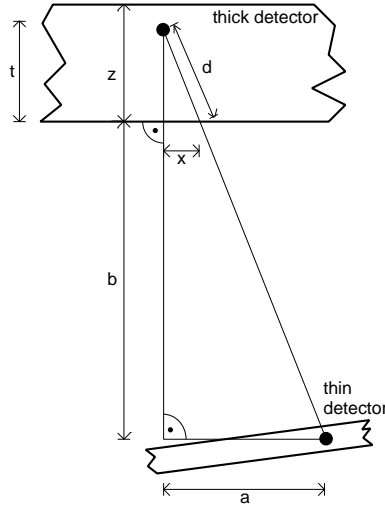
Figure 6.7: Determination of the z-coordinate of a hit in the thick detector.

$$z^2 + \frac{a^2 \cdot z^2}{(b+z)^2} - d^2 = 0 \qquad (6.4)$$

Equations 6.2 and 6.3 result from geometrical considerations. The missing z coordinate of the hit in the thick detector is obtained by finding a $z \in [0, t]$ that solves equation 6.4 which is the combination of equations 6.2 and 6.3.

6.2   Track Reconstruction

The track of a particle is parameterized by its vertex and a direction (θ and ϕ with respect to the nominal beam axis), and in a first approximation defined by a straight line between the 2D hits in the detection layers. Since a valid track has to originate from the target, a cut on the target region can be made by cutting on the strip-strip bands for the hits in the thin and the thick detector. Figure 6.8 shows the two correlation plots which are used to make a cut on the target region.

6.2.1   Determination of the y and z coordinates of the target

With knowledge of the track parameters it is possible to reconstruct the position and extension of the target. Figure 6.9 gives a sketch of how the reconstruction is performed. The straight line track is defined by the two hits (red dots in the figure). The intersection of the track with a $y - z$ plane at the x coordinate of the target results in the green dot in the figure. The histogram of the y and z coordinates of this intersection point over a sample of tracks gives the mean position as well as the extension of the target in y and z direction. Figure 6.10 shows the y and z target
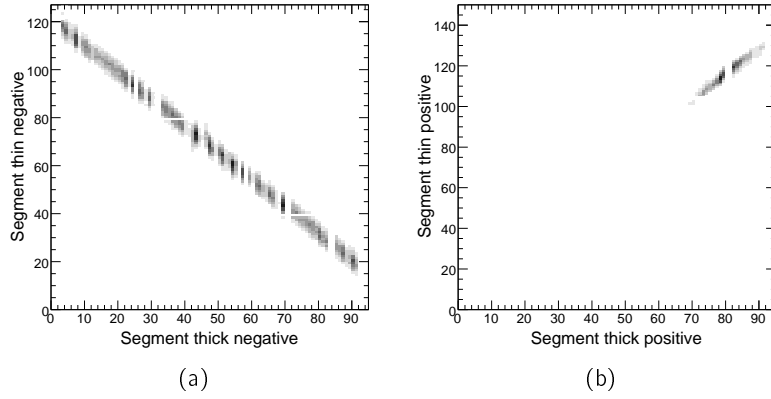
Figure 6.8: Strip-strip correlation plots for hits in the thin and thick detectors.

position and extension for data from the beam-time in November 2003. The given coordinates are with respect to the telescope reference frame.

6.2.2   Determination of the x coordinate

The performance of the reconstruction of the y and z coordinate of the target point strongly depends on the correct knowledge of the x coordinate of the intersection plane (x coordinate of the target). The x coordinate of the target can be determined by minimizing the width of the y and z target distributions. If the position of the intersection plane has been chosen correctly the y and z distributions must have minimum width. Figure 6.11(a) shows the projection of a sample of proton tracks from the November 2003 data onto the $x - y$ plane. The width of the projection in y direction strongly depends on the x coordinate. A distribution of the sigma of a Gauss fit over a y slice of the projection as a function of x is shown in figure 6.11(b). The x coordinate at which the distribution has its minimum is the position of the target and the intersection plane. For correct operation of the method it is however necessary to have the tracks over a wide range of θ and ϕ angles. In the above example in which the y coordinate of the intersection point was used to reconstruct x all possible ϕ angles where available. Due to this, the track projection onto the $x - y$ plane shows good sensitivity to the x coordinate. For a cross check it is also possible to use the z coordinate of the intersection point in order to reconstruct the x position of the target. For the November 2003 data in which the θ track angles were only in a limited range this was not possible. Figure 6.11(c) shows the track projection onto the $x - z$ plane. From the figure it can be seen that the $x - z$ projection is not sensitive to the x coordinate of the target.
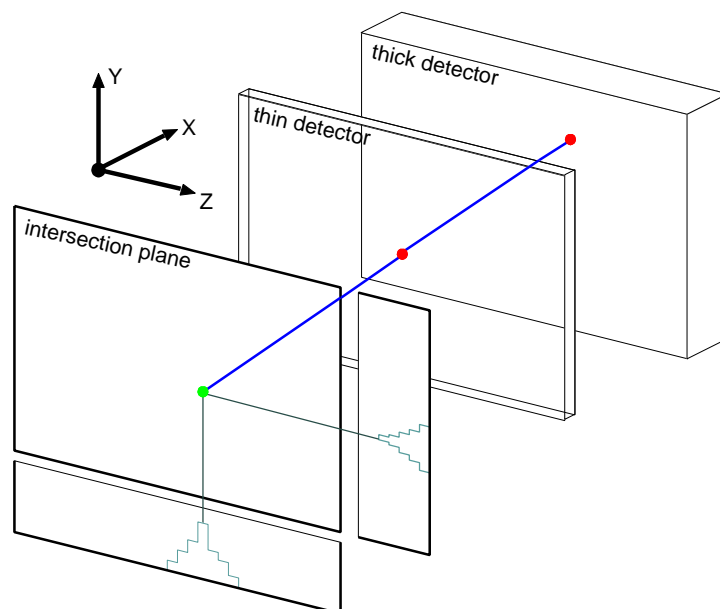
Figure 6.9: Sketch of the vertex/target reconstruction with a straight line track through the hits in the thin and thick detector.

(a) (b)
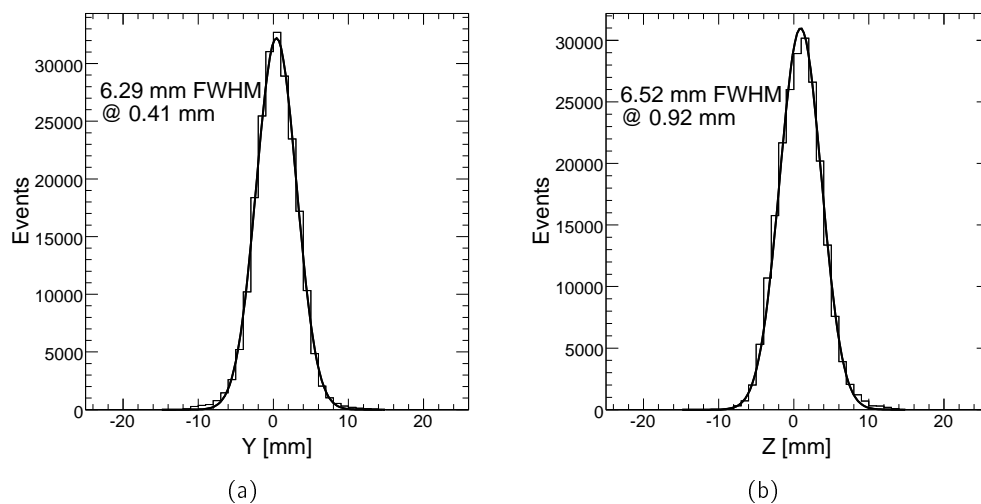
Figure 6.10: Position and extension of the target for the November 2003 charge exchange beam-time.

(a)

(b)

(c)
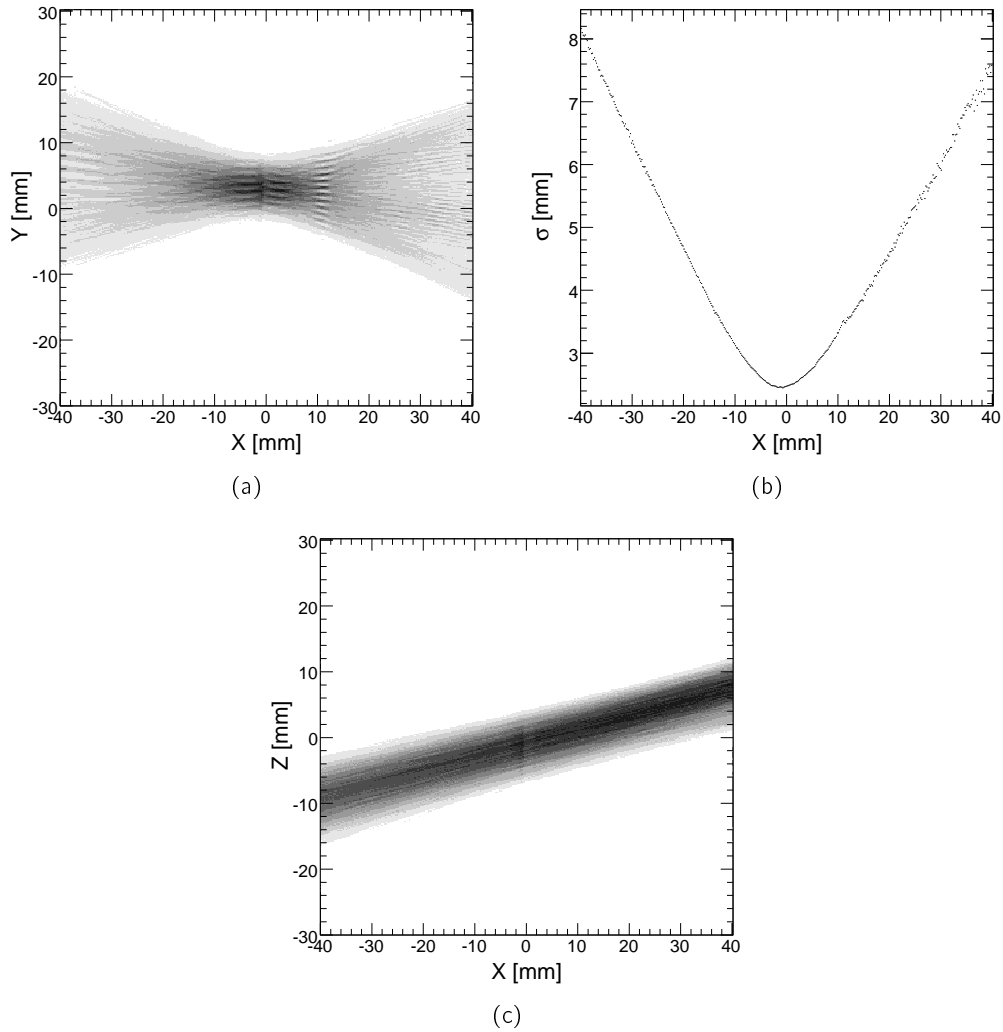
Figure 6.11: Projection of a sample of proton tracks from the data taken in November 2003 onto the $x - y$ plane (a). Distribution of the sigma of a Gaussian fit over a y slice of the projection in the $x - y$ plane as a function of x (b). In (c) the projection onto the $x - z$ plane is shown. Since the θ angles of the tracks in the sample were limited to a small angular range it is not possible to reconstruct the x position of the target from the $x - z$ projection plot.
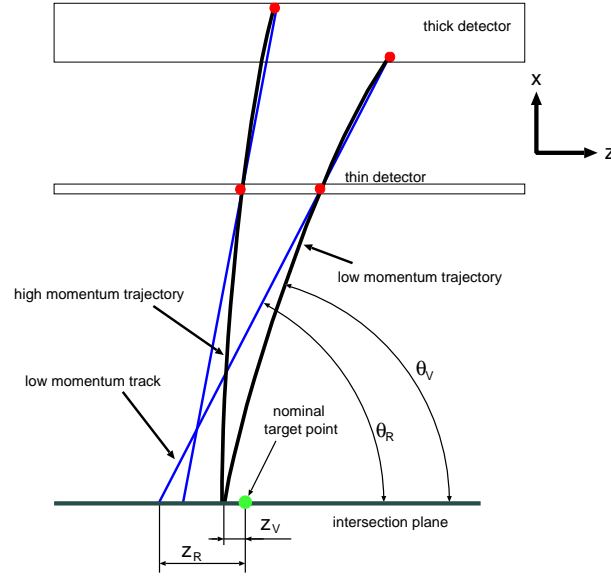
Figure 6.12: Exaggerated sketch of the influence of the magnetic field on the track parameters. z_R and θ_R are the track parameters obtained by the straight line approach. z_V and θ_V are the true z-coordinate and θ-angle at the vertex. z_R and θ_V are both positions given with respect to the nominal target point.

6.3 Magnetic field correction

The tracking telescope is located inside the target chamber in which the influence of the D2 magnetic field to the track parameters can not be neglected. In order to check this influence and if necessary introduce corrections to the track parameters obtained by the straight line approach a Geant4 simulation has been used [59, 60]. In the simulation a point like target at $x = y = z = 0.0$ mm (in the telescope reference frame) was chosen, multiple scattering was switched off and protons and deuterons were generated into the full acceptance of the tracking telescope. In the analysis of the simulated data only stopped particles were taken into account. In the following θ_R, ϕ_R, x_R, y_R and z_R shall be the track parameters reconstructed by the straight line method and θ_V, ϕ_V, x_V, y_V and z_V are the true parameters at the vertex.

Figure 6.12 shows an exaggerated sketch of the influence of the magnetic field on the above mentioned track parameters. The lower the momentum of the stopped particle is, the further the reconstructed z coordinate is shifted to negative values. A similar dependence is visible for the track θ angle. z_R and θ_V are both positions given with respect to the nominal target point.

6.3.1 The x coordinate of the target

To determine the x coordinate of the target (which must be at 0.0 mm) the method described in section 6.2.2 has been used. Since the generated events covered the whole telescope acceptance it was possible to reconstruct x_R both via the y and the

particle	x_R via y	x_R via z
proton	$-0.012\,\text{mm}$	$-0.026\,\text{mm}$
deuteron	$+0.018\,\text{mm}$	$+0.011\,\text{mm}$

Table 6.1: Reconstructed x_R coordinate of the target for the simulated data.

z coordinates of the intersection point. The results are summarized in table 6.1. A dependence of the reconstructed target x coordinate on the particle momentum could not be seen.

6.3.2 The z coordinate of the target and the track θ angle

The major component of the D2 magnetic field in the target region is in y direction. Thus a strong dependence of the reconstructed z coordinate of the target and the θ angle of the track on the particle momentum is expected.

A magnetic field correction can be expressed by the following equations:

$$\theta_V = \theta_R - \Delta\theta(p) \tag{6.5}$$

$$z_V = z_R - \Delta z(p) \tag{6.6}$$

in which $\Delta\theta(p)$ and $\Delta z(p)$ are offsets due to the magnetic field and depend only on the particle type and momentum. The difference of θ_R and z_R to the nominal values given by the Geant4 event generator are displayed in figures 6.13(a) and (c) for protons and 6.14(a) and (c) for deuterons. For both particles a clear shift and a tail to negative $\Delta\theta_R$ and negative Δz_R values is visible. Figures 6.13(b) and (d) and 6.14(b) and (d) show $\Delta\theta_R$ and Δz_R as a function of the particle momentum. In all four plots a clear dependence on the particle momentum is visible. To correct the effects shown in figures 6.13(a) through (d) and 6.14(a) through (d) a fit by a function

$$f(p) = C_0 \cdot e^{C_1 \cdot p + C_2} + \frac{C_3}{C_4 \cdot p + C_5} + C_6 \cdot p^2 + C_7 \cdot p + C_8 \tag{6.7}$$

can be made for all four cases. Figures (e) through (h) of 6.13 and 6.14 display $\Delta\theta_V$ and Δz_V as well as their dependence on the particle momentum for both particle types. The shift and the tail to negative angles and negative z values is removed. The dependence on the particle momentum is removed in all four cases.

6.3.3 The y coordinate of the target and the track ϕ angle

In the $x - z$ plane the magnetic field has a significant influence on the track parameters. Figure 6.15 shows $\Delta\phi_R$ and Δy_R as a function of the particle momentum for protons and deuterons. In the $x - y$ plane the magnetic field has hardly any influence on the track parameters which makes a correction unnecessary.

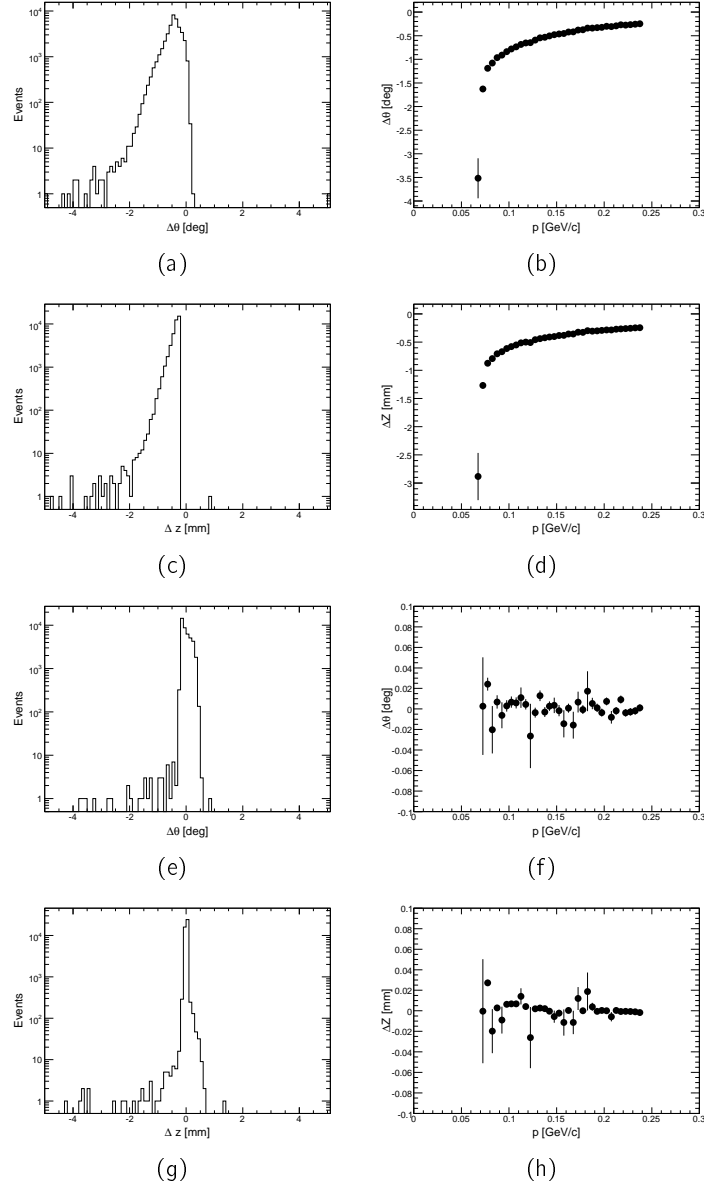Figure 6.13: $\Delta\theta_R = \theta_R - \theta_{generator}$ and $\Delta z_R = z_R - z_{generator}$ for protons without ((a)-(d)) and with ((e)-(h)) the magnetic field correction. A constant shift and a tail to negative angles and negative Δz values is visible in the uncorrected plots.
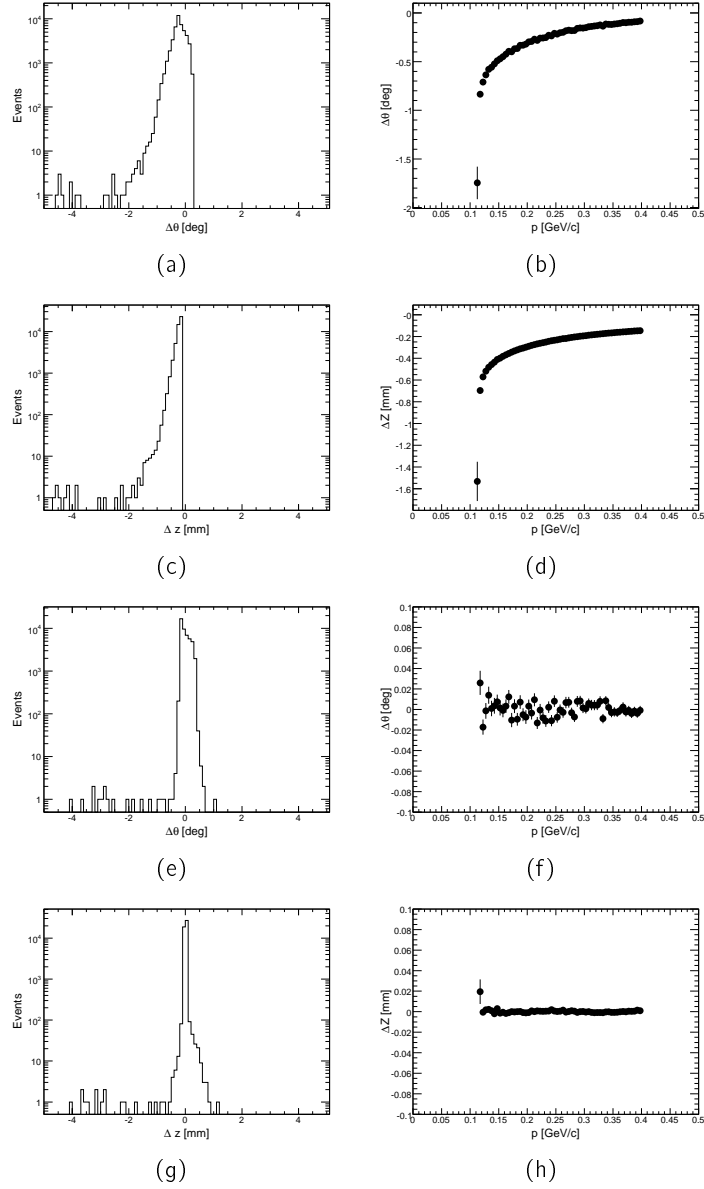
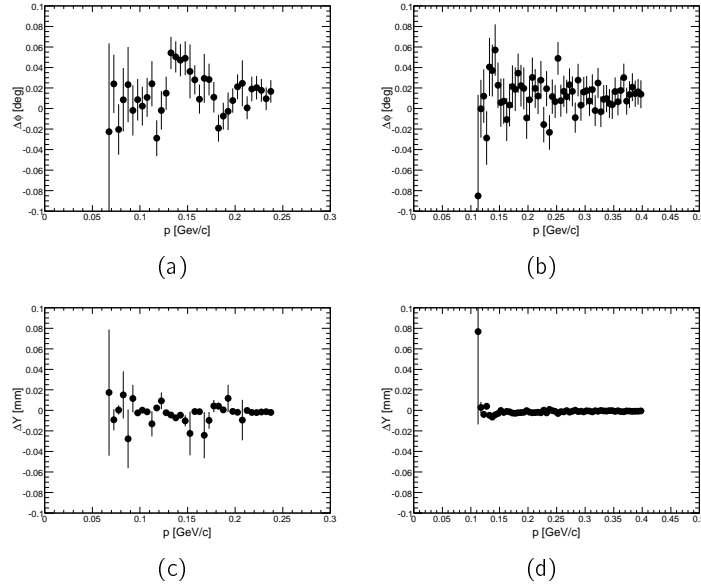Figure 6.14: $\Delta\theta_R$ and Δz_R for deuterons without ((a)-(d)) and with ((e)-(h)) the magnetic field correction.

Figure 6.15: Influence of the momentum and the track θ and ϕ angles on the track parameters in the $x - y$ plane for (a,c) protons and (b, d) deuterons.

6.3.4 Cross-Check of the magnetic field correction

To get an estimate of the errors introduced by the reconstruction a second simulation has been done. In this simulation run an extended target with a spherical shape with a radius of 2.5 mm has been chosen. In addition multiple scattering has been switched on. In the reconstruction code θ and ϕ are directly extracted from the information from the detectors while y_V and z_V depend on the position of the intersection plane. It is therefore reasonable to split the track parameters into two categories. One for the directly measured and one for the indirectly measured parameters.

θ_V and ϕ_V

Figure 6.16 shows the differences $\Delta\theta_V$ and $\Delta\phi_V$ of the measured parameters to the nominal values given by the Geant4 event generator. For $\Delta\theta$ the values after the magnetic field correction are plotted. In both cases the peak is centered around 0 deg which means that the reconstruction method does not introduce any offsets. This is especially crucial for θ which already includes the magnetic field correction. For θ_V the standard deviation is 0.46 deg for ϕ_V it is 0.48 deg.

x_V, y_V and z_V

The major drawback of having mostly single track events in the telescope is that one is insensitive to x_V on an event by event basis. In the reconstruction x_V is assumed to be equal to x_R which is the x coordinate of the center of the target. Thus the real x_V can be anywhere between $x_R - 0.5 \cdot \Delta x_T$ and $x_R + 0.5 \cdot \Delta x_T$ with Δx_T being the
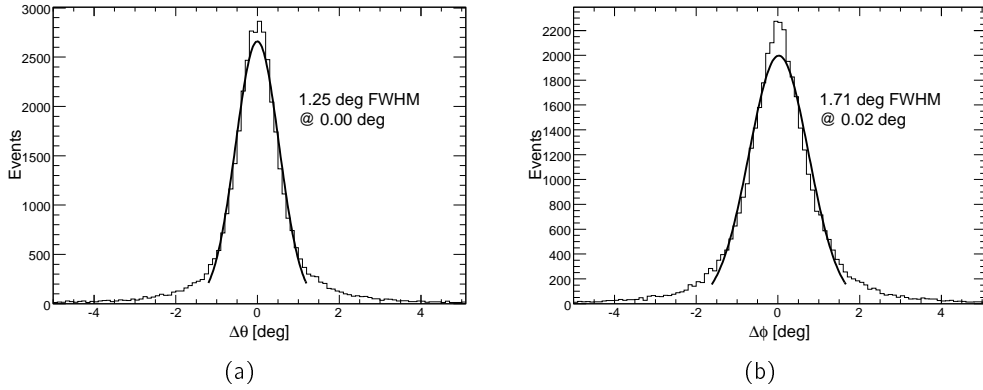
Figure 6.16: $\Delta\theta_V$ (a) and $\Delta\phi_V$ (b) for the simulated data with extended target and multiple scattering switched on.

size of the target in x direction. Figures 6.17(a) and (b) display Δy_V, the difference of y_V to the nominal values, and Δy_V versus x_G, the x position of the origin of the simulated particle. The plot in 6.17(a) is the projection of plot 6.17(b) to the y axis. For Δy_V the standard deviation is 0.62 mm. Figures 6.17(c) and (d) show similar plots for the z coordinate at the target. Δz_V strongly depends on x_G due to the influence of the magnetic field. Since the 1D plot is again the projection of Δz_V versus x_G the standard deviation for Δz_V is larger than in case of Δy_V. For Δz_V it is 0.65 mm.

6.3.5   Application to real data

Up to this point all plots and data concerning the magnetic field correction have been based upon Monte-Carlo simulations. A next step to check the magnetic field correction is to apply it to real data. In an ideal case the correction should eliminate the dependency of the track parameter on the momentum of the particle. For the reconstruction of the z position of the target the check is straight forward because the target z position is independent on the investigated physics. The histogram in figure 6.18(a) shows this behavior for protons. The data points indicated by solid triangles represent the mean z position with magnetic field correction, the z position without magnetic field correction is indicated by squares. In addition the correction function is drawn as a solid line. The uncorrected data points match the development of the correction function. For the θ angle however, the situation is more complicated since the physics itself introduces a correlation between θ and the momentum. To perform the check also for θ it is necessary to identify a single reaction channel and compare the experimental θ vs. momentum correlation with the theoretically calculated one. Figure 6.18(b) displays θ as a function of the deuteron momentum for dd-elastic events. Again, the corrected data points are indicated by solid triangles and the uncorrected points by squares. The solid line represents the correction function and

(a)

(b)

(c)

(d)
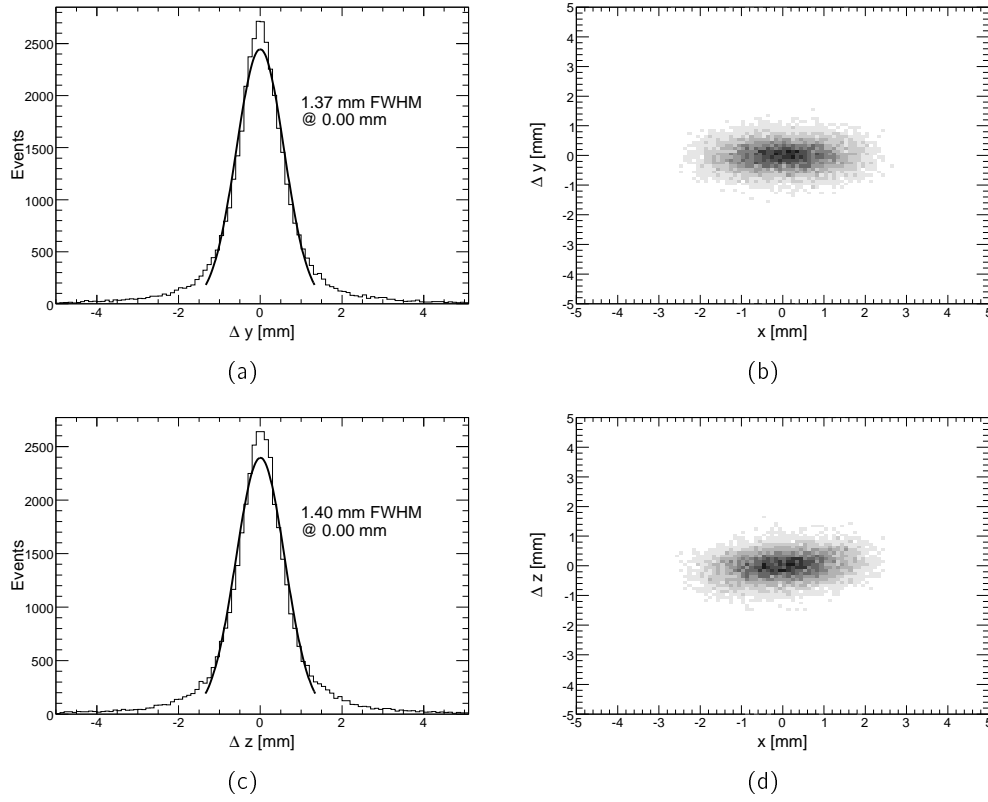
Figure 6.17: Δy_V (a), Δy_V vs. x_G (b), Δz_V (c) and Δz_V vs. x_G (d) for the simulated data with extended target and multiple scattering switched on.

the dashed line the kinematically calculated correlation.

6.4 Alignment

To get the correct position of the detectors with respect to each other and the target chamber, the tracking telescope has been measured by the Central Department of Technology of the research center. The measurements comprised the determination of the positions of the center of each detector with a precision of better than $10\,\mu m$ as well as the rotation around all three axes with a precision of better than $10\,mrad$.

The most powerful tool to check the measurements and the correct alignment of the detectors are the correlations between the y and z coordinates of the target and the track angles ϕ and θ. In all cases the reconstructed target coordinate must be independent on the track angles. Figures 6.19(a) through (d) show the target y and z coordinates versus the track ϕ and θ angles with the inclination of the bands printed in each plot. For each case the inclination is below $0.005\,mm/deg$. Figures 6.19(a)
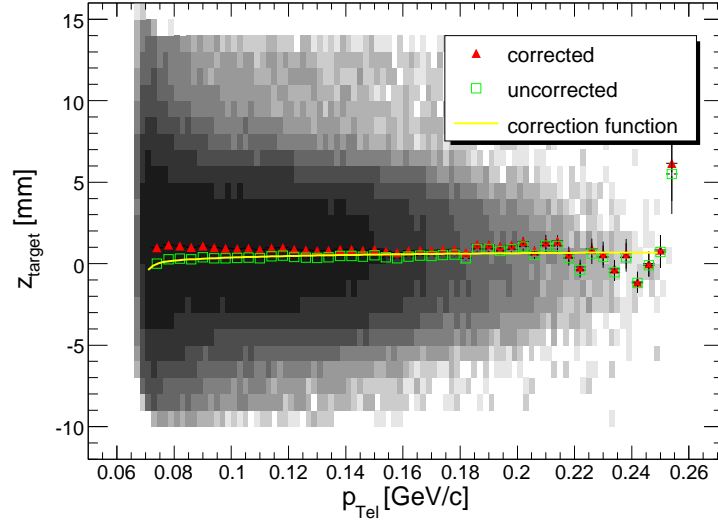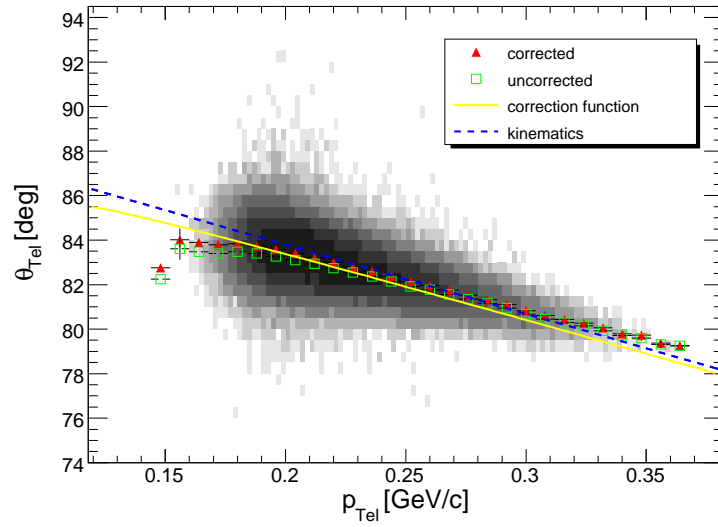
Figure 6.18: Reconstructed target z position (a) and θ (b) as a function of the particle momentum with and without the magnetic field correction for dd-elastic events.
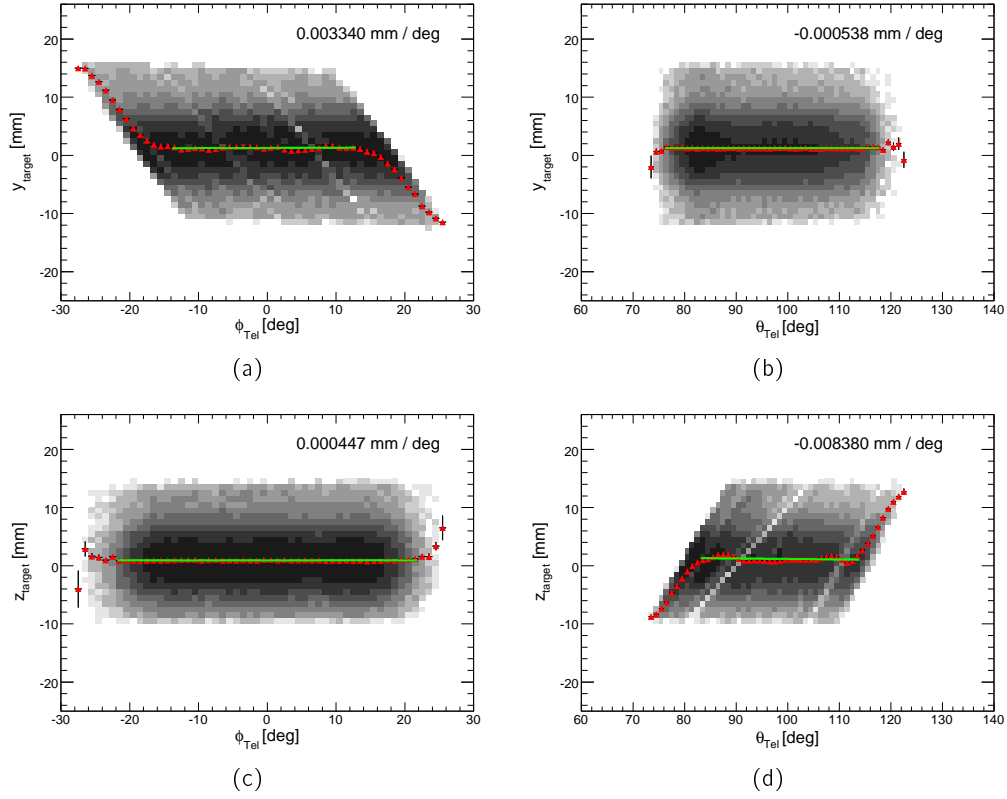
Figure 6.19: y_{target} vs. ϕ (a) and θ (b) and z_{target} vs. ϕ (c) and θ (d) for protons.

and (d) also show the acceptance of the telescope arrangement. For large ϕ angles for instance, only the lower part of the target is imaged while for small ϕ angles the upper part is visible. Another tool to check the alignment is the θ vs. ϕ plot which must also show no dependence. Figure 6.20 shows the θ vs. ϕ distribution of deuterons for different momentum ranges (figures (a)-(c)) and all momenta (figure (d)). The inclination of each of the bands is printed in the plots. The maximum inclination is $\approx 0.0138\,\mathrm{deg}_{\theta}/\mathrm{deg}_{\phi}$. For a check of the absolute alignment and positioning an identified reaction has to be consulted. Figure 6.21(a) shows the θ angle of the deuteron in the tracking telescope versus θ of the forward going deuteron for dd-elastic at a beam momentum of 2.40 GeV/c. The solid line indicates the kinematical calculation for this reaction and it is seen that the experimental data points agree very well with the calculation. The difference in the ϕ angles for both detected deuterons is displayed in Figure 6.21(b). A peak very close to 180° is visible in the plot which must be the case since for any two-body elastic reaction the two outgoing particles and the incoming beam particle lie in the same plane.

A further possibility to check the validity of the reconstructed tracks as well as the energy calibration is to plot θ of a particle detected in the telescope against its

(a) 120 MeV < p < 200 MeV

(b) 200 MeV < p < 280 MeV

(c) p > 280 MeV

(d) p > 120 MeV
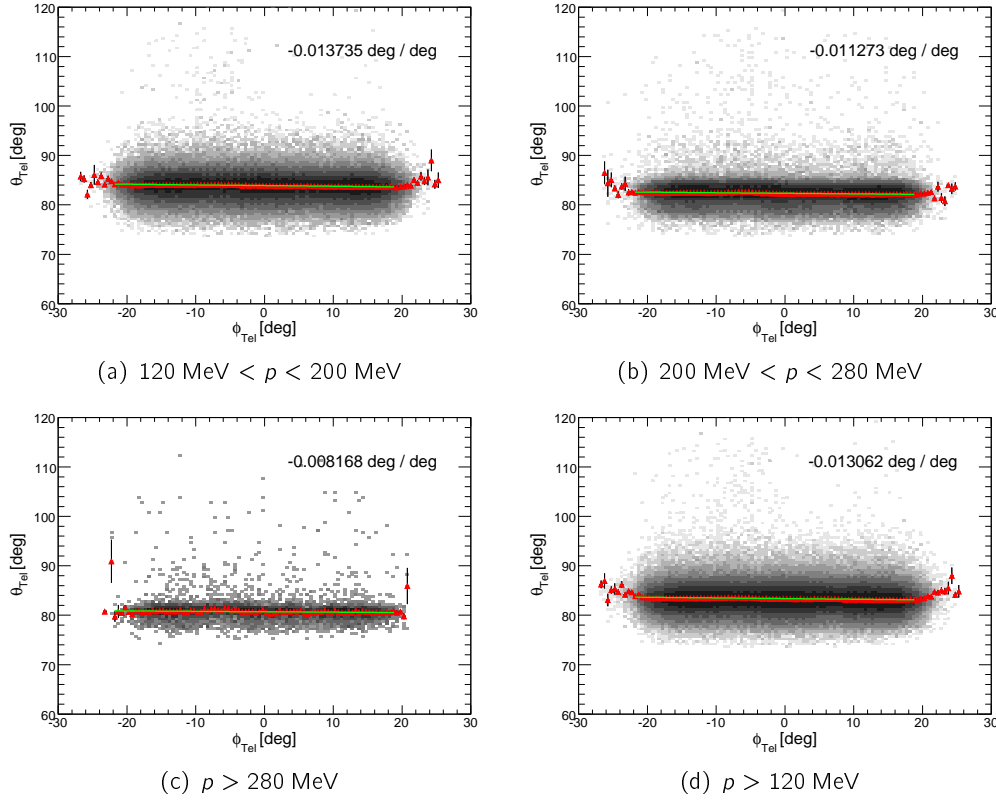
Figure 6.20: θ vs. ϕ for deuterons for different momentum ranges ((a)-(c)) and for all momenta (d).

momentum for a known elastic reaction. Such a plot is shown in figure 6.18(b) which has originally been used to demonstrate the magnetic field correction. In the plot the band is slightly inclined with respect to the kinematical calculation. Since the plots in figures 6.19, 6.20 and 6.21 show that the alignment of the detectors is correct the inclination in 6.18(b) originates from a remaining inaccuracy in the energy calibration.

The alignment has been checked for data taken with 2.40 GeV/c and 2.46 GeV/c deuteron beams on a deuteron cluster target as well as a polarized deuteron beam of 2.40 GeV/c momentum on a proton target. For all three data sets, which used the same geometrical setup of the telescope, the data analysis reproduced the kinematics of the reaction that has been used to check the alignment. With the used tracking telescope an angular resolution (FWHM) of 1.6° for protons and 2.2° for deuterons for the lowest particle momenta could be achieved. This essentially shows, that the presented track reconstruction method and the magnetic field correction work as expected. A full collection of alignment reference plots is presented in appendix A.

Figure 6.21: (a) θ_{Tel} vs. θ_{Fd} for dd-elastic at a beam momentum of 2.40 GeV/c. (b) $\Delta\phi$ of the two detected deuterons for the same reaction.

Chapter 7

Application

To show the capabilities of the silicon tracking telescope, the polarization observables A_y and A_{yy} for dp-elastic and pp and np-quasi elastic have been extracted from data taken during a test beam-time for Charge-Exchange experiments [61]. In the experiment a polarized deuteron 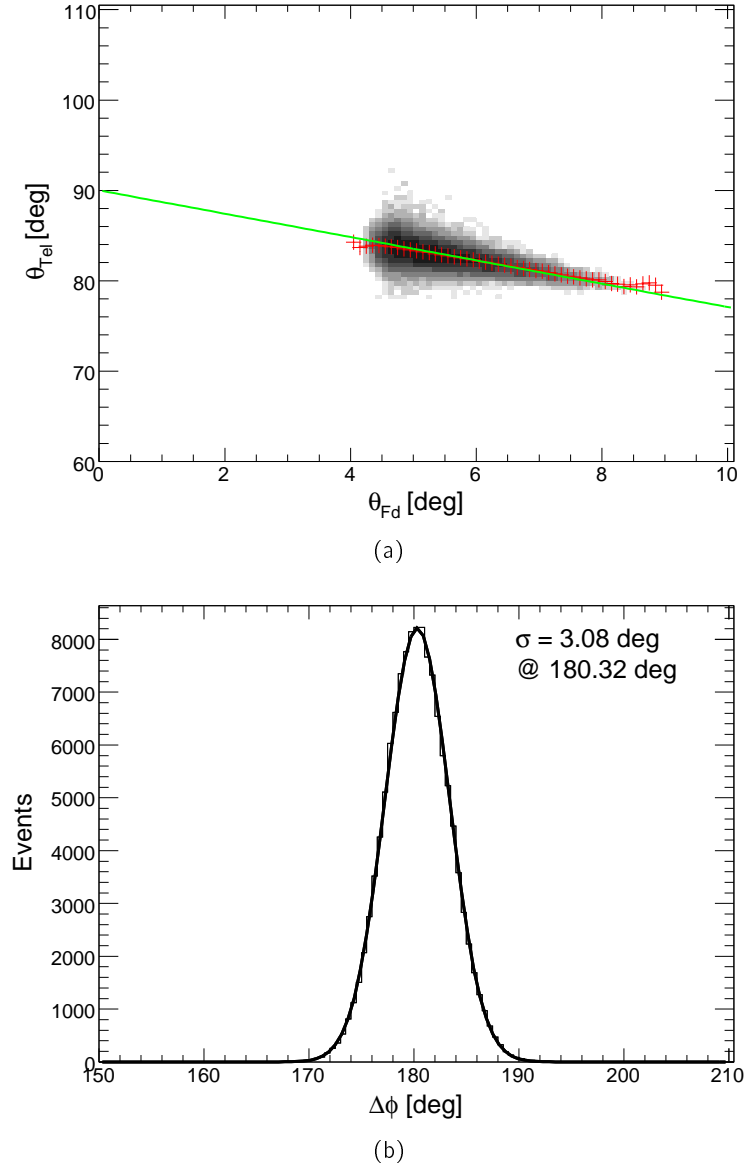beam of 2.40 GeV/c momentum with eight different polarization states impinged on an unpolarized hydrogen cluster jet target. Later in the chapter a first attempt to obtain a three-dimensional target image by fitting is presented.

For the analysis dedicated software has been developed around the Root-based [62] analysis framework RootSorter [63] which was also used in the tuning and commissioning phase of the tracking telescope.

7.1 Data Taking

A first test beam-time for the Charge-Exchange experiments with a polarized deuteron beam of 2.40 GeV/c momentum and an unpolarized hydrogen cluster jet target was exploited in November 2003. The presented data has been taken with the forward-coincidence trigger described in section 4.5. In the experiment eight different beam polarization states have been used. One unpolarized mixture and seven combinations of different vector and tensor polarizations. The states are summarized in table 7.1. At the end of each accelerator cycle, the polarized ion source was switched to the next polarization state. After the seventh state the source was reset and the polarization state set to the first spin mode. In order to allow the analysis of the different spin modes additional data-words that encoded the spin mode have been integrated into the data stream.

In the experiment the slow recoil proton from $\vec{dp} \rightarrow pd$, $\vec{dp} \rightarrow (pp)n_{Spectator}$ and $\vec{dp} \rightarrow (np)p_{Spectator}$ has been detected in the silicon tracking telescope, whereas the fast forward-going deuteron for $\vec{dp} \rightarrow pd$, the fast proton from $\vec{dp} \rightarrow (pp)n_{Spectator}$ and the spectator proton in $\vec{dp} \rightarrow (np)p_{Spectator}$ have been detected in the ANKE forward detector.

Spin Mode	Relative Intensity	Vector Polarization P_z		Tensor Polarization P_{zz}	
	$[I_0]$	ideal	EDDA	ideal	EDDA
0	1	0	0	0	0
1	1	$-2/3$	-0.499 ± 0.021	0	$+0.057 \pm 0.051$
2	1	$+1/3$	$+0.290 \pm 0.023$	$+1$	$+0.594 \pm 0.050$
3	1	$-1/3$	-0.248 ± 0.021	-1	-0.634 ± 0.051
4	2/3	$+1/2$	$+0.381 \pm 0.022$	$-1/2$	-0.282 ± 0.052
5	2/3	-1	-0.682 ± 0.022	$+1$	$+0.537 \pm 0.052$
6	2/3	$+1$	$+0.764 \pm 0.022$	$+1$	$+0.545 \pm 0.050$
7	2/3	$-1/2$	-0.349 ± 0.022	$-1/2$	-0.404 ± 0.053

Table 7.1: Vector and tensor polarizations measured by EDDA for the different spin modes used in the charge-exchange test beam-time. I_0 is the maximum number of deuterons stored in the COSY ring. In the experiment I_0 was in the order of $3 \cdot 10^9$ with spin modes 4 through 7 having 2/3 of that value.
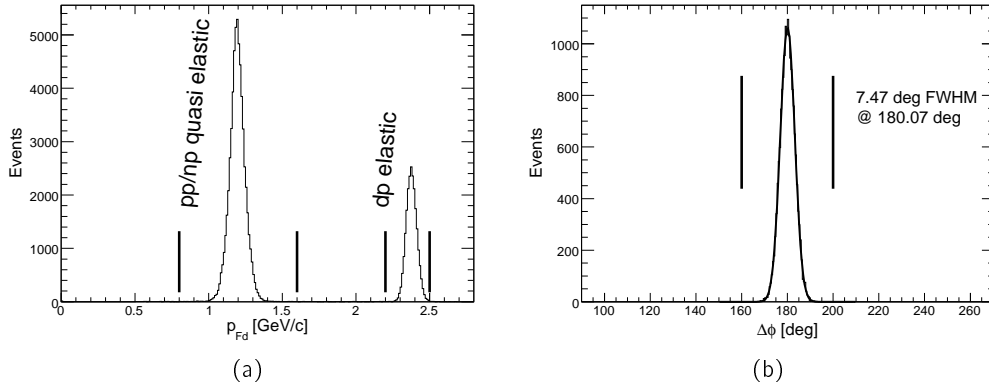

Figure 7.1: (a) Momentum distribution of forward-going particles for the data taken with the forward-spectator coincidence trigger. (b) Distribution of $\Delta\phi$ (the difference in ϕ angles for both particles) for $dp \rightarrow pd$.

7.2 Analyzing Powers from $\vec{\mathrm{d}}\mathrm{p} \to \mathrm{pd}$

Due to the limited ϕ acceptance of the ANKE forward detection system and the used tracking telescope for dp-elastic at this energy it was not possible to determine the beam polarization for each spin mode individually. With the knowledge of the beam vector and tensor polarizations obtained by simultaneous measurements by EDDA [24] it was, however, possible to extract the analyzing powers A_y and A_{yy} for $\vec{d}\mathrm{p} \to \mathrm{pd}$.

7.2.1 Event Selection

Figure 7.1(a) shows the momentum distribution of particles in the forward detection system for the forward-telescope coincidence trigger. A cut around the dp-elastic peak as well as a cut on the coplanarity, the difference in the ϕ angle of both detected particles, is enough to clearly identify the $dp \to pd$ elastic reaction channel with hardly any background events. The $\Delta\phi$ distribution for the identified $dp \to pd$ reaction channel together with the applied cut is shown in figure 7.1(b).

7.2.2 Determination of **A**$_y$ and **A**$_{yy}$

The differential cross section for polarized deuteron - proton scattering [64] can be expressed by

$$
\frac{d\sigma}{d\Omega}(\theta, \phi) = \frac{d\sigma_0}{d\Omega}(\theta) \left\{ 1 + \frac{3}{2} P_z A_y(\theta) \cos\phi \right.
$$
$$
\left. + \frac{1}{4} P_{zz} \left[A_{yy}(\theta)(1 + \cos 2\phi) + A_{xx}(\theta)(1 - \cos 2\phi) \right] \right\} \quad (7.1)
$$

in which $\frac{d\sigma_0}{d\Omega}(\theta)$ is the cross section for the unpolarized case, P_z and P_{zz} are the beam vector and tensor polarizations and A_y, A_{yy} and A_{xx} are the vector and tensor analyzing powers. Rewritten in terms of counts for certain beam polarization states equation 7.1 becomes

$$
N(\theta) = N_0(\theta) \left[1 + \beta_z P_z + \beta_{zz} P_{zz} \right] \quad (7.2)
$$

in which $N(\theta)$ are the counts for a certain spin-mode, $N_0(\theta)$ are the counts for the unpolarized beam and

$$
\beta_z = \frac{3}{2} A_y(\theta) \langle \cos\phi \rangle \quad \text{and} \quad (7.3a)
$$
$$
\beta_{zz} = \frac{1}{4} \left[A_{yy}(\theta)(1 + \langle \cos 2\phi \rangle) + A_{xx}(\theta)(1 - \langle \cos 2\phi \rangle) \right] \quad (7.3b)
$$

are asymmetries integrated over the full acceptance. To obtain these asymmetries from the experimental data, the number of identified dp elastic events for each spin-mode normalized to the number of events for the unpolarized beam (spin-mode 0) are plotted in a three-dimensional graph with the x and y axes being the beam vector (P_z) and tensor (P_{zz}) polarizations determined by EDDA. The plots are shown in figure 7.2. The counts for each accelerator spill have also been corrected using the COSY beam

(a) $15° < \theta_{cm} < 18°$ (b) $18° < \theta_{cm} < 21°$
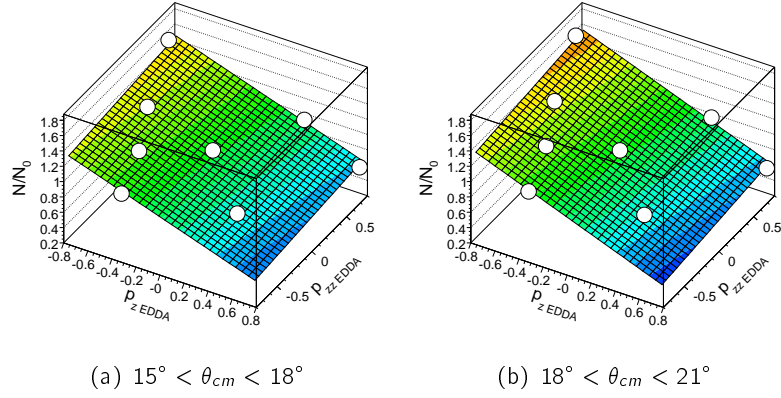
Figure 7.2: Counts of identified dp-elastic events for the eight available beam polarization states normalized to the counts for the unpolarized beam as a function of the beam polarizations p_z and p_{zz} measured by EDDA for the different θ_{cm} ranges of the forward-going deuteron. The data points are indicated by circles, the results of a fit by equation 7.2 to the data points are shown as planes in the plots and summarized in table 7.2.
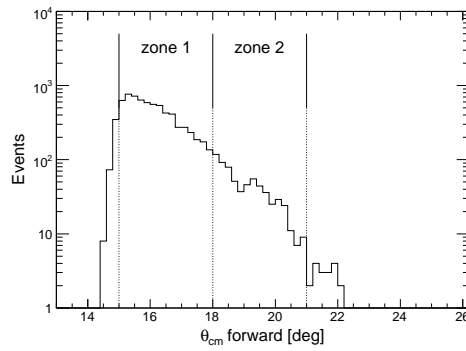
Figure 7.3: Distribution of the θ of the forward-going deuteron in the center of mass system.

zone	θ_{cm} [deg]	$\langle\theta_{cm}\rangle$ [deg]	N_0^*/N_0	β_z	β_{zz}
1	15 - 18	16.2	0.998	-0.527 ± 0.020	0.101 ± 0.021
2	18 - 21	19.0	1.007	-0.587 ± 0.025	0.119 ± 0.026

Table 7.2: Results of the fit of equation 7.2 to the three-dimensional asymmetry plots

zone	$\langle\theta_{cm}\rangle$ [deg]	$\langle\cos\phi_0\rangle$	$\langle\cos 2\phi_0\rangle$	A_y	A_{yy}
1	16.2	-0.991	0.965	0.354 ± 0.014	0.209 ± 0.044
2	19.0	-0.991	0.963	0.395 ± 0.017	0.248 ± 0.054

Table 7.3: Average of the cosine of the azimuthal angle and twice the azimuthal angle of the deuteron together with the results for the A_y and A_{yy} measurement for the two angular ranges.

current signal (BCT) which is a measure of the beam intensity, and the dead-time as described in section 4.6. In addition, the whole statistics have been subdivided into two ranges of θ_{cm} angles of the forward-going deuteron. Figure 7.3 shows the distribution of the θ angle of the deuteron in the center of mass system together with the two angular subdivisions. A fit by equation 7.2 yields the asymmetries β_z and β_{zz}. The fit results are indicated by planes in figure 7.2 and summarized in table 7.2 in which $\langle\theta_{cm}\rangle$ is the mean θ angle of the forward-going deuteron and N_0^*/N_0 is a fit offset.

With β_z obtained from the fit and the mean value of $\cos\phi$ of the forward going deuteron for spin-mode 0 it is possible to calculate A_y for each θ bin via equation 7.3a. The results for A_y are summarized in table 7.3 and shown in figure 7.4(a) together with experimental data points from Argonne [65, 66] and Saturne [67, 68]. At Argonne A_y and A_{yy} were investigated with a deuteron beam momentum of $p_d = 2.43\,\mathrm{GeV/c}$ for center of mass theta angles up to $61°$, whereas for A_{xx} the angular range went up to $84°$. The Saturne measurement, carried out at a deuteron beam momentum of $p_d = 2.435\,\mathrm{GeV/c}$, investigated A_y and A_{yy} in a θ_{cm} range from $32°$ to $94°$.

For the determination of A_{yy} the situation is more complicated because even at a small acceptance away from $\phi = 180°$ of the forward-going deuteron the influence of A_{xx} to the asymmetry has to be taken into account. To do so, equation 7.3b can be rewritten as

$$\beta_{zz} = \frac{A_{yy}(\theta)}{2 \cdot \mathcal{CF}} \tag{7.4}$$

with

$$\mathcal{CF} = 2 \cdot \frac{A_{yy}(\theta)}{A_{yy}(\theta) \cdot (1 + \langle\cos 2\phi_0\rangle) + A_{xx}(\theta) \cdot (1 - \langle\cos 2\phi_0\rangle)} \tag{7.5}$$

being a correction factor which is basically a ratio between A_{yy} and A_{xx} that can be estimated from the Argonne results. The Argonne results for A_{yy} and A_{xx} were ob-

(a)

(b)

(c)
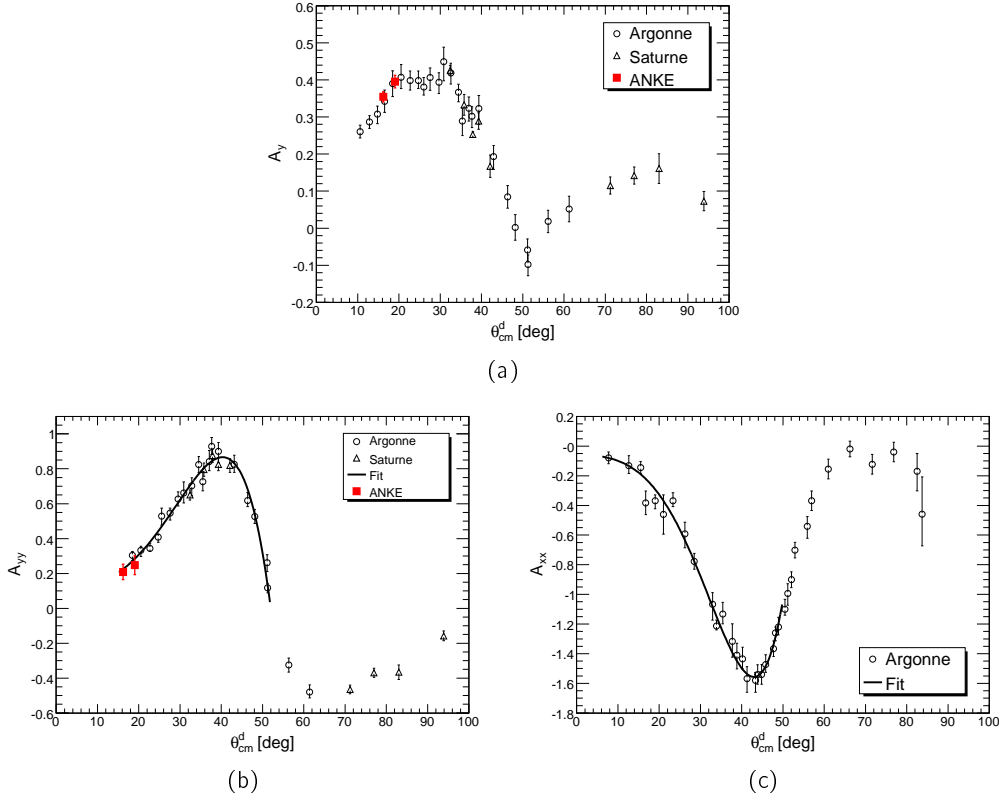
Figure 7.4: Experimental values for A_y (a), A_{yy} (b) and A_{xx} (c) from measurements at Argonne and Saturne. The results of the fits to the data points (equations 7.6) are drawn as solid lines.

tained from the same data set which means that the influence of the beam polarization on the ration cancels out. This feature essentially allows the use of the results from this independent measurement for the calculation of the correction factor. The results of the fits to the Argonne A_{yy} and A_{xx} data points [69, 70] (figures 7.4(b) and 7.4(c)) are shown in the following equations

$$A_{yy} = -50.51 + 178.6 \cos \theta_{cm} - 203.1 \cos^2 \theta_{cm} + 75.09 \cos^3 \theta_{cm} \qquad (7.6a)$$

$$A_{xx} = 77.19 - 282.7 \cos \theta_{cm} + 331.5 \cos^2 \theta_{cm} - 126.1 \cos^3 \theta_{cm} \qquad (7.6b)$$

With the use of the correction factor and the value for β_{zz} obtained by the fit to the three-dimensional asymmetry plots, the tensor analyzing power A_{yy} is obtained via equation 7.4. The results for A_{yy} are also summarized in table 7.3, the data points are plotted in figure 7.4(b).

Within the error bars the results for A_y and A_{yy} are compatible with the Argonne

zone	θ_{cm} [deg]	$\langle\theta_{cm}\rangle$ [deg]	A_y	A_{yy}
1	15 - 18	16.8	0.362 ± 0.008	0.212 ± 0.025
2	18 - 21	19.6	0.394 ± 0.012	0.289 ± 0.039
2	21 - 24	22.6	0.410 ± 0.011	0.337 ± 0.034

Table 7.4: Vector and tensor analyzing powers for the analysis without the use of the tracking telescope.

and Saturne data as well as with the results from an alternative analysis that did not make use of the tracking telescope data [69, 71]. The results of this analysis are summarized in table 7.4. The good agreement with the values of A_y and A_{yy} from the literature and the alternative analysis prove the capabilities of the tracking telescope.

7.3 Analyzing Powers for quasi-free pp and np scattering

The real advantage of the tracking telescope becomes obvious in the *pn* case in which a slow proton is detected in the tracking telescope and a second proton with half the beam momentum in the forward detector of ANKE. Here it is possible to determine the analyzing power A_y in *pp* and *np*-quasi elastic scattering via the reaction $\vec{d}p \rightarrow (pp)n_{\text{Spectator}}$ and $\vec{d}p \rightarrow (np)p_{\text{Spectator}}$ respectively. In the first reaction, both elastic reaction partners are directly measured in the ANKE detection system, while in the latter reaction the spectator proton is detected in the forward detection system. In both cases the four-momentum of the missing neutron is given by

$$n^\mu = d^\mu_{\text{Beam}} + p^\mu_{\text{Target}} - p^\mu_{\text{Telescope}} - p^\mu_{\text{Forward}} \tag{7.7}$$

in which $p^\mu_{\text{Telescope}}$ and p^μ_{Forward} are the four-momenta of the protons detected in the tracking telescope and the forward detector.

7.3.1 Identifying the reactions

The subset of the data is selected by a cut on the momentum of the forward-going proton as indicated in figure 7.1(a), and a narrow cut around the neutron mass in the missing mass distribution of the two detected protons. The missing mass of both protons together with the applied cut is shown in figure 7.5(a).

In case of pure quasi-elastic *pp* and *np* scattering no influence of the beam tensor polarization on the extracted analyzing powers should be seen. For low momentum transfer to the fast proton in the *pp* case and the neutron in the *np* case, a strong contribution from final state interaction however introduces this dependence. This is best seen from the results shown in table 7.5 in which, similar to the analysis for *dp* elastic, a fit by a plane with equation 7.2 has been made to the three-dimensional plot of the corrected counts for the eight different spin modes. The binning has however
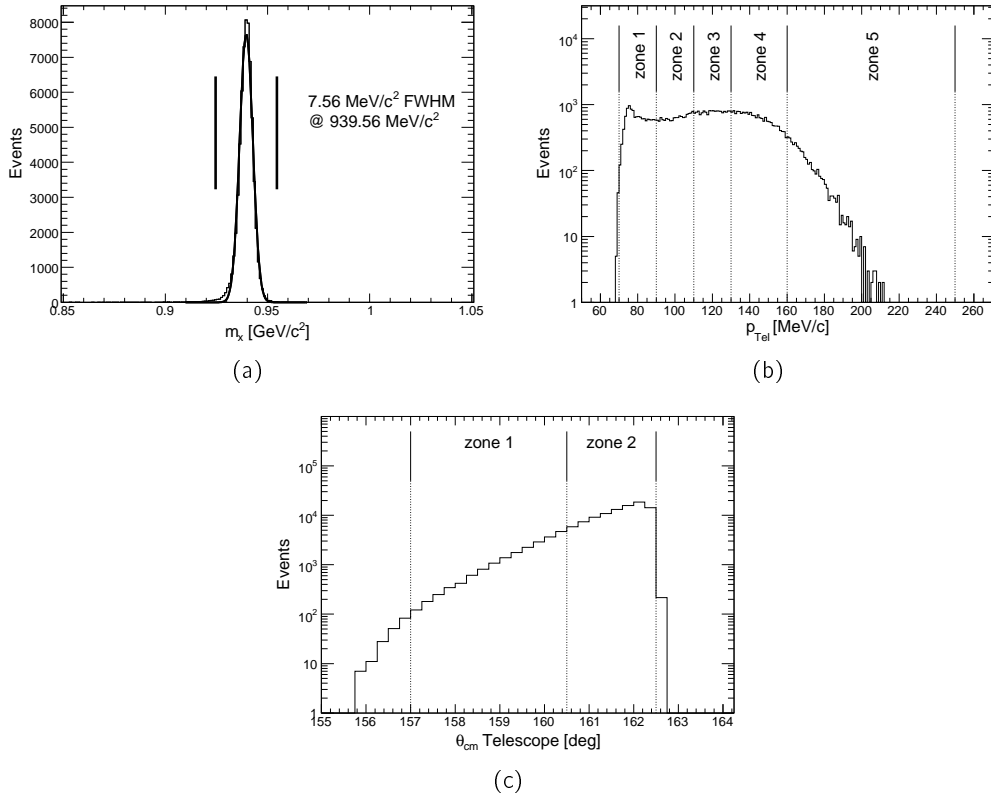
(a)

(b)

(c)

Figure 7.5: (a) Missing mass of the two detected protons. A peak at the neutron mass with hardly any background is visible. (b) Distribution of the momentum of the proton detected in the tracking telescope. (c) Distribution of the θ angle in the center of mass system for the proton detected in the telescope in which this proton has a momentum of $p_{Tel} > 160\,\text{MeV/c}$.

been done by the momentum of the proton detected in the tracking telescope, which is a direct measure of the momentum transfer. The distribution of momenta is shown in figure 7.5(b). In case of pure quasi-elastic pp or np scattering the fit parameter β_{zz}, which is sensitive to the influence of the beam tensor polarization, must be zero, the results in the table show however that β_{zz} is significantly different from zero for low momenta and develops towards zero with increasing momentum.

For larger momentum transfers, the influence of the final state interaction decreases, which also means that for the last momentum bin ($p_{Tel} > 160\,\text{MeV/c}$) the selected events are mostly due to pure pp and np quasi-elastic scattering. These events have been used to determine the analyzing power A_y for the combined and separated pp and np reaction channels.

zone	p_{Tel} [MeV/c]	β_z	β_{zz}
1	70 - 90	-0.093 ± 0.054	-0.200 ± 0.056
2	90 - 110	-0.159 ± 0.031	-0.154 ± 0.032
3	110 - 130	-0.199 ± 0.012	-0.098 ± 0.012
4	130 - 160	-0.241 ± 0.020	-0.067 ± 0.021
5	160 - 250	-0.269 ± 0.013	-0.030 ± 0.013

Table 7.5: Results of a fit of equation 7.2 to the three-dimensional plot of normalized counts for each spin-mode versus the P_z and P_{zz} measured by EDDA binned by the momentum transfer to the proton detected in the tracking telescope.

(a) $157° < \theta_{cm}^{p\,Tel} < 160.5°$ (b) $160.5° < \theta_{cm}^{p\,Tel} < 162.5°$
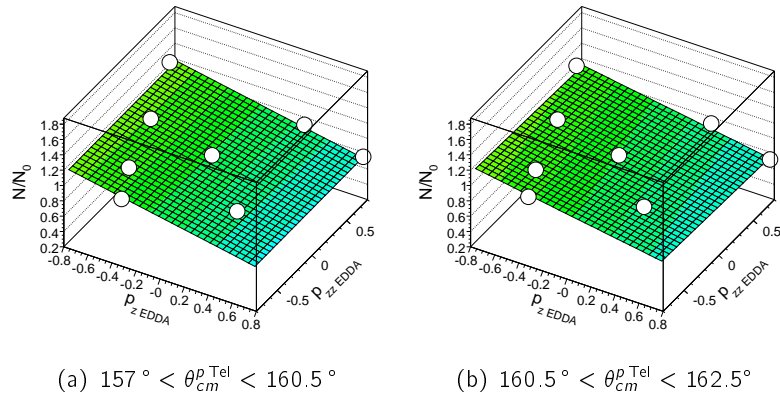
Figure 7.6: Counts for the combination of pp and np-quasi elastic for the eight available beam polarization states normalized to the counts for the unpolarized beam as a function of the beam polarizations p_z and p_{zz} measured by EDDA for the different θ_{cm} ranges of the proton detected in the telescope. The data points are indicated by circles, the results of a fit of equation 7.2 are shown as planes in the plots and summarized in table 7.6.

7.3.2 Determination of A_y

In both the pp and np case, the polarized differential cross-section is given by

$$\frac{d\sigma}{d\Omega}(\theta, \phi) = \frac{d\sigma_0}{d\Omega}(\theta) \left\{ 1 + P_z A_y(\theta) \cos \phi \right\} \tag{7.8}$$

In terms of counts equation 7.8 can again be written as

$$N(\theta) = N_0(\theta) \left[1 + \beta_z P_z \right] \quad \text{with} \quad \beta_z = A_y(\theta) \langle \cos \phi \rangle \tag{7.9}$$

in which β_z is the asymmetry with which the analyzing power A_y may be determined. Already without a separation into pp and np events the analyzing power may be determined for the combination of both reaction channels. To obtain the asymmetry $\beta_z^{pp/np}$

zone	θ_{cm} [deg]	$\langle\theta_{cm}\rangle$ [deg]	N_0^*/N_0	β_z	β_{zz}
1	157.0 - 160.5	159.6	0.977	-0.298 ± 0.032	0.007 ± 0.033
2	160.5 - 162.5	161.7	0.983	-0.260 ± 0.013	-0.040 ± 0.013

Table 7.6: Results of the fit of equation 7.2 to the two-dimensional asymmetry plots for the unseparated pp and np data ($p_{Tel} > 160\,\text{MeV/c}$).

zone	$\langle\theta_{cm}\rangle$ [deg]	$\langle\cos\phi_0\rangle$	A_y
1	159.6	0.979	-0.304 ± 0.033
2	161.7	0.978	-0.266 ± 0.013

Table 7.7: Vector analyzing power A_y for the combined pp and np data binned into angular ranges of θ_{cm} of the proton detected in the telescope ($p_{Tel} > 160\,\text{MeV/c}$).

the whole statistics has again been subdivided into ranges of the θ_{cm} angle of the proton detected in the tracking telescope and the normalized counts for each spin-mode plotted versus the beam polarizations measured by EDDA in a two-dimensional graph[1]. The distributions of θ angles in the center of mass system is shown in figure 7.5(c) together with the subdivisions. The two-dimensional graphs are shown in figure 7.6. A fit by equation 7.2 yields the asymmetries β_z and β_{zz} which are summarized in table 7.6.

From the fit results for β_z the analyzing power A_y can be calculated via equation 7.9. The results are summarized in table 7.7.

The only available possibility to separate both reaction channel to some extent from one another are the cuts indicated in figure 7.7 in which the correlation of θ_{Tel} to θ of the forward-going proton is shown. Figures 7.7(a) and (b) display the correlation for the results of a Geant4 simulation of $dp \rightarrow (pp)n_{\text{Spectator}}$ and $dp \rightarrow (np)p_{\text{Spectator}}$ respectively. A combination of both simulated reaction channels is displayed in figure 7.7(c), while the distribution for the real data is shown in figure 7.7(d).

For both pp and np, the difference of the ϕ angles of both ejectiles must peak at $\Delta\phi = 180°$. In pp $\Delta\phi$ is the difference of ϕ of both detected protons, while in np it is the difference of ϕ of the proton detected in the tracking telescope and the neutron. This behavior is shown in the histograms in figures 7.8(a) and (b). The data points indicate the real data, the histograms show the results from the Geant4 simulation. For both reaction channels the simulation reproduces the real data quite well. Moreover, with knowledge of the four-momentum vector of the spectator particle, in np this is just the forward-going proton, in the pp case it is the neutron, it is possible to reconstruct the Fermi momentum distribution. This is accomplished by a Lorentz transformation of this four-momentum into the rest frame of the beam deuteron via

---

[1]A one-dimensional graph is basically sufficient since there is no influence of P_{zz} on the asymmetry for the investigated reactions. In order to be sensitive on any residual effects from background reactions that depend on P_{zz} a two-dimensional graph has however been chosen.
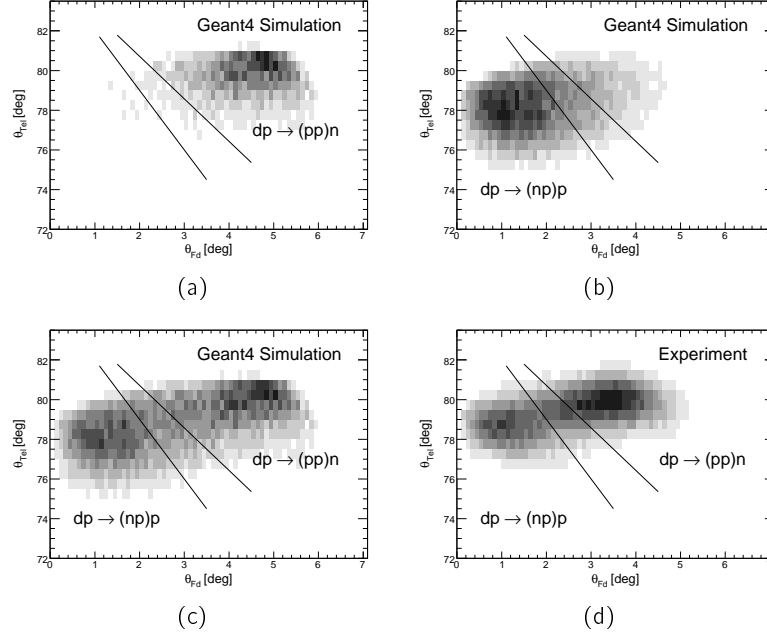
Figure 7.7: θ of the proton in the tracking telescope (θ_{Tel}) vs. θ of the proton in the forward detection system (θ_{Fd}) for (a) simulated pp events, (b) simulated np events, (c) both simulated pp and np and (d) the real data. In all cases the momentum of the proton in the telescope has been restricted to $p_{\mathrm{Tel}} > 160\,\mathrm{MeV}/c$.
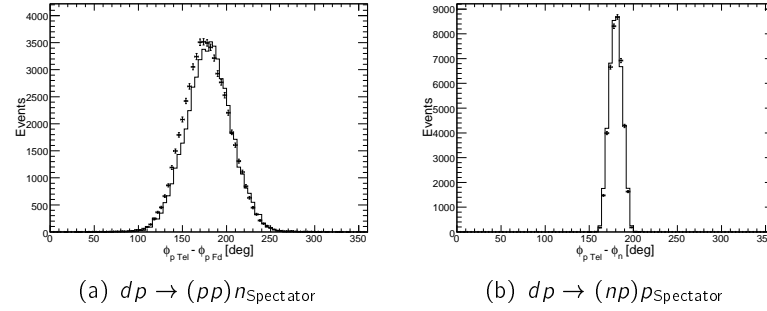

Figure 7.8: (a) Difference in ϕ ($\Delta\phi$) of the protons detected in the silicon tracking telescope and the forward detection system for the selected $dp \rightarrow (pp)n_{\mathrm{Spectator}}$ events. (b) Difference of ϕ_{Tel} to ϕ of the reconstructed neutron for the selected $dp \rightarrow (np)p_{\mathrm{Spectator}}$ events. In both plots the histogram represent the simulated data, the points the real data.

(a) $dp \rightarrow (pp)n_{Spectator}$

(b) $dp \rightarrow (np)p_{Spectator}$

(c) $dp \rightarrow (pp)n_{Spectator}$

(d) $dp \rightarrow (np)p_{Spectator}$
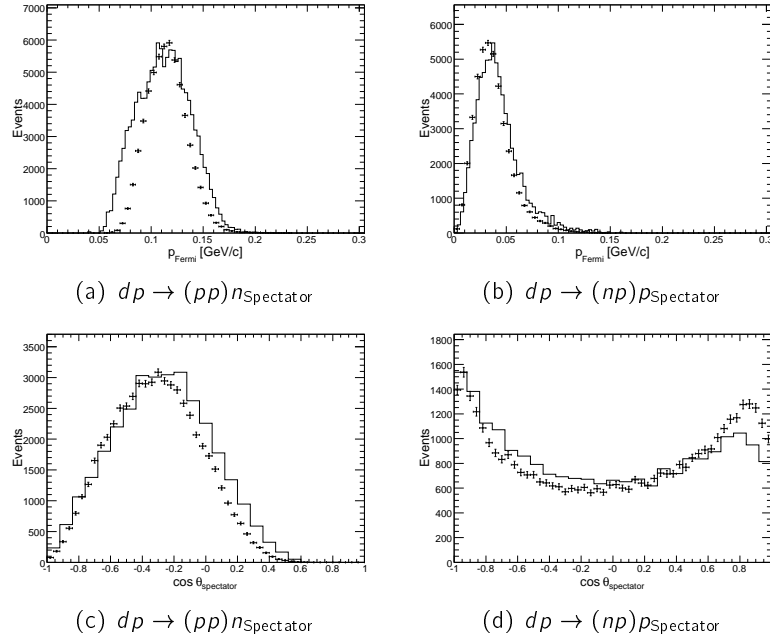
Figure 7.9: Fermi momentum distribution for (a) $dp \rightarrow (pp)n_{Spectator}$ and (b) $dp \rightarrow (np)p_{Spectator}$ (points) together with the results from the simulation indicated by histograms. Distribution of the cosine of the spectator particle in the rest frame of the beam deuteron for (c) $dp \rightarrow (pp)n_{Spectator}$ and (d) $dp \rightarrow (np)p_{Spectator}$ (points) together with the results from the simulation indicated by histograms.

$$
\begin{aligned}
p^x_{beam} &= p^x_{lab} \\
p^y_{beam} &= p^y_{lab} \\
p^z_{beam} &= (p^z_{lab} - E_{lab} \cdot \beta_{beam}) \cdot \gamma_{beam} \\
E_{beam} &= (E_{lab} - p^z_{lab} \cdot \beta_{beam}) \cdot \gamma_{beam}
\end{aligned}
\tag{7.10}
$$

in which p denote the spacial momentum components and E the energy of the spectator particle in the beam and lab frames. The momentum magnitude of the spectator particle after the transformation is then the intrinsic Fermi momentum of the constituent nucleons of the deuteron. The distributions together with the simulation results indicated by histograms, are shown in figures 7.9(a) and (b). Due to the limited acceptance, especially in the pp case, the distribution does however not look like the one shown in figure 1.2(a) of the introductory chapter. The distributions of $\cos\theta$ of the spectator particle in the beam rest frame are shown in figures 7.9(c) and (d), again the simulation reproduces the data quite well.

The good agreement of the simulation with the real data allows the use of the simulation to estimate the amount of background, that remains for the θ vs. θ cuts.

(a) $dp \rightarrow (pp)n_{\text{Spectator}}$ (b) $dp \rightarrow (np)p_{\text{Spectator}}$
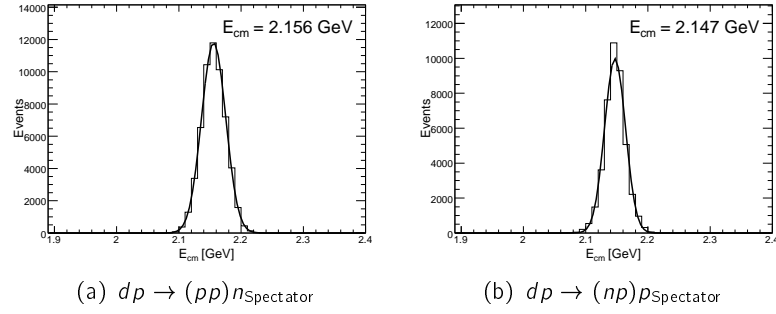
Figure 7.10: Center of mass energy for (a) $dp \rightarrow (pp)n_{\text{Spectator}}$ and (b) $dp \rightarrow (np)p_{\text{Spectator}}$.

zone	θ_{cm} [deg]	$\langle\theta_{cm}\rangle$ [deg]	N_0^*/N_0	β_z	β_{zz}
1	157.0 - 160.5	159.6	0.940	-0.385 ± 0.050	0.010 ± 0.051
2	160.5 - 162.5	161.7	0.984	-0.370 ± 0.018	-0.031 ± 0.018

(a) $dp \rightarrow (pp)n_{\text{Spectator}}$

zone	θ_{cm} [deg]	$\langle\theta_{cm}\rangle$ [deg]	N_0^*/N_0	β_z	β_{zz}
1	157.0 - 160.5	159.7	0.983	-0.199 ± 0.030	0.007 ± 0.031
2	160.5 - 162.5	161.7	0.977	-0.145 ± 0.015	-0.049 ± 0.016

(b) $dp \rightarrow (np)p_{\text{Spectator}}$

Table 7.8: Results of the fit of equation 7.2 to the two-dimensional asymmetry plots for the selected (a) pp and (b) np-quasi elastic events ($p_{Tel} > 160\,\text{MeV/c}$).

Taking the cross-sections for both reactions into account, at these angles the pp cross-section is about a factor of two higher than the np cross-section, about 32 % of the events selected with the pp cut actually arise from np-quasi elastic. This is already qualitatively seen from figure 7.7(b). For the selected np events the simulation shows 2 % background from $dp \rightarrow (pp)n_{Spectator}$.

Figure 7.9(c) displays that the direction of the spectator neutron in the pp case is going backwards with respect to the beam. In the spectator model this means that the beam proton is going into forward direction, which leads to a shift in the center of mass energy. Figures 7.10(a) and (b) show the center of mass energies for both selections calculated with equation 1.7. The center of mass energy in the pp case is roughly 10 MeV higher than in the np case due to the different momentum distributions of the spectator particle.

With the separated data the analyzing power A_y may be determined in the same way as with the full data sample. The plots in figure 7.11 display the normalized counts
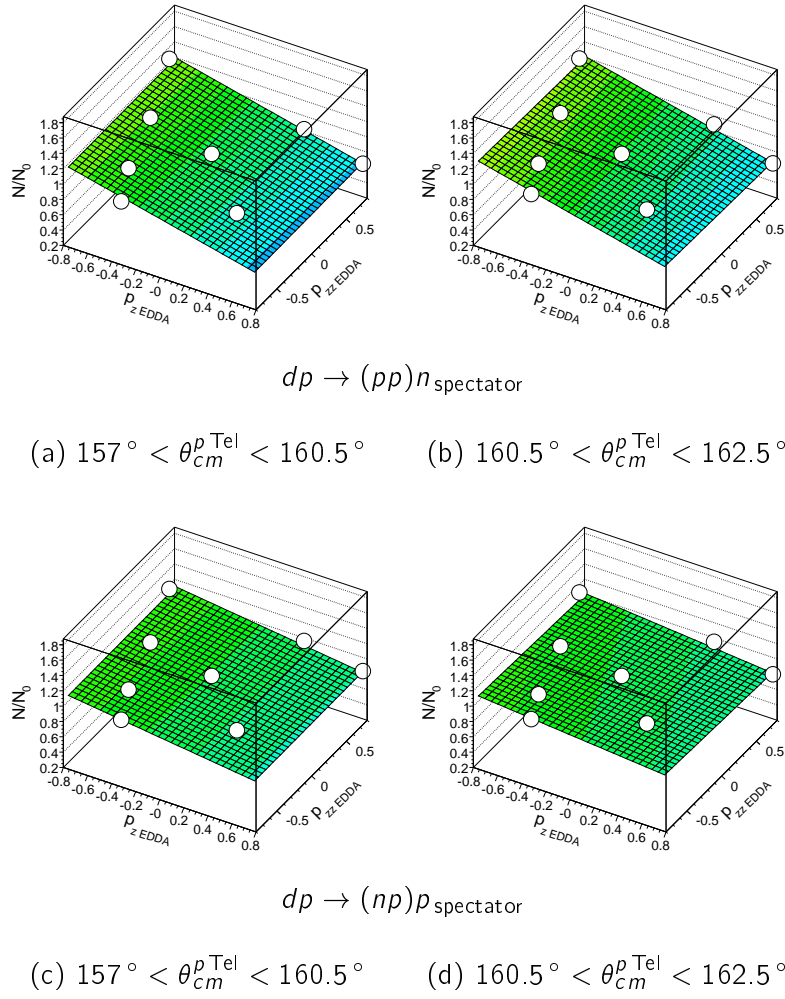
$$dp \rightarrow (pp)n_{\text{spectator}}$$

(a) $157° < \theta_{cm}^{p\,\text{Tel}} < 160.5°$ (b) $160.5° < \theta_{cm}^{p\,\text{Tel}} < 162.5°$

$$dp \rightarrow (np)p_{\text{spectator}}$$

(c) $157° < \theta_{cm}^{p\,\text{Tel}} < 160.5°$ (d) $160.5° < \theta_{cm}^{p\,\text{Tel}} < 162.5°$

Figure 7.11: Counts for *pp* and *np*-quasi elastic for the eight available beam polarization states normalized to the counts for the unpolarized beam as a function of the beam polarizations p_z and p_{zz} measured by EDDA for the different θ_{cm} ranges of the proton detected in the telescope. The data points are indicated by circles, the results of a fit of equation 7.2 to the points are shown as planes in the plots and summarized in table 7.8.
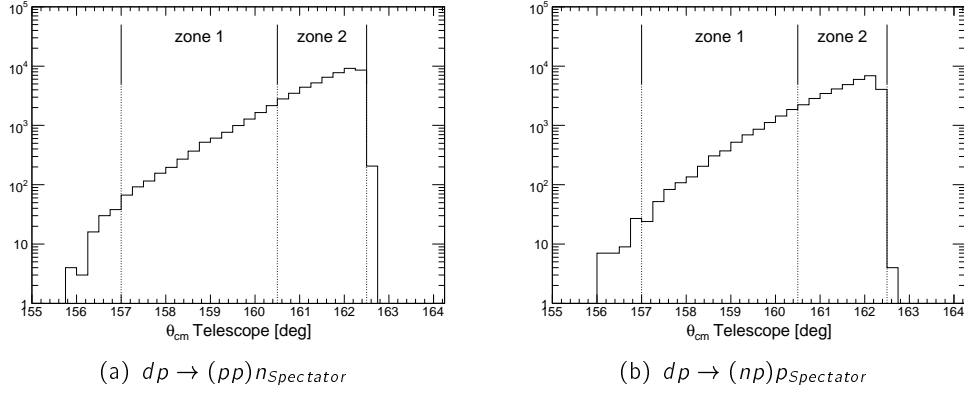
(a) $dp \rightarrow (pp)n_{Spectator}$

(b) $dp \rightarrow (np)p_{Spectator}$

Figure 7.12: Distribution of the θ angle in the center of mass system for the proton detected in the telescope for the selected (a) $dp \rightarrow (pp)n_{Spectator}$ and (b) $dp \rightarrow (np)p_{Spectator}$ events.

zone	$\langle\theta_{cm}\rangle$ [deg]	$\langle\cos\ \phi_0\rangle$	A_y
1	159.6	0.978	-0.393 ± 0.051
2	161.7	0.977	-0.379 ± 0.018

(a) $dp \rightarrow (pp)n_{\text{Spectator}}$

zone	$\langle\theta_{cm}\rangle$ [deg]	$\langle\cos\ \phi_0\rangle$	A_y
1	159.7	0.981	-0.203 ± 0.031
2	161.7	0.979	-0.148 ± 0.016

(b) $dp \rightarrow (np)p_{\text{Spectator}}$

Table 7.9: Vector analyzing power A_y for the selected (a) pp and (b) np-quasi elastic events binned into angular ranges of θ_{cm} of the proton detected in the telescope ($p_{Tel} >$ 160 MeV/c).
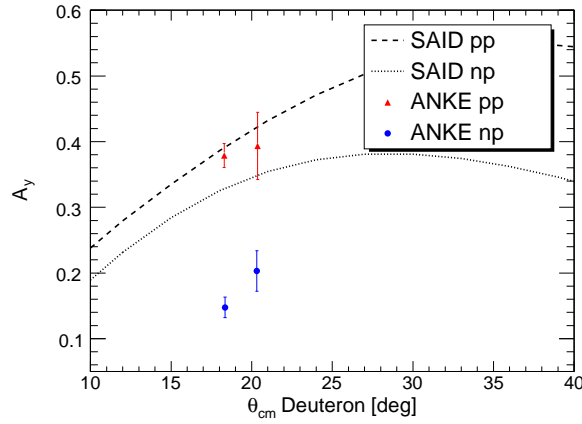
Figure 7.13: Experimental values for the analyzing power A_y for pp and np-quasi elastic. The lines in the plot represent the SAID prediction for pp and np-elastic scattering.

for the selected pp and np-quasi elastic events for two angular ranges of the proton detected in the telescope. The selected ranges indicated in figures 7.12(a) and (b) have been chosen to be the same as in the combined analysis. A fit by equation 7.9 to the data points yields the asymmetry β_z and the analyzing power A_y. A summary of the obtained fit coefficients is given in table 7.8. The results for A_y are summarized in table 7.9 and also shown in figure 7.13.

Although the np reaction channel seem to be identified quite well, the obtained A_y does not coincide with the SAID prediction whereas in the pp case, in which a strong influence of the miss-identified np events on the asymmetry is expected, the experimental data points are within the errors compatible with the SAID prediction. However, also here a shift to lower values for A_y is clearly seen in figure 7.13.

Up to this point, this feature has not been fully understood. Further investigations are therefore required in order to improve the separation of both reaction channels. Furthermore, the contribution of the miss-identified background on the asymmetry has to be analyzed in order to fully understand the presented results.

One potential reason for the effect seen in the results is the remaining disagreement between data and the simulation. As the simulation was used to determine the cuts to separate both reaction channels, it is clear that any disagreement might easily have an effect on the event selection. In addition, in the pp elastic case, the proton in forward direction is detected at the edge of the acceptance of the forward detection system where it is known that significant uncertainties in the momentum reconstruction may appear [72].
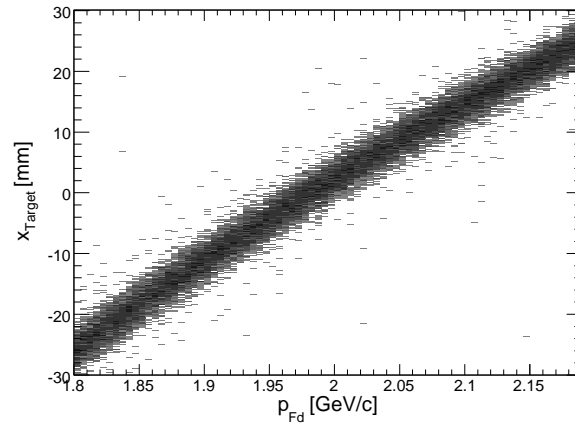
Figure 7.14: Possible Target x coordinates as a function of the particle momentum for fixed
hit positions in the forward wire chambers.

7.4   Reconstruction of a 3D Target Image

Even with only one particle in the tracking telescope it is possible, as shown in section 6.2.1, to reconstruct a two-dimensional target image. To obtain a 3D target image a second track, preferably in a second or the same tracking telescope, is necessary. The following will show the principle reconstruction method when this second track is in the forward detection system of ANKE.

A track in the forward detection system is described by its hits in the forward multi-wire proportional chambers and the hits in the scintillation counters. In the standard momentum reconstruction a particle is tracked through the D2 magnetic field by minimizing the distance of the track to the hits in the wire chambers with the origin of the track being the nominal target point and the free parameters of the minimization being the three-momentum of the particle (p, $\theta_{horizontal}$ and $\theta_{vertical}$. For the reconstruction of the x coordinate of the vertex on an event by event basis a fourth minimization parameter which specifies the origin of the track has to be introduced. The origin of the track is a point on the track of the particle in the tracking telescope but with a variable x coordinate.

Since the wire chambers of the forward detection system are located outside the field of the D2 spectrometer magnet the tracks described by the hits in the chambers are basically straight lines. Figure 7.14 shows the possible x coordinates of the start point of the track versus the particle momentum for fixed hit positions in the wire chambers. The data for this plot have been simulated by sending particles with different momenta from behind the third forward multi-wire proportional chamber through the inverted magnetic field of D2 back to the target region. The plot shows a strong correlation between the momentum and the x coordinate of the origin even though the track parameters from the analysis point of view are identical (hit positions). This means that a minimization with all four parameters is not possible.
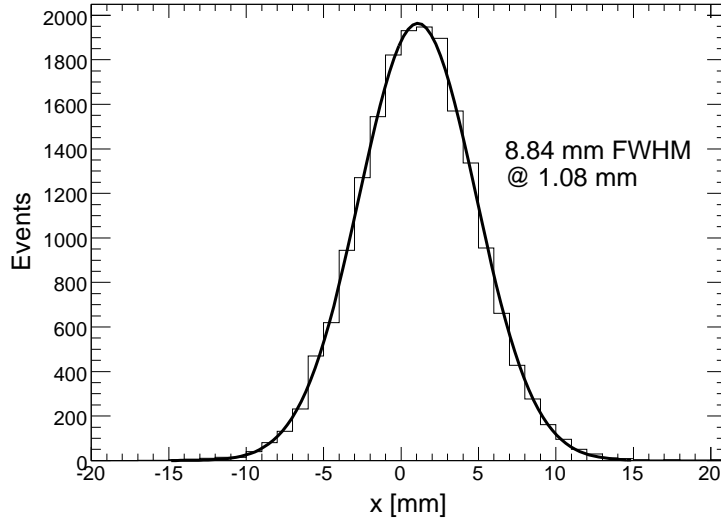
Figure 7.15: Distribution of vertex x coordinates after intersecting the track in the tracking telescope with the track in the forward detection system.

With the knowledge of the four-momentum of the particle detected in the tracking telescope and the reaction kinematics it is however possible to fix the magnitude of the momentum of the forward-going particle. For the available data the possible reactions are the elastic reactions $dp \rightarrow pd$ and $dd \rightarrow dd$ for which the momentum of the particle in the forward detector can be expressed by

$$E_{cm} = \sqrt{m_{\text{beam}}^2 + m_{\text{target}}^2 + 2 \cdot E_{\text{beam}} \cdot m_{\text{target}}}$$
$$\beta_{cm} = \frac{p_{\text{beam}}}{E_{\text{beam}} \cdot m_{\text{target}}}$$
$$\gamma_{cm} = \frac{1}{1 - \beta_{cm}^2} \tag{7.11}$$
$$p_{\text{Fd}} = \sqrt{(\gamma_{cm} \cdot E_{cm} - E_{\text{Tel}})^2 - m_{\text{Fd}}^2}$$

in which p_{Fd} is the momentum of the forward-going particle and E_{Tel} is the Energy of the particle detected in the tracking telescope. With the momentum of the forward-going particle being fixed by kinematical constraints the number of free parameters is reduced to three (x, θ_{Fd} and ϕ_{Fd}) which allows one to perform the minimization. The result of the minimization is shown in figure 7.15 which displays the vertex x coordinate distribution for the $dp \rightarrow pd$ elastic scattering.

As shown previously in section 6.2.1 on page 63, the target extension in y and z determined by the tracking telescope alone is in the order of 6.3 mm in y and 6.5 mm in z (both FWHM) with a resolution of approximately 1 mm. With the assumption

that the distribution of vertexes in the x coordinate is in the same order as for y and z one can conclude that the resolution in x is much worse and is of the order of 9 mm. With this result it is apparent, that the vertex resolution with just one track in the tracking telescope is not sufficient to unambiguously distinguish between beam hits on the actual target gas from hits on the storage cell wall when working with the polarized internal target at ANKE.

An increased coverage of the target cell by additional tracking telescopes and thus at least two tracks in the telescopes will make it possible to overcome this problem.

Chapter 8

Conclusions and Improvements

It had been planned to use two fully equipped telescopes for the measurement of $pn \rightarrow d\omega$ during a beam-time in August 2003. Due to an incident with a vacuum break, the bond connections to one $69\,\mu$m detector, both $300\,\mu$m detectors and one Si(Li) were, however, destroyed prior to the measurements which made the existing setup useless. Only due to the modular design of the setup it has been possible to configure one of the telescopes with the remaining two detectors prior to the next scheduled beam-time in November 2003. The alignment plots based on the available data demonstrate the good performance of the tracking telescope even though it has not been used in its optimal configuration.

Nevertheless, there is room for improvements, especially in the energy measurement and the read-out performance.

8.1 Energy Calibration

The procedure to obtain the energy calibration for each individual segment, detector side and the whole telescope has been primarily based on the test-pulse calibration with additional adjustments by fitting real data to the expected values. Due to the absence of an absolute energy reference, the quality of the calibration can only be given by the distance between the proton and deuteron bands. For the calibration obtained by the fitting method it was only in the order of 6 %. With the used telescope and this calibration, a proton-deuteron separation of $3.8\,\sigma$ could still be achieved.

In the future it is therefore desirable to have at least one energy reference point in order to obtain an absolute calibration with just a test-pulse measurement, that basically determines the non-linearity of the preamplifier, and then scaling to that reference energy. In practice such an energy reference point could be given by irradiating each detector with a mono-energetic α-source with known energy. When working with an α-source, the dead-layers have to, however, be taken into account. Moreover, the proposed procedure will be significantly faster than the method described in this work, which would also allow to monitor the stability of the calibration during data taking at COSY by permanently placing α-sources at the telescopes.

8.2   Tracking

The data presented in this work has solely been taken with a telescope equipped with just one thin silicon and one thick Si(Li) detector. Even without the intermediate tracking layer it was possible to reconstruct three-dimensional hit position information from that last detection layer. Moreover, the kinematics of all reactions that have been used to check the alignment of the setup could be reproduced by the analysis. This shows that the presented track reconstruction method and the magnetic field corrections work as expected. The achieved angular resolution for the lowest detected momenta was in the order of $1.6°$ for protons and $2.2°$ for deuterons.

With the poor position resolution of the thick detector, it is evident that the tracking performance can only be improved by an intermediate detection layer of $300\,\mu$m or $500\,\mu$m thickness with the same pitch as the first detector. With a total of three detectors, the track reconstruction will rely only on the position information of the hits in the first two detectors and use the third layer only to check the validity of the track and determine the efficiency of the telescope. It will then be possible to increase the pitch of the third layer to about $2\,$mm which will also improve the error in the energy loss determination because the number of segments that collect the generated charge is decreased.

8.3   Read-Out Performance

With zero suppression, the time needed to read out on event is in the order of $160\,\mu$s while it is $360\,\mu$s when the DAQ is running without data reduction. These numbers are for the telescope equipped with two detectors and will increase for a fully equipped telescope and once several telescope will become available for data taking. At the moment, the slowest other sub-system at ANKE requires approximately $150\,\mu$s to handle one event. It should therefore be the goal to increase the read-out performance of the tracking telescope DAQ system or keep it at least at the current value of $160\,\mu$s even when increasing the number of channels.

To achieve this, a dedicated read-out system is under development at the Central Institute for Electronics (ZEL) of the research center which will be compatible with the developed in-vacuum front-end electronics. One unit of this new electronics will handle both sides of one detector by a flat-cable connection to both interface boards on the flange. In addition, each unit will be equipped with two ADC, one for each detector side, and two Xilinx Spartan-II [73] field programmable gate arrays (FPGA) that replaces the VPG517 control unit of the existing DAQ and allow an individual per side read-out sequence. Furthermore, the use of the FPGA will give the opportunity to implement one of the presented common-mode correction methods and the zero suppression already on hardware level.

8.4   Time of Flight Measurement

To distinguish between protons and deuterons detected in the forward detection system by the time of flight method the time resolution of 10 ns of the VA32TA2 chip is not sufficient. At a beam momentum of for instance 3 GeV/c the time of flight difference between protons and deuterons is only 3 ns. Currently a different front-end chip with significantly better time resolution is under investigation at the IKP that could be used as an alternative for the VA32TA. The MATE3 [74] front-end chip has been developed at the CEA Saclay and the University of Orsay for the MUST2 [75] detection system. For the investigation a second in-vacuum front-end board similar to the on developed for the VA32TA2 chip has been designed. It is compatible with the existing interface board which allows the integration of the MATE3 chip into the DAQ.

Although the MATE3 chip has also a better energy resolution, it is not a replacement for the VA32TA2 because it has a significantly higher threshold. It is planned to equip one side of the first two detection layers (300 μm and 300/500 μm) with the MATE3 chip for good time resolution and the other side with the VA32TA2 for low trigger thresholds. This way it will be possible to precisely measure the energy loss, have a low trigger threshold and be able to use the time information from the silicon telescope in combination with the time information from other ANKE detection systems to perform a particle identification via the time-of-flight method.

The latest results from these investigations look already promising. It could be shown that the time resolution is below 1 ns (FWHM) for energy deposits of $\geq$ 1.2 MeV which results in a time of flight separation of protons and deuterons detected in the ANKE forward detector of approximately 7 σ.

Chapter 9

Outlook

The results and data presented in this work have shown that the developed detection system, consisting of the telescope itself, the dedicated front-end electronics and the data acquisition, together with the developed software algorithms are powerful tools for the future physics program at ANKE.

For a final check of the calibration procedure, a beam-time is under preparation at the Tandem accelerator of the University of Cologne. It is planned to directly irradiate one telescope at fixed angles with low intensity proton and deuteron beams of well defined energy provided by the accelerator. Besides the benefit of an absolute energy calibration this method will also allow the measurement of the thicknesses of the dead layers of each detector and a first determination of the efficiency.

A first set of $300\,\mu$m thick detectors has been delivered by Micron and we are waiting for the ordered $69\,\mu$m and $500\,\mu$m detectors. The serial production and laboratory tests of the front-end electronics for these detectors is under way. The unsuccessful beam-time for the measurement of $pn \rightarrow d\omega$ in August of 2003 will be repeated with two telescopes equipped with these new detectors in the second half of 2006. The telescopes will then also contain most of the proposed improvements. For this experiment three weeks of beam-time at COSY will be needed.

In 2007, when the final check of the front-end and read-out electronics is completed, ANKE will be extended with eight tracking telescopes placed around the storage cell. This will ultimately mark the start of the double polarized proton neutron physics program at ANKE.

Appendix A

Alignment Reference Plots

The following is a collection of alignment reference plots obtained from data taken during the beam-times in November 2003 with polarized and unpolarized deuteron beams on proton and deuterium targets. In all cases the same geometrical setup of the tracking telescope has been used.

Each section starts with reaction independent alignment plots which are the reconstructed target positions versus the track angles (y_{target} vs. ϕ, z_{target} vs. ϕ, y_{target} vs. θ and z_{target} vs. θ) and the θ - ϕ correlation. All plots are selected in such a way that the value plotted on the ordinate must be independent on the value drawn on the abscissa. Each plot also includes the inclination of the displayed band. Were applicable the plots are divided in different momentum ranges.

For completeness each section also contains the alignment plots for the corresponding elastic reaction. In case of the proton target this is $dp \rightarrow pd$, for the deuteron target it is $dd \rightarrow dd$. The plots are the difference between the ϕ angles of both particles ($\Delta\phi$), θ_{Tel} vs. θ_{Fd}, θ_{Tel} vs. p_{Tel} and θ_{Fd} vs. p_{Tel}. The later two plots strongly depend on the correctness of the energy calibration.
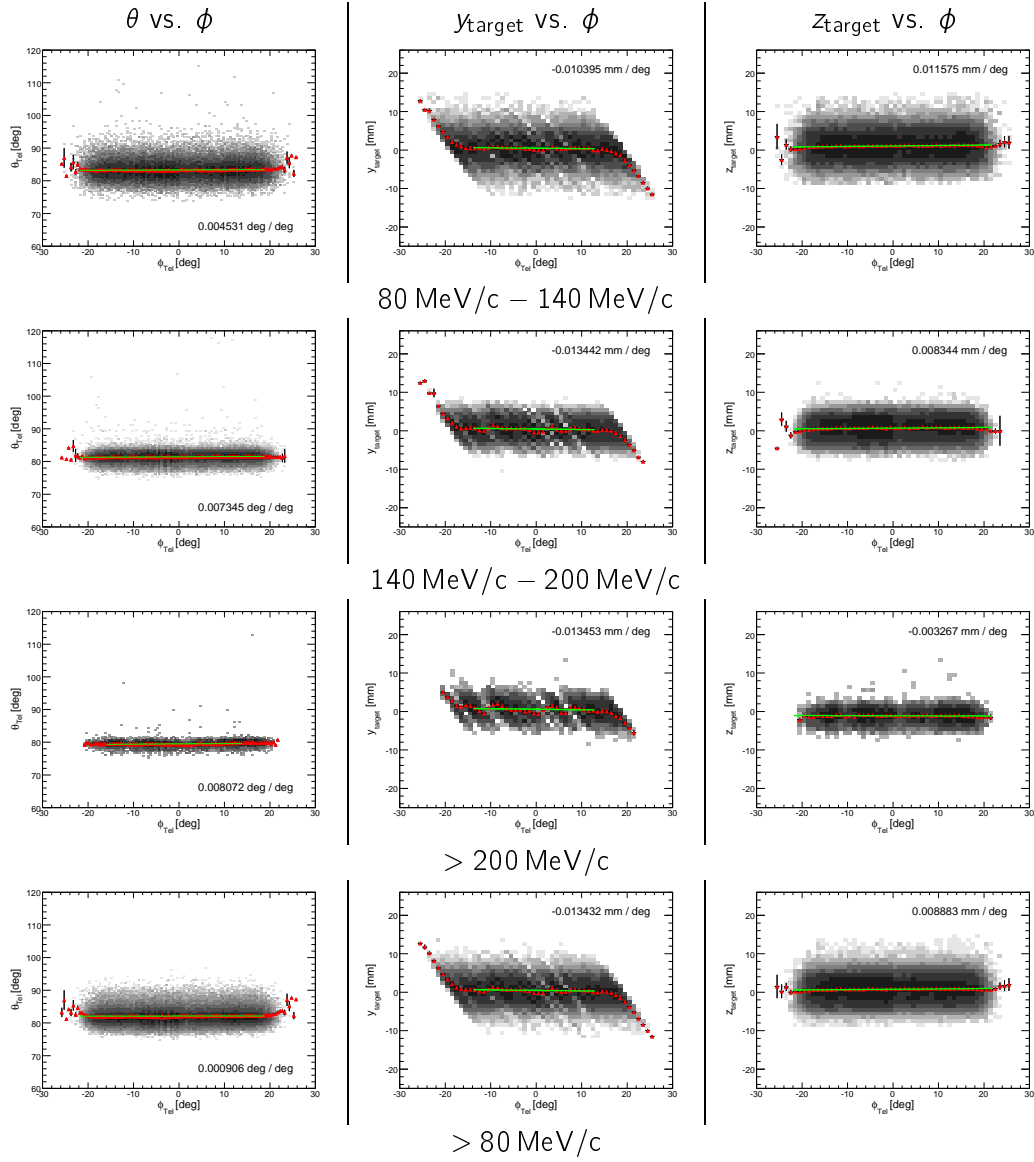
dp-Elastic at $2.40\,\mathrm{GeV/c}$

Figure A.1: θ vs. ϕ, y_{target} vs. ϕ and z_{target} vs. ϕ for protons split into different momentum ranges.
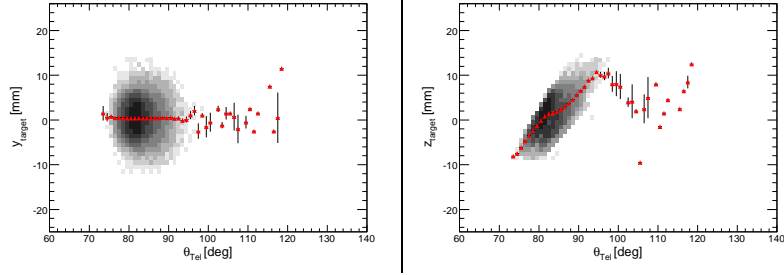
Figure A.2: y_{target} vs. θ and z_{target} vs. θ for protons. Due to the limited range of θ angles it is not meaningful to split the plots in different momentum ranges. In case of z_{target} vs. θ also the cut originating from the acceptance of the telescope is visible. Under no θ angle of the detected proton the full target (in z direction) is visible.
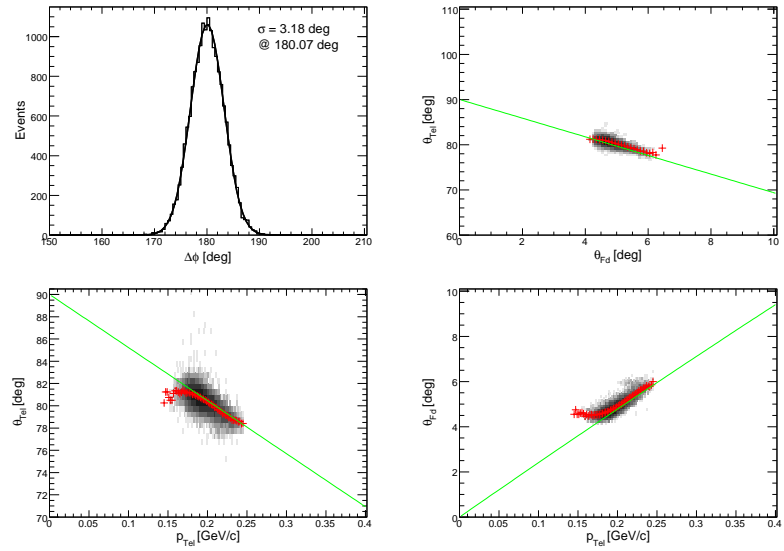

Figure A.3: Alignment plots for $dp \rightarrow pd$. The lower two plots strongly depend on the correctness of the energy calibration.
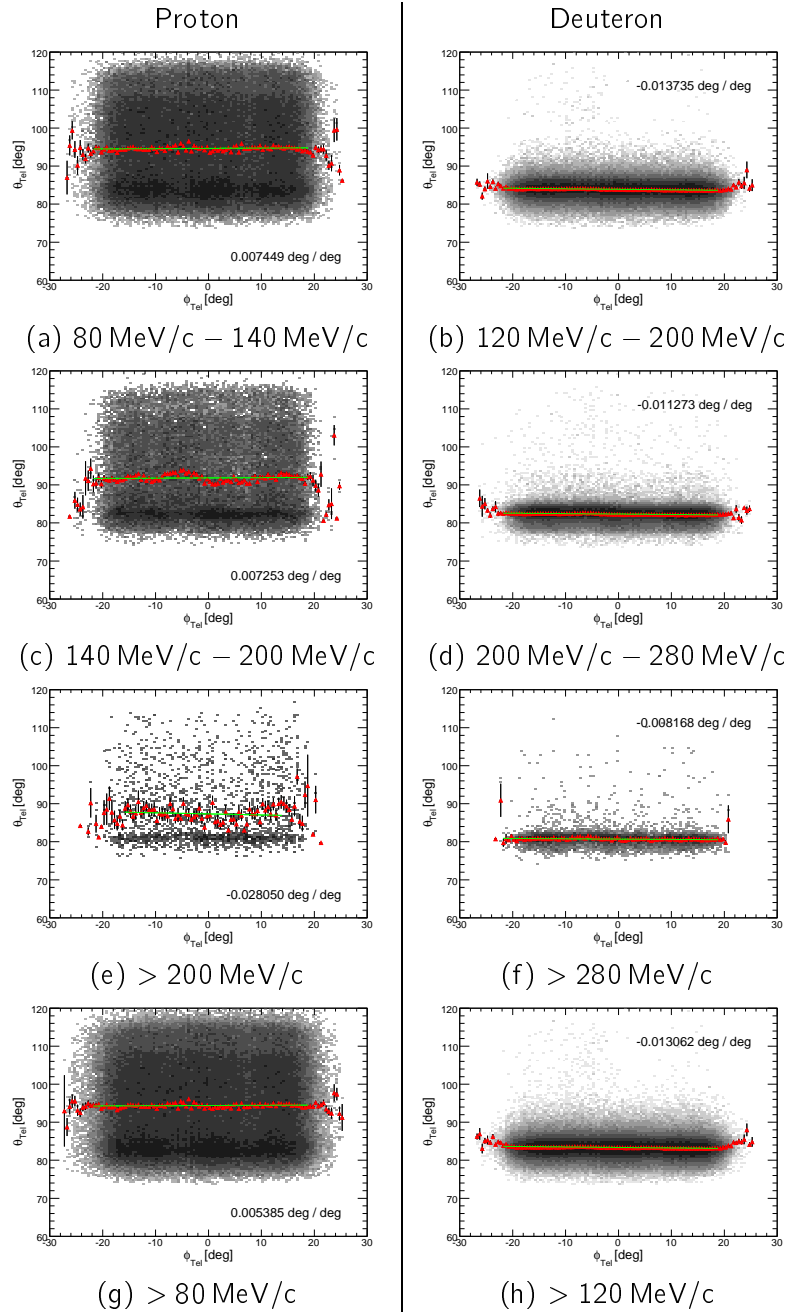
dd-Elastic at 2.40 GeV/c

Proton

Deuteron

(a) 80 MeV/c − 140 MeV/c

(b) 120 MeV/c − 200 MeV/c

(c) 140 MeV/c − 200 MeV/c

(d) 200 MeV/c − 280 MeV/c

(e) > 200 MeV/c

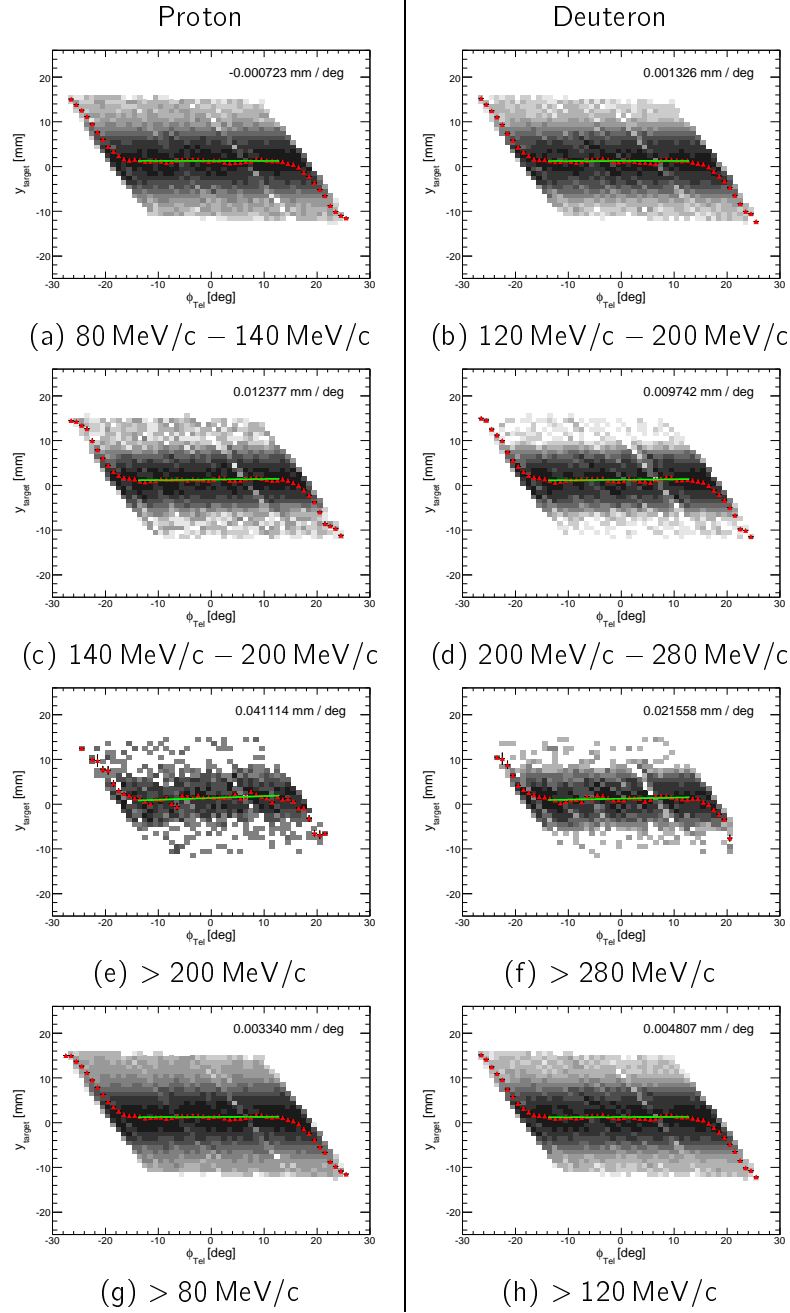(f) > 280 MeV/c

(g) > 80 MeV/c

(h) > 120 MeV/c

Figure A.4: θ vs. ϕ for both protons and deuterons separated in different momentum ranges.

Figure A.5: y_{target} vs. ϕ for both protons and deuterons separated in different momentum ranges.
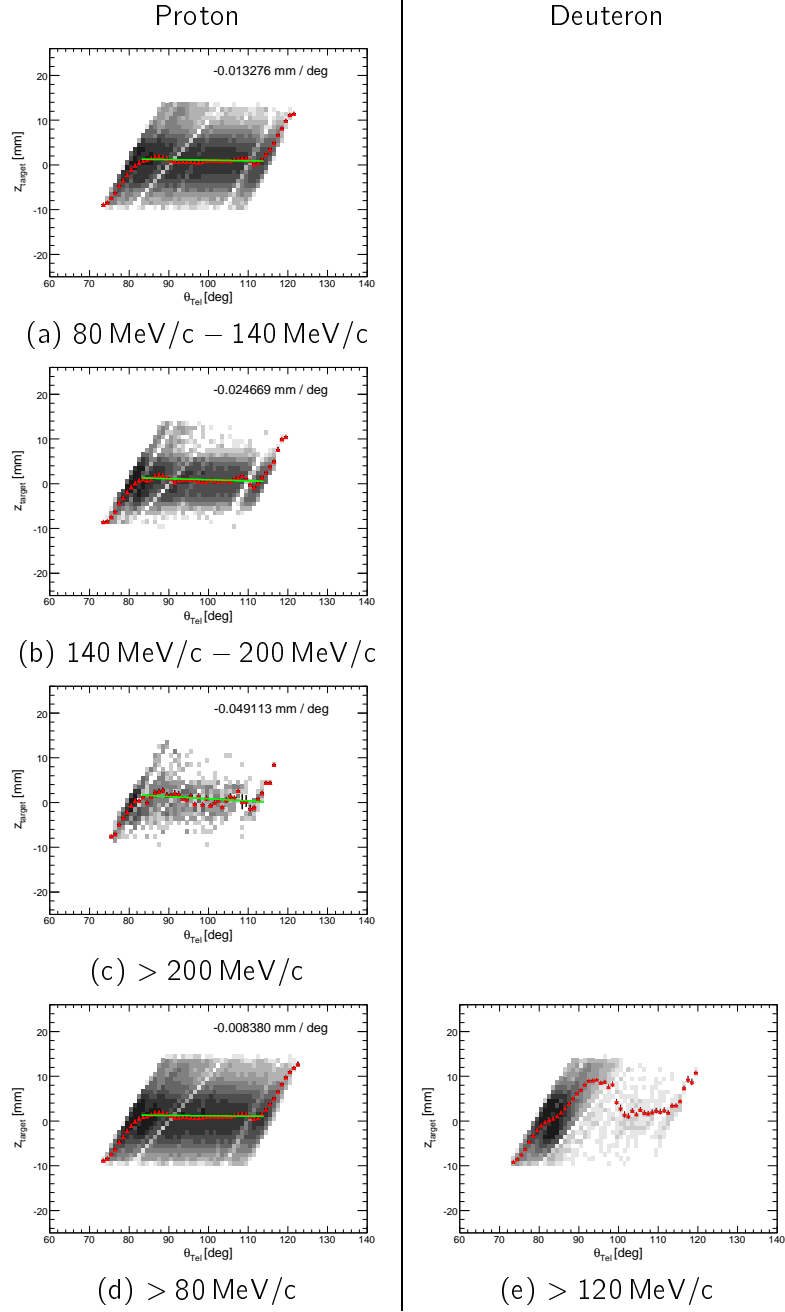
Proton   Deuteron

(a) $80\,\mathrm{MeV/c} - 140\,\mathrm{MeV/c}$

(b) $140\,\mathrm{MeV/c} - 200\,\mathrm{MeV/c}$

(c) $> 200\,\mathrm{MeV/c}$

(d) $> 80\,\mathrm{MeV/c}$

(e) $> 120\,\mathrm{MeV/c}$

Figure A.6: z_{target} vs. θ for both protons and deuterons. For deuterons which are only detected in a very limited θ range the plots are not split into different momentum ranges. In all plots the cut due to the limited acceptance is visible.
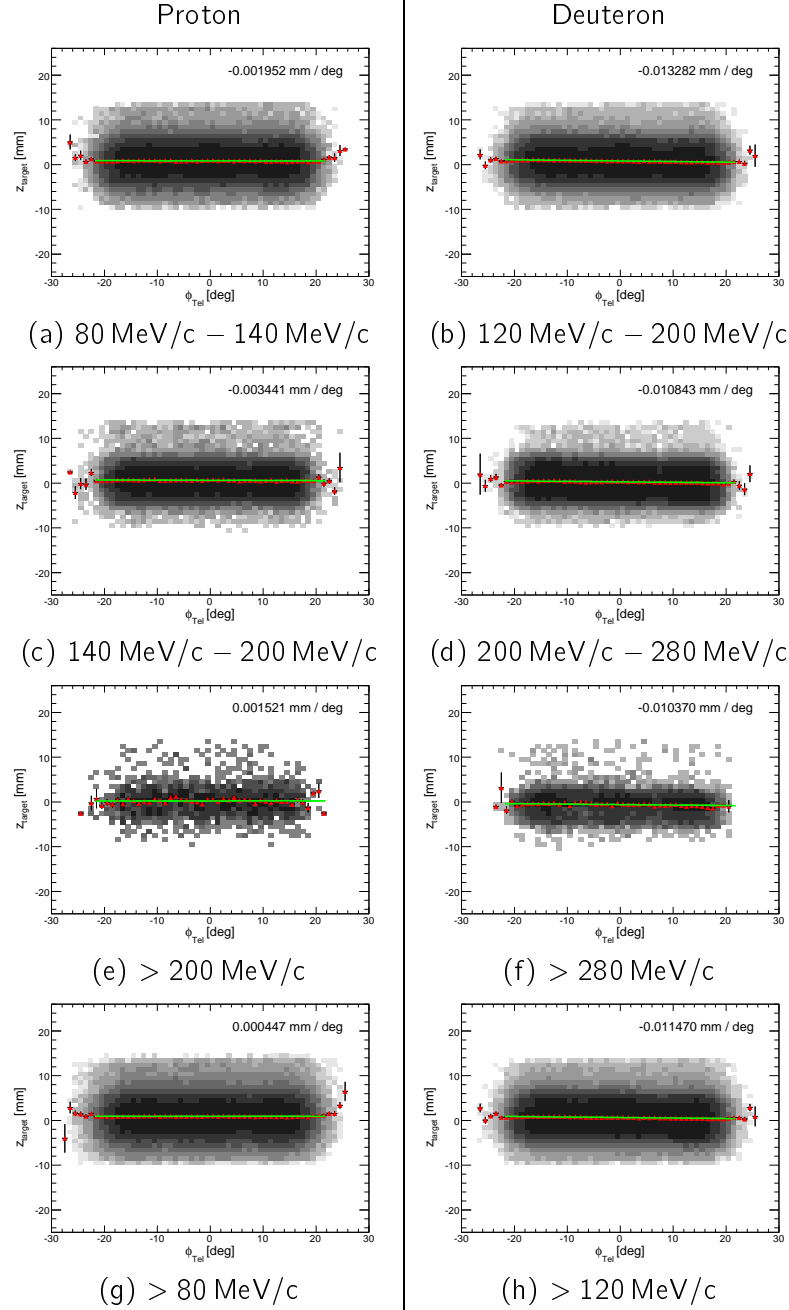
Figure A.7: z_{target} vs. ϕ for protons and deuterons split into different momentum ranges.
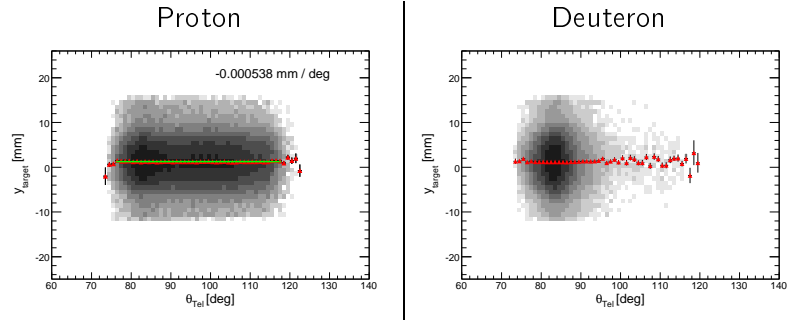
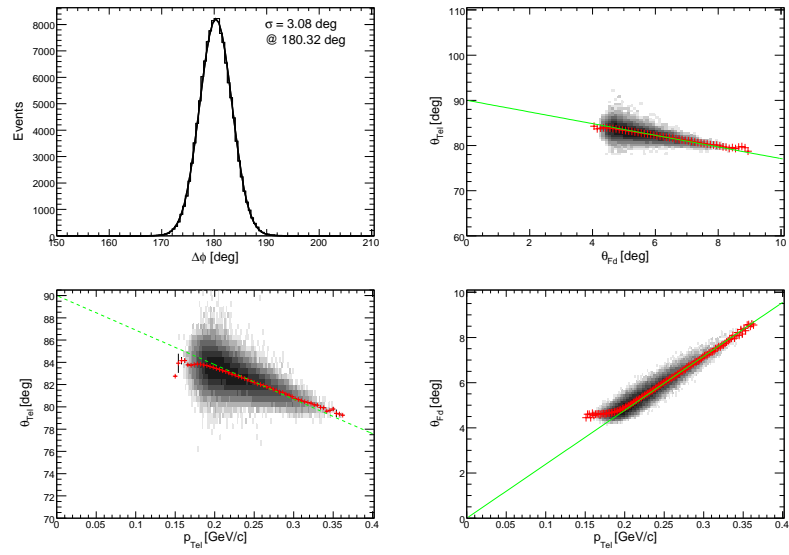Figure A.8: y_{target} vs. θ for protons and deuterons.

Figure A.9: Alignment plots for dd-elastic at 2.40 GeV/c beam momentum.
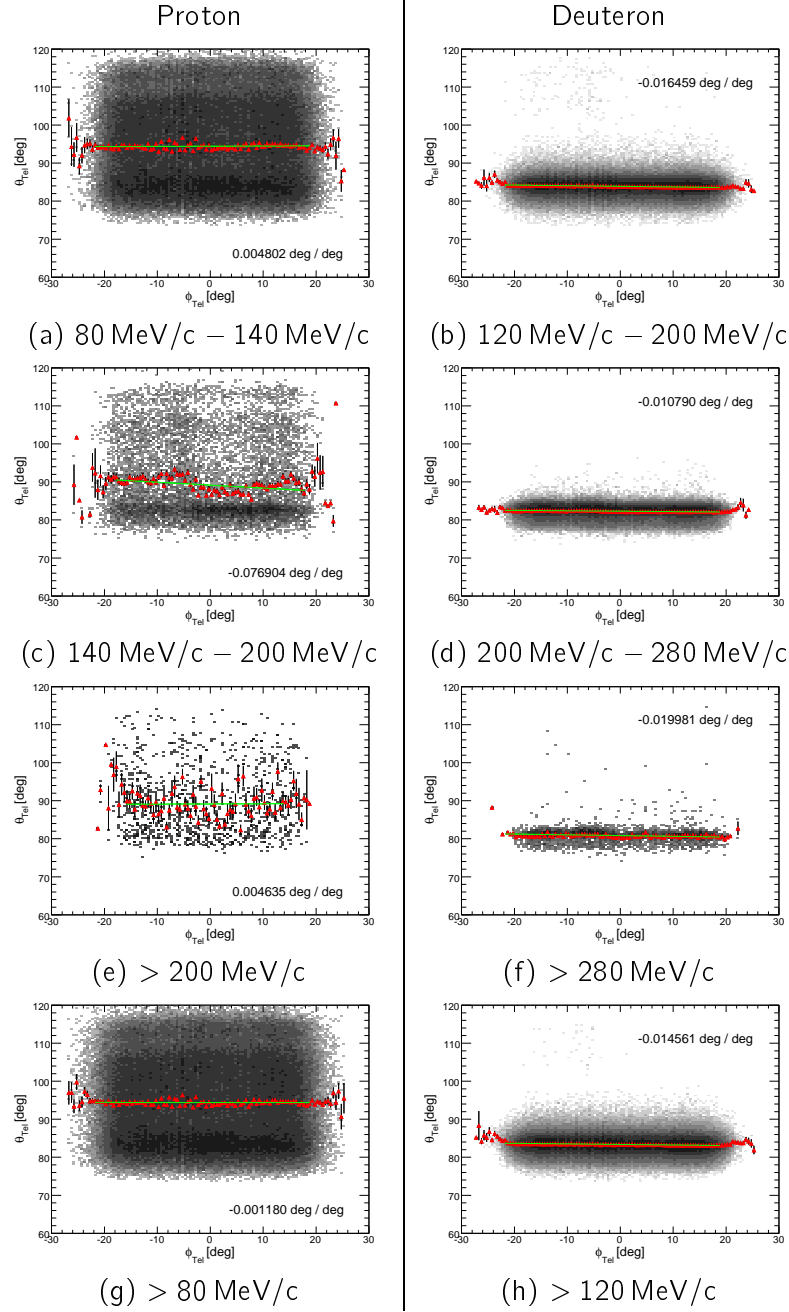
dd-Elastic at 2.46 GeV/c

Figure A.10: θ vs. ϕ for protons as well as deuterons separated into different momentum ranges.

Proton

Deuteron

(a) 80 MeV/c − 140 MeV/c

(b) 120 MeV/c − 200 MeV/c

(c) 140 MeV/c − 200 MeV/c

(d) 200 MeV/c − 280 MeV/c

(e) > 200 MeV/c

(f) > 280 MeV/c

(g) > 80 MeV/c

(h) > 120 MeV/c
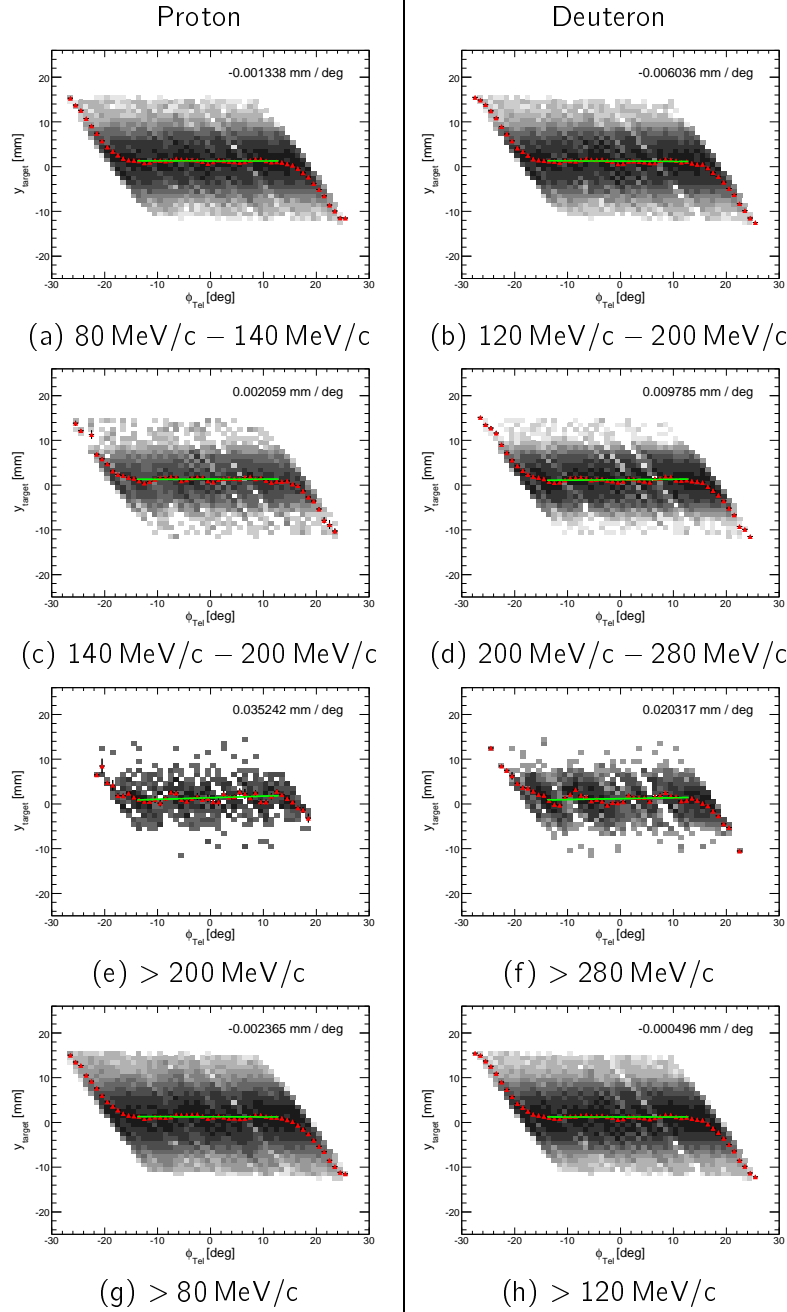
Figure A.11: y_{target} vs. ϕ for both protons and deuterons and different momentum ranges.

(a) $80\,\text{MeV/c} - 140\,\text{MeV/c}$

(b) $140\,\text{MeV/c} - 200\,\text{MeV/c}$

(c) $> 200\,\text{MeV/c}$
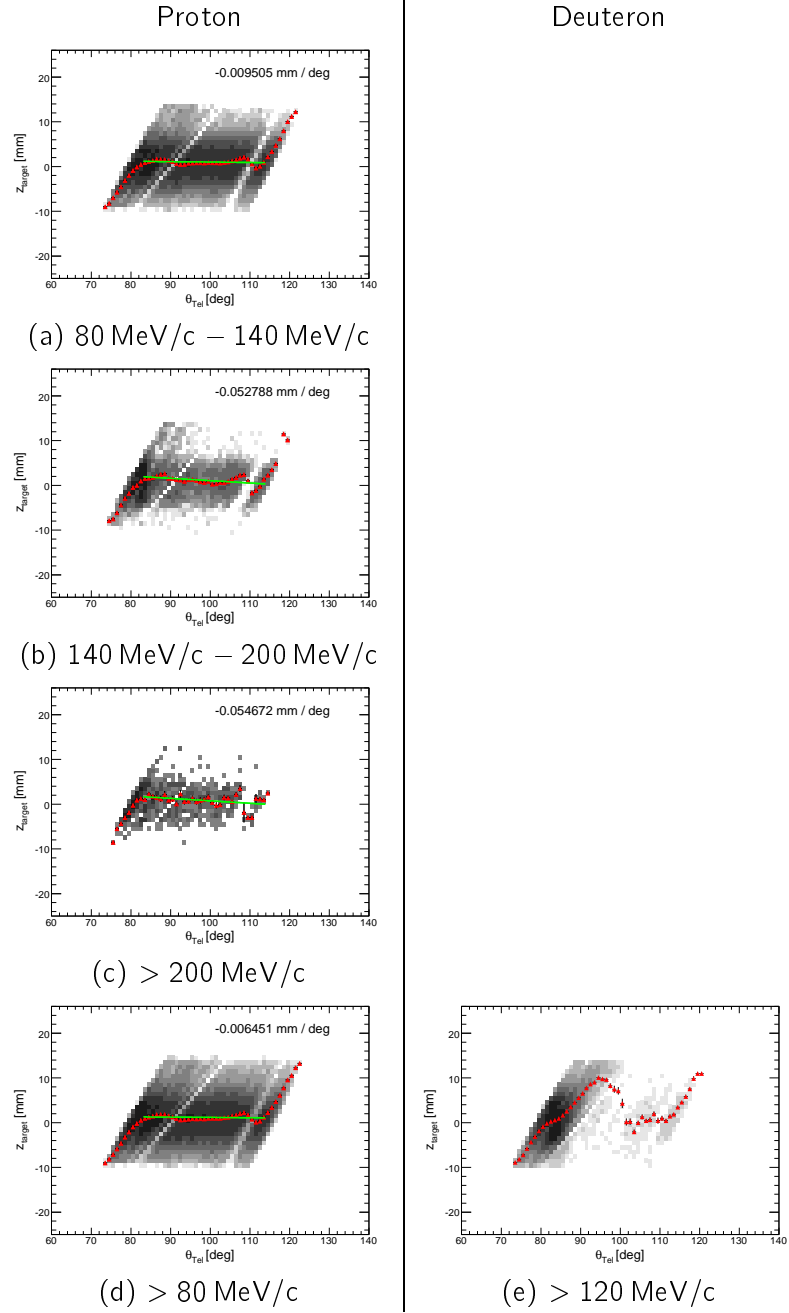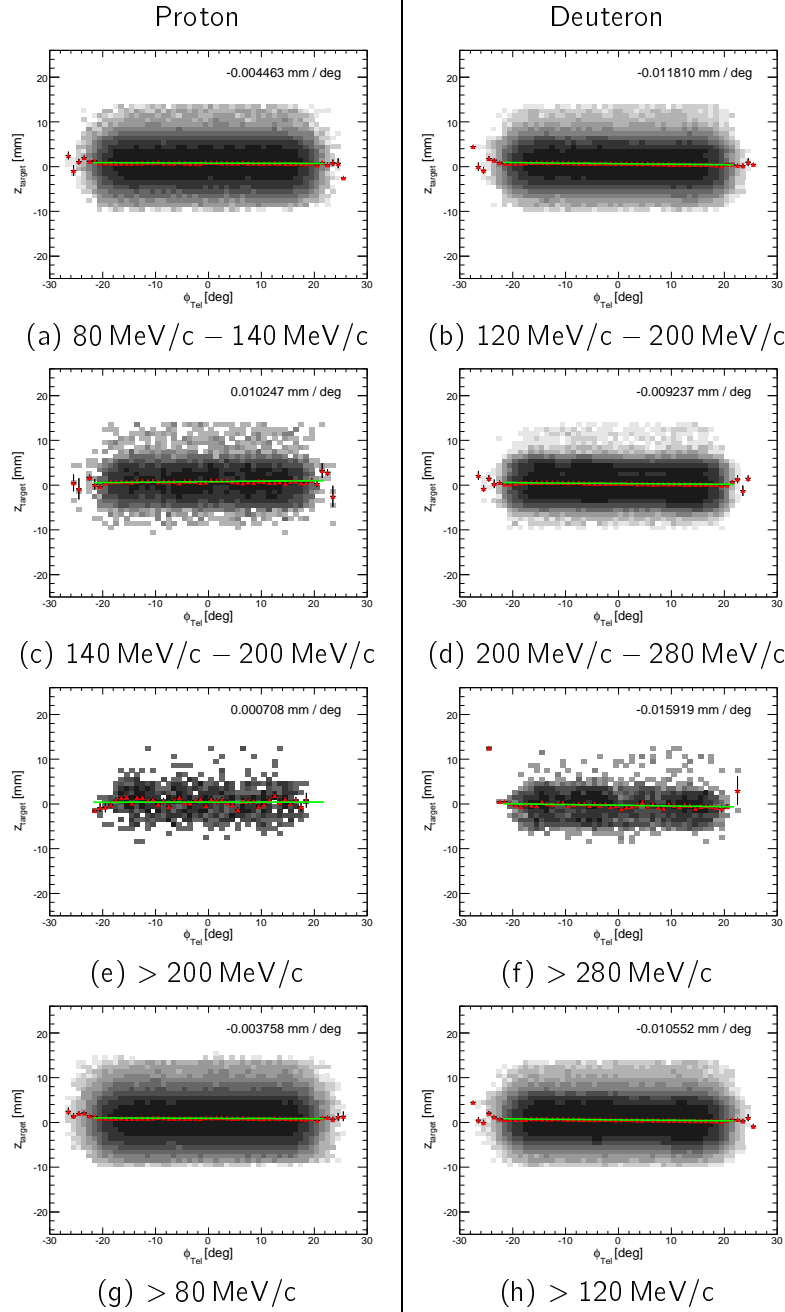
(d) $> 80\,\text{MeV/c}$

(e) $> 120\,\text{MeV/c}$

Figure A.12: z_{target} vs. θ for protons and deuterons. For deuterons the plots are not split into different momentum ranges.

Proton

Deuteron

(a) $80\,\mathrm{MeV/c} - 140\,\mathrm{MeV/c}$

(b) $120\,\mathrm{MeV/c} - 200\,\mathrm{MeV/c}$

(c) $140\,\mathrm{MeV/c} - 200\,\mathrm{MeV/c}$

(d) $200\,\mathrm{MeV/c} - 280\,\mathrm{MeV/c}$

(e) $> 200\,\mathrm{MeV/c}$

(f) $> 280\,\mathrm{MeV/c}$

(g) $> 80\,\mathrm{MeV/c}$

(h) $> 120\,\mathrm{MeV/c}$

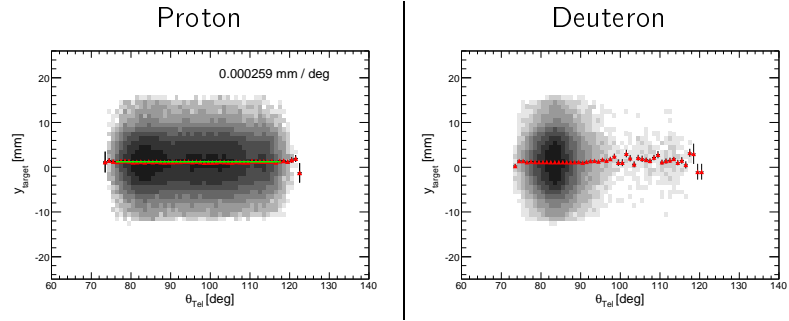Figure A.13: z_{target} vs. ϕ for protons and deuterons.

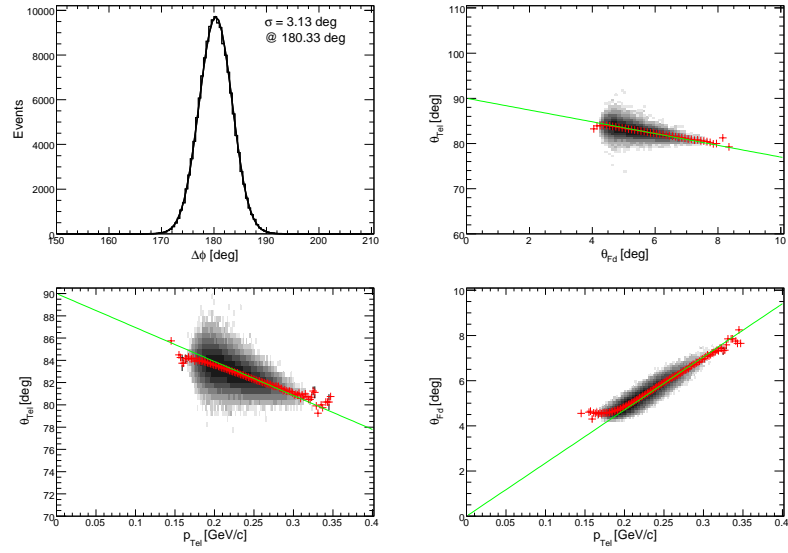Figure A.14: y_{target} vs. θ for protons as well as deuterons.

Figure A.15: Alignment plots for dd-elastic at 2.46 GeV/c beam momentum.

Bibliography

[1] S. Barsov *et al.* ANKE, a New Facility for Medium Energy Hadron Physics at COSY-Jülich. *Nucl. Instr. and Meth. in Phys. Res.*, A462:364–381, 2001.

[2] R. Maier *et al.* Cooler synchrotron COSY. *Nucl. Phys.*, A626:395–403, 1997.

[3] R. Maier. Cooler synchrotron COSY - Performance and perspectives. *Nucl. Instr. and Meth. in Phys. Res.*, A390:1–8, 1997.

[4] K. Kilian *et al.* Cooler Synchrotron COSY Jülich - User Guide. Technical report, IKP-KFA, 1990.

[5] A. Kacharava, F. Rathmann and C. Wilkin for the ANKE Collaboration. Spin Physics from COSY to FAIR, 2005. Available from `http://www.fz-juelich.de/ikp/anke`.

[6] M. Capiluppi *et al.* Beam request for COSY experiment #146.1 *Commissioning and Initial Research with PIT at ANKE*, August 2005.

[7] *Antiproton-Proton Scattering Experiments with Polarisation*, Letter-of-intent for HESR at FAIR. Spokesperson: P. Lenisa and F. Rathmann. Available from `http://www.fz-juelich.de/ikp/pax`, Jülich 2004.

[8] Conceptual Design Report for *An International Facility for Antiproton and ion Research*. Available from `http://www.gsi.de/GSI-Future/cdr`, November 2001.

[9] B. Povh, K. Rith, C. Scholz, and F. Zetsche. *Teilchen und Kerne*. Springer, 6 edition, 2004.

[10] H. Caln *et al.* Measurement of the quasifree $pn \to pn\eta$ reaction. *Phys. Rev. C*, 58(5):2667–2670, November 1998.

[11] I. Lehmann *et al.* Spectator detection for the measurement of proton-neutron interactions at ANKE. *Nucl. Instr. and Meth. in Phys. Res.*, A530:275–285, 2004.

[12] I. Lehmann. ω *meson production in the pn $\to$ dω Reaction at ANKE*. PhD thesis, Universität zu Köln, 2003.

[13] S. Barsov *et al.* Near-threshold production of ω-mesons in the $pn \rightarrow d\omega$ reaction. *Eur. Phys. J.*, A21:521–527, 2004.

[14] N. Lang. *Schwellennahe Produktion von eta-Mesonen im Proton-Neutron Stoss am Magnetspektrometer ANKE.* PhD thesis, Universität Münster, 2004.

[15] M. Mikirtytchiants *et al.* The Polarized Gas Target for the ANKE Spectrometer at COSYJülich. *Proc. 9th Int. Workshop on Polarized Sources and Targets (PST 01)*, 2001. 30 Sept. - 4 Oct. 2001, Nashville, Indiana, USA.

[16] K. Grigoriev. private communication, 2005.

[17] H.J. Stein *et al.* (article in preparation).

[18] R. Engels *et al.* Precision Lamb-shift polarimeter for polarized atomic and ion beams. *Rev. Sc. Instr.*, 74(11):4607–4615, 2003.

[19] R. Engels *et al.* Background reduction by a getter pump around the ionization volume of a Lamb-shift polarimeter and possible improvements of polarized ion sources. *Rev. Sc. Instr.*, 76, 2005.

[20] F. Bauer and K. Büß er. A polarimeter for GeV protons of recirculating synchrotron beams. *Nucl. Inst. and Meth. in Phys. Res.*, A431(3):385–395, July 1999.

[21] H. Rohdje. The Edda Experiment at COSY. In *Proceedings of the 7th Int. Workshop on Polarized Gas Targets and Polarized Beams*, Urbana, August 18-22 1997.

[22] P. D. Eversheim *et al.* Status of the polarized source for the cooler synchrotron COSY-Jülich. In *AIP Conference Proceedings*, volume 293, pages 92–96, December 1993.

[23] M. Eggert. *Entwicklung eines gepulsten Cäsium-Ionenstrahls für die Quelle polarisierter Ionen an COSY/Jülich.* PhD thesis, University of Cologne, 1999.

[24] B. Lorentz *et al.* Status of the Cooler Synchrotron COSY-Juelich. In *Proceedings of the 9th European Particle Accelerator Conference (EPAC 2004)*, page 1246, Lucerne, Switzerland, 2004.

[25] D. Boutigny *et al.* BaBar Technical Design Report. Technical report, SLAC-R-95-457 Report, March 1995.

[26] C. Bozzi *et al.* The BaBar Silicon Vertex Tracker. *Nucl. Instr. and Meth. in Phys. Res.*, A461:162–167, 2001.

[27] C. Bozzi *et al.* The design and construction of the BaBar silicon vertex tracker. *Nucl. Instr. and Meth. in Phys. Res.*, A447:15–25, 2000.

[28] PEP II - Conceptual Design Report. Technical report, Report SLAC-418, June 1993.

[29] Micron Semiconductor Ltd. *http://www.micronsemiconductor.co.uk*.

[30] A. Mussgiller. Setup and Test of a vacuum-compatible Read-Out System for Silicon-Strip-Detectors. Master's thesis, Fachhochschule München, 2000.

[31] straschu Leiterplatten GmbH, An der Schmiede 15, 26135 Oldenburg, Germany. *http://www.straschu-lp.de*.

[32] D. Protic, T. Krings, and R. Schleichert. Development of Double-Sided Microstructured Si(Li) Detectors. *IEEE Trans. Nucl. Sci.*, 49(4):1993–1998, August 2002.

[33] D. Protic, E. L. Hull, T. Krings, and K. Vetter. Large-Volume Si(Li) Orthogonal-Strip Detectors for Compton-Effect-Based Instruments. In *Proc. IEEE Conf. Nuclear Science Symp.*, Rome, 2004. accepted for publication in IEEE Trans. Nucl. Sci.

[34] Hirose Electronic GmbH, Ostfildern, Germany. *Low Profile 0.3mm Pitch Connectors For FPC - FH18 Series*, 4 edition, 2004.

[35] Integrated Detectors & Electronics AS. *VA32TA2 - Technical Information Manual*. See also http://www.ideas.no.

[36] Integrated Detectors & Electronics AS. *VA32HDR - Technical Information Manual*. See also http://www.ideas.no.

[37] R. Schleichert, T. Krings, S. Merzliakov, A. Mussgiller, and D. Protic. A Self-Triggering Silicon-Tracking Telescope for Spectator Proton Detection. *IEEE Trans. Nucl. Sci.*, 50(3):301–306, June 2003.

[38] Integrated Detectors & Electronics AS. *TA32CG - Technical Information Manual*. See also http://www.ideas.no.

[39] CeramTec AG - Innovative Ceramic Engineering, Fabrikstraße 23 - 29, 73207 Plochingen, Germany. *Sub D Type (MIL-C-24308) Connectors*, 2005. from Ceramaseal - Multipin Connector Catalog.

[40] S. Barsov *et al.* COSY Proposal #114: "Study of ω-Meson Production in the Reaction $pn \rightarrow d\omega$", November 2002. Spokespersons: R. Schleichert.

[41] K. Zwoll *et al.* A Flexible Data Acquisition System for Experiments at COSY. *IEEE Trans. Nucl. Sci.*, 41(1):37–44, 1994.

[42] M. Drochner, W. Ervnen, P. Wüstner and K. Zwoll. The second Generation of DAQ-Systems at COSY. KFA-Jülich internal report, 1997.

[43] M. Hartmann. *Aufbau und Einsatz von Datenaufnahmesystemen zur Untersuchung der Strangness Produktion von Atomkernen mit Protonen an COSY Jülich*. PhD thesis, Universität zu Köln, 1999.

[44] M. Kirsch. *SIS1100/3100 PCI to VME*. Struck Innovative Systeme GmbH, Hamburg, Germany, 2004. See also `http://www.struck.de`.

[45] M. Drochner *et al.* A VME Controller for Data Acquisition with flexible Gigabit Data Link to PCI. In *12th IEEE Realtime conference proceedings*, pages 204–207, June 2001.

[46] The NetBSD Project. `http://www.netbsd.org`.

[47] W. Erven, P. Wüstner, A. Ackens, K. Zwoll. PCI Synchronisations Module. KFA-Jülich internal report, 1997.

[48] Kramert. *instruction manual - VPG517*. Dipl.-Ing. Kramert GmbH, December 1999.

[49] C.A.E.N. spa. *Technical Information Manual - Mod. V 550 (2 Channel C-Rams)*, 1.0 edition, 4 1998.

[50] M. Kirsch. *SIS3800 VME Scaler/Counter User Manual*. Struck Innovative Systeme GmbH, Hamburg, Germany, 1999. See also `http://www.struck.de`.

[51] C.A.E.N. spa. *Technical Information Manual - Mod. V 513 (DIGITAL IO)*, 1.0 edition, 4 1998.

[52] V. Komarov *et al.* First Module of the Forward Detector Proportional Chambers of the Anke Spectrometer. *IKP/COSY Annual Report*, 1996.

[53] B. Chiladze *et al.* The Forward Detector of the ANKE Spectrometer. *Particles and Nuclei*, Lett. 4, 2002.

[54] W. R. Leo. *Techniques for Nuclear and Particle Physics Experiments*. Springer-Verlag, 2 edition, 1994.

[55] *Ubuntu - Linux for Human Beings*. `http://www.ubuntulinux.org`.

[56] *GCC - the GNU Compiler Collection*. `http://gcc.gnu.org`.

[57] Glenn. F. Knoll. *Radiation Detection And Measurement*. John Wiley & Sons, Inc., 2 edition, 1979.

[58] G. Riepe *et al.* Performance of a high-purity germanium multi-detector telescope for long-range particles. *Nucl. Inst. and Meth.*, 177(2-3):361–367, November 1980.

[59] S. Agostinelli *et al.* GEANT4: A Simulation Toolkit. *Nucl. Inst. and Meth. in Phys. Res.*, A506:250–303, 2003. See also `http://geant4.web.cern.ch/geant4`.

[60] A. Mussgiller. A New Geant4 based Simulation Framework for ANKE. *IKP/COSY Annual Report*, 2004. See also `http://www.fz-juelich.de/ikp/anke`.

[61] A. Kacharava and F. Rathmann. COSY Proposal #125: "The Polarizsed Charge-Exchange Reaction $\vec{d} + p \rightarrow (pp)n$", March 2003. Spokespersons: A. Kacharava and F. Rathmann.

[62] Rene Brun and Fons Rademakers. ROOT - An Object Oriented Data Analysis Framework. *Proceedings AIHENP'96 Workshop, Lausanne, Sep. 1996, Nucl. Inst. and Meth. in Phys. Res.*, A389:81–86, 1997. See also `http://root.cern.ch`.

[63] V. Hejny, M. Hartmann, and A. Mussgiller. RootSorter: A New Analysis Framework for ANKE. *IKP/COSY Annual Report*, 2002. See also `http://www.fz-juelich.de/ikp/anke`.

[64] G. Ohlsen. Polarization transfer and spin correlation experiments in nuclear physics. *Rep. Prog. Phys.*, 35:717–801, May 1972.

[65] M. Haji-Saied *et al.* Tensor and vector spin observables in p-d elastic scattering at 600, 800 and 1000 MeV. *Phys. Rev. C*, 36(5):2010–2017, 1987.

[66] V. Ghazikhanian *et al.* Vector and tensor spin observables in the reaction $\vec{p}(\vec{d}, d)\vec{p}$ at 1.6 GeV. *Phys. Rev. C*, 43(4):1532–1552, 1991.

[67] J. Arvieux *et al.* Elastic scattering of polarized deuterons by protons at intermediate energies. *Nucl. Phys. A*, 431(4):613–636, 1984.

[68] J. Arvieux *et al.* Deuteron polarimetry studies at low and intermediate energies. *Nucl. Instr. and Meth. in Phys. Res.*, A273(1):48–58, 1988.

[69] D. Chiladze. Deuteron polarimetry studies at COSY-Jülich with the ANKE spectrometer. Master's thesis, Tbilisi State University - High Energy Physics Institute, 2004.

[70] D. Chiladze *et al.* Deuteron Polarimetry at ANKE. Technical report, August 2004.

[71] D. Chiladze *et al.* Determination of Deuteron Beam Polarizations at COSY. *Phys. Rev. ST AB*. article under preparation.

[72] M. Hartmann. private communication.

[73] Xilinx, Inc. *Spartan-II 2.5V FPGA Family: Complete Data Sheet*, August 2004. See also `http://www.xilinx.com`.

[74] P. Baron *et al.* MATE, a single front-end ASIC for silicon strip, Si(Li) and CsI detectors. In *Nuclear Science Symposium Conference Record*, volume 1, pages 386–390. IEEE, October 2003.

[75] Y. Blumenfeld *et al.* MUST: A silicon strip detector array for radioactive beam experiments. *Nucl. Inst. and Meth. in Phys. Res.*, A421(3):471–491, February 1999.

Acknowledgements

I would like to thank:

- Prof. Dr. H. Ströher for providing the possibility to do this work at his institute and for reading the thesis as my referee,

- Prof. Dr. P. Reiter for acting as the co-referee,

- Prof. Dr. D. Stauffer for the consent to act as the head of the examination commission,

- Dr. Ralf Schleichert for acting as my supervisor, his continuous advice and many productive discussions,

- Dr. Sergey Barsov for large and valuable contributions to this work, especially to the dead-time correction and the applications chapter,

- Dr. Sergey Merzliakov and Dr. Sergey Trusov for all the read-out electronics and software that made working with the setup possible,

- Colin Wilkin, Dr. Andro Kacharava and David Chiladze for helping me understand the polarimetry business

- my colleagues at the institute who could help out with a lot of things and provided a nice atmosphere,

- my former physics teacher Mrs. B. Krämer, who got me into that whole physics business
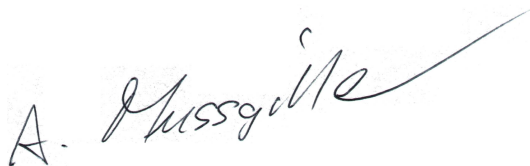
and finally

- my wife Daniela, my son Korbinian, my daughter Josephine and my parents for their continuous support

Erklärung

Ich versichere, daß ich die von mir vorgelegte Dissertation selbständig angefertigt, die benutzten Quellen und Hilfsmittel vollständig angegeben und die Stellen der Arbeit - einschließlich Tabellen, Karten und Abbildungen -, die anderen Werken im Wortlaut oder dem Sinn nach entnommen sind, in jedem Einzelfall als Entlehnung kenntlich gemacht habe; daß sie - abgesehen von unten angegebenen Teilpublikationen - noch nicht veröffentlicht worden ist sowie, daß ich eine solche Veröffentlichung vor Abschluß des Promotionsverfahrens nicht vornehmen werde. Die Bestimmungen dieser Promotionsordnung sind mir bekannt. Die von mir vorgelegte Dissertation ist von Herrn Prof. Dr. H. Ströher betreut worden.

Veröffentlichungen

- R. Schleichert, T. Krings, S. Merzliakov, A. Mussgiller and D. Protic, A Self-Triggering Silicon-Tracking Telescope for Spectator Proton Detection, IEEE Trans. Nucl. Sci. 50(3);301-306, 2003

- D. Chiladze *et al.*, Determination of Deuteron Beam Polarizations at COSY, in Vorbereitung zur Veröffentlichung in Phys. Rev. ST AB.

- D. Chiladze *et al.*, Vector and tensor analysing powers in deuteron-proton breakup reactions at intermediate energies, in Vorbereitung zur Veröffentlichung in European Physical Journal.

A. Mussgiller

Lebenslauf

Name:	Andreas Mussgiller	
geboren am:	4. April 1974	
geboren in:	München	
Familienstand:	verheiratet, zwei Kinder	

Eltern:	Vater:	Martin Mussgiller
		geb. am 10. November 1939
	Mutter:	Siglinde Filthaut, geb. Herold
		geb. am 13. November 1945

Promotion: Forschungszentrum Jülich GmbH
"Identification and Tracking of low Energy Spectator Protons"
seit Mai 2004

Aufbaustudium: Universität zu Köln
Oktober 2000 bis März 2003
Gesamtnote "gut"

Diplom: Forschungszentrum Jülich GmbH / Fachhochschule München
Oktober 1999 bis April 2000
Gesamtnote "gut"

Studium: Fachhochschule München
Fachbereich Pysikalische Technik
Oktober 1995 bis Oktober 1999

Zivildienst: Heilpädagogisches Centrum Augustinum e. V.
September 1994 bis Juli 1995

Schule:	Fachabitur 1994	Gesamtnote "gut"
	1992 - 1994	Fachoberschule München
	1991 - 1992	John R. Rogers High School - USA
	1987 - 1991	Georg-Büchner-Realschule München
	1984 - 1987	Max-Planck-Gymasium München
	1980 - 1984	Grundschule am Hedernfeld München